Characterization of Graphene Grown Directly on Crystalline Substrates

A DISSERTATION SUBMITTED TO THE FACULTY OF THE UNIVERSITY OF MINNESOTA BY

Sara L. Rothwell

IN PARTIAL FULFILLMENT OF THE REQUIERMENTS FOR THE DEGREE OF DOCTOR OF PHILOSOPHY

Advisor: Philip I. Cohen

September, 2015

Acknowledgements

I would like to graciously thank my advisor Phil Cohen for his continued support and patience. I also thank my thesis committee: Professors Paul Ruden, Andre Mkhoyan, and Bethanie Stadler, and collaborators Professor Ed Conrad from Georgia Tech and Professor Len Feldman from Rutgers University. I am grateful for their support and guidance as well. Last but not least, thanks to my fellow ECE grad students who are good friends.

Abstract

Graphene has become one of the most popular materials under research, particularly since the 2010 Nobel Prize in Physics. Many visions posit that graphene electronics will be some of the fastest and smallest circuitry physically feasible, however before this becomes reality the scientific community must gain a firm handle on the creation of semiconducting varieties of graphene. In addition, well understood epitaxial growth of graphene on insulating materials will add to the facility of fabricating all-carbon electronics. This thesis presents experimental work detailing the growth of pristine graphene grown on sapphire (GOS) through the thermal decomposition of acetylene, and the electronic characterization of graphene grown on nitrogen-seeded silicon carbide (NG), a semiconducting variety of graphene grown in collaboration with researchers at Georgia Institute of Technology and Rutgers University. GOS displays turbostratic stacking and characteristics of monolayer graphene as analyzed by Raman spectroscopy and atomic force microscopy. Scanning tunneling microscopy characterization of NG illustrates a topography of pleats from 0.5-2 nm tall, 1-4 nm thick, and 1-20 nm long, as well as atomically flat plateaus and other areas of intermixed features. Scanning tunneling spectroscopy measurements across NG features show peaks interpreted as Landau levels induced by strain. Analysis of these Landau levels in coordination with previous characterization concludes that a model employing a bandgap fits best.

Table of Contents

List of Tables

List of Figures

Acronyms

AFM Atomic force microscopy

ANL Argonne National Laboratory

ARPES Angle-resolved photoelectron spectroscopy

BNL Brookhaven National Laboratory

CSS Controlled silicon sublimation

CVD Chemical vapor deposition

DFT Density functional theory

DOS Density of states

FWHM Full width at half maximum

GOS Graphene grown on sapphire

HOPG Highly ordered pyrolytic graphite

KE Kinetic energy

LDOS Local density of states

LEED Low-energy electron diffraction

MBE Molecular beam epitaxy

ML Monolayer

NG Graphene grown on nitrogen-seeded SiC

ORNL Oak Ridge National Laboratory

RHEED Reflection high-energy electron diffraction

SiC Silicon carbide

STM Scanning tunneling microscopy

STS Scanning tunneling spectroscopy

TEM Transmission electron microscopy

TRIM The transport of ions in matter

UHV Ultra-high vacuum

XPS X-ray photoelectron spectroscopy

XRD X-ray diffraction

Symbols

A The vector potential

a Lattice parameter of graphene, 2.46 Å

$\hat{a}$ A lowering operator, $\sqrt{\frac{1}{2\hbar eB_z}}(p_x - eA_x + ip_y - ieA_y)$

$\hat{a}^\dagger$ A raising operator, $\sqrt{\frac{1}{2\hbar eB_z}}(p_x - eA_x - ip_y + ieA_y)$

a_C The carbon-carbon bond length in graphene, 1.42 Å

δa_i Change in magnitude of a_C after displacement

B The magnetic field, $\nabla \times A = B$

c Basis vector for the graphene lattice

$b_{1,2}$ Reciprocal lattice vectors for graphene

$c_{i,j}$ Tight-binding coefficient for a Bloch function

E Energy

$\hat{H}$ The Hamiltonian

H_n A Hermite polynomial of order n

h The height of a ripple, $h(x, y)$ is a height function

I Current

k Momentum or wavevector

L A length

L_a Crystal domain size

l_B The magnetic length, $l_B = \frac{\hbar}{eB_z}$

M_{ij} Tunneling matrix element

m Mass

N The number of atoms in a lattice or Bloch functions in a tight-binding calculation

n The number of electrons or charge carriers, or the integer Landau index

$\hat{n}$ The number operator

p Momentum, $p = \hbar k$ or $p = \hbar q$

q A small momentum or wavevector

R Matrix for clockwise rotation or reflection amplitude

R_i A lattice vector in real space to atom i

R_T Tip radius

r A real space or position space vector, $r = \sqrt{x^2 + y^2}$ or $r_i = x$, y, or z

S The overlap integral at the same site

s_0 Phase for the overlap integral at the same site

Δs An arc length

T Transmission amplitude

$t_{0,1,2,3}$ Phase for the overlap integral on different sites, tight-binding hopping parameters

U An applied potential

u_i A displacement

u_{ij} A component of the strain tensor, $u_{ij} = \frac{\delta u_i}{\delta r_j}$

V Voltage

v The Fermi velocity, $v = \frac{\sqrt{3}at_0}{2\hbar}$

w The width of a ripple

Δ A bandgap

$\delta_{1,2,3}$ The nearest-neighbor vectors for graphene

ϵ_{2p} The energy of the 2p$_z$ orbital in graphene

η Variable for a free space electron in an applied field, $\eta = \frac{p_x}{eB_z} - \frac{1}{2}y$

π A type of hybrid bond, or the constant π (by context)

Ψ**,** ψ A (tight-binding) wavefunction

Φ A Bloch function or the work function of a material (by context)

ϕ An atomic orbital, s, p, d, etc...

ρ_i Vector between two atoms ending at atom i, $|\rho_i| = a_C$ if unstrained

$\rho_{t,s}$ Density of states

σ A Pauli matrix, a type of hybrid bond, or the standard deviation

τ Decay time constant

ω Cyclotron frequency

ξ Variable for a free space electron in an applied field, $\xi = p_y - \frac{eB_z}{2}x$

Physical Constants

e Electron charge, 1.602*10^{-19} C

$\hbar$ Planck constant, 1.055*10^{-34} Js

β Grüneisen parameter, $\beta = -\frac{d\ln(t)}{d\ln(a_C)} \approx 2$ for graphene

π Ratio between a circle circumference and radius, $\pi = 3.1415...$

Φ_0 Magnetic flux quantum, $\Phi = (\hbar\pi)/e$

Introduction

Graphene is a highly conductive carbon thin film, posited by some to be the future of fast, tiny, flexible circuitry. Toward that end, semiconducting graphene is needed to provide the possibility of all-carbon transistors. Conventional graphene grown from a variety of fabrication methods, including mechanical exfoliation, silicon carbide (SiC) epitaxy, and chemical vapor deposition (CVD) among others, has been characterized extensively reporting high mobilities and no bandgap. A radical departure from the ideal monolayer sheet is required to fabricate a semiconducting form of this material.

Bandgaps in graphene have been reported under a variety of conditions. Various dopants have been reported to induce a gap [1, 2], including nitrogen [3–5], but these doped films are predicted to have low mobility due to scattering from substitutional dopants. Graphene ribbons have experimentally demonstrated confinement induced bandgaps, but continue to present lithographic challenges for large scale fabrication and device integration [6, 7]. Finally, graphene placed on an array of 1D periodic lines in coordination with a chemically functionalized surface has been reported to have small, strain induced gaps of 0.14-0.19 eV, dependent on feature pitch [8].

Semiconducting graphene is not the only attainable goal; graphene grown directly on an insulating substrate is also desirable because if achieved, this graphene may be directly patterned into devices using conventional lithography techniques. Graphene grown on conductive substrates must be transferred prior to patterning and thereby introduces more complexity into any device fabrication procedure. Moreover, transfer techniques typically leave residue and often cause tears which would reduce yield and may significantly alter the de-

sired traits of the transferred graphene [9].

This thesis presents experimental work characterizing epitaxial graphene grown on sapphire (GOS), and epitaxial graphene grown on nitrogen-seeded SiC (NG). NG was grown in collaboration with Rutgers University and Georgia Institute of Technology. Chapter 1 focuses on the theoretical background of graphene, the electronic structure in vacuum and under an applied magnetic field as derived by tight-binding theory, and the theoretical behavior of graphene's electronic structure with strain. Chapter 2 reviews the background theory of the characterization equipment used herein to characterize the experimentally fabricated films. Chapter 3 experimentally characterizes and discusses graphene grown on sapphire from the thermal decomposition of acetylene and presents a review of the current state of the art graphene grown via controlled silicon sublimation (CSS) on C-face SiC. Chapter 4 presents the background research on nitrogen doping in graphene, nitrogen in nitrogen-seeded SiC, and the previously published experimental research on NG films, concentrating on the X-ray photoelectron spectroscopy (XPS) characterization of nitrogen in NG. Chapter 5 presents scanning tunneling microscopy and spectroscopy (STM and STS) characterizing NG and discusses this data in light of previous work which shows a valence band offset in NG. The discussion presents an analysis of NG wherein strain-induced pseudo-magnetic fields create Landau levels visible in STS spectra. The energy distribution of these Landau levels is consistent with an electronic model employing a finite bandgap.

Chapter 1

Graphene Theory

The derivation of the electronic structure for graphene starts with considering the electronic structure of graphite. For the purposes of this thesis, the low energy form of graphene's Hamiltonian is considered primarily.

1.1 Graphene Lattice Structure

The term 'graphene' refers to a single isolated sheet of graphite, or few layer graphite that still maintains some of the unique electronic character of monolayer graphene. The graphene crystal lattice is a hexagonal Bravais lattice with a two atom basis. Fig. 1.1 illustrates the 2D honeycomb structure of a single sheet with the two sublattices highlighted in red and blue and nearest neighbor vectors identified. Bernal stacking is also illustrated, which is the stacking pattern for graphite where layers of graphene alternate in an ABAB pattern, each layer rotating 60° with respect to the underlying layer.

Bernal stacking renders the two sublattices of graphene inequivalent. In Bernal stacked material, one sublattice is located directly above atoms in the lower layer and one sublattice sits in the center of the honeycomb hex alone. This type of stacking has the greatest interlayer bonding. This is visible via STM where Bernal stacked graphene has a hexagonal appearance rather than honeycombed. The STM analysis of graphene scattering and inter-

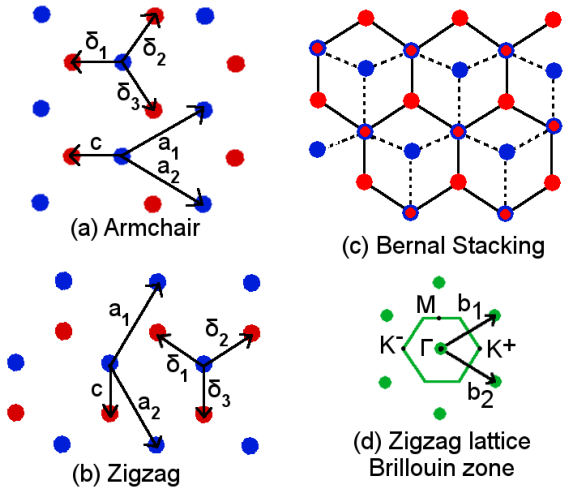

Figure 1.1: The graphene crystal lattice with lattice vectors $a_{1,2}$, basis vector c, and nearest neighbor vectors $\delta_{1,2,3}$. (a) x-axis parallel with the armchair axis. (b) x-axis parallel to the zigzag axis. (c) Bernal stacking. The solid lines connect the honeycomb of a lower layer and the dashed lines connect the honeycomb of a top layer, rotated 60° with respect to the lower layer and elevated 3.35 Å. Multilayer Bernal stacked graphene or graphite is made by further layers alternating between the solid honeycomb and the dotted honeycomb in an ABAB stack. (d) The reciprocal lattice and Brillouin zone for a zigzag lattice with significant locations Γ, M, $K^{\pm}$, and reciprocal space vectors $b_{1,2}$ marked.

layer bonding, such as the appearance of Bernal stacking in STM, is addressed in Chapter 2 and the STM analysis of NG is addressed in Chapter 5.

1.2 Derivation of Graphene's Electronic Structure

Tight binding derives the allowed energy bands for a crystalline system by modeling the electron wavefunctions of the system as a linear combination of atomic orbitals (which are presumed to be known functions, such as spherical harmonic functions) [10]. Carbon has 6 electrons, 2 of which are sequestered in a tightly bound 1s orbital. The remaining four are in the 2s and 2p orbitals; carbon commonly forms hybrid bonds involving all four of these valence electrons. Diamond bonding is the result when all four are involved in sp^3 bonds.

In graphene, three carbon atoms form hybrid σ or sp^2 bonds within the sheet plane and the fourth electron, the $2p_z$ orbital electron, forms a π bond above and below the sheet of graphene [11, 12]. For modeling purposes, this implies that each carbon atom contributes one electron to conduction [13, 12].

Fig. 1.1 illustrates both a zigzag and an armchair oriented lattice. The armchair orientation is used at times in literature [14], but this thesis will primarily use the zigzag orientation where the x-axis is parallel to the zigzag axis. The lattice, basis, and reciprocal lattice vectors are:

$$\begin{aligned} \text{Zigzag lattice vectors } a_1 &= (\frac{a}{2}, \frac{\sqrt{3}a}{2}), a_2 = (\frac{a}{2}, -\frac{\sqrt{3}a}{2}), \\ \text{Zigzag basis vector } c &= (0, -\frac{a}{\sqrt{3}}), \\ \text{Zigzag reciprocal lattice vectors } b_1 &= (\frac{2\pi}{a}, \frac{2\pi}{\sqrt{3}a}), \quad b_2 = (\frac{2\pi}{a}, -\frac{2\pi}{\sqrt{3}a}). \end{aligned} \tag{1.1}$$

The reciprocal lattice vectors satisfy the requirements: $a_1 b_1 = a_2 b_2 = 2\pi$ and $a_1 b_2 = a_2 b_1 = 0$. For graphene, the lattice constant is $a = 2.46$ Å and the separation between two carbon atoms is $a_C = a/\sqrt{3} = 1.42$ Å, which is also the length of the basis vector. The interlayer spacing is 3.35 Å for Bernal stacking but may expand to 3.44 Å for turbostratic stacking (graphene layers stacked at random rotations) [15, 11].

The derivation of graphene's electronic structure here uses the standard tight binding formalism where a trial wavefunction Ψ_l is composed of a linear superposition of Bloch functions, Φ_j, which are in turn a linear superposition of N atomic orbitals, ϕ_j.

$$\text{Wavefunction: } \Psi_l(k, r) = \sum_{j=1}^{n} c_{l,j} \Phi_j(k, r), \tag{1.2}$$

$$\text{Bloch function: } \Phi_j(k, r) = \frac{1}{\sqrt{N}} \sum_{i=1}^{N} e^{ik.R_{j,i}} \phi_j(r - R_{j,i}), \tag{1.3}$$

Here, $R_{j,i}$ gives the position of the jth orbital in the ith unit cell; j = s, p, or d orbital (or 1, 2, 3... as notated by whichever preferred index), and i counts the until cells in the system. Expanding Bloch functions using orbital wavefunctions is preferable to a plane wave expansions since fewer are required. However, one drawback of this type of tight binding model is that atomic orbitals do not describe the interatomic regions [13, 10].

The energy for orbital/wavefunction component j at momentum k, $E_j(k)$ is given from trial eigenvalues of the Hamiltonian, which can be formally notated as follows:

$$E_j(k) = \frac{\langle \Psi_j | \, H \, | \Psi_j \rangle}{\langle \Psi_j \, | \, \Psi_j \rangle}. \tag{1.4}$$

After substituting in the wavefunctions, this becomes:

$$E_i = \frac{\sum\limits_{j,j'=1}^{n} c_{i,j}^* c_{i,j'} \langle \Phi_j | \, H \, | \Phi_{j'} \rangle}{\sum\limits_{j,j'=1}^{n} c_{i,j}^* c_{i,j'} \langle \Phi_j \, | \, \Phi_{j'} \rangle} = \frac{\sum\limits_{j,j'=1}^{n} c_{i,j}^* c_{i,j'} H_{jj'}}{\sum\limits_{j,j'=1}^{n} c_{i,j}^* c_{i,j'} S_{jj'}}. \tag{1.5}$$

$H_{jj'}$ and $S_{jj'}$ are the transfer and overlap integrals respectively, and take the form of a matrix between each orbital j which appears in the wavefunction expansion. Since the wavefunctions are functions of momentum k and position r, $H_{jj'}$ and $S_{jj'}$ are too. To calculate $E_j(k)$ at a particular k value, the coefficient $c_{i,j}^*$ must be optimized so as to minimize $E_j(k)$. To calculate the dispersion over many k values, the process is simply iterated over a near-continuum of k values.

A partial derivative of $E_j(k)$ with respect to $c_{i,j}^*$ while fixing the other $c_{i,j}$ values will now minimize the energy. This equation is set to 0 to find the minima:

$$\frac{\delta E_i(k)}{\delta c_{ij}^*} = \frac{\sum\limits_{j'=1}^{N} H_{jj'} c_{ij'}}{\sum\limits_{j'=1}^{N} S_{jj'} c_{ij}^* c_{ij'}} - \frac{\sum\limits_{j,j'=1}^{N} H_{jj'} c_{ij}^* c_{ij'}}{(\sum\limits_{j,j'=1}^{N} S_{jj'} c_{ij}^* c_{ij'})^2} \sum_{j'=1}^{N} S_{jj'}(k) c_{ij'} = 0 \tag{1.6}$$

To simplify, multiply both sides of the equation by $\sum\limits_{j,j'=1}^{N} S_{jj'}(k) c_{ij'}$, and substitute Eq. 1.5 into the second fraction in Eq. 1.6.

It is more clear to represent these equations in matrix form. If the expansion coefficients c_i are considered a column vector from 1 to N at unit cell i, then this equation can be represented by:

$$C_i = \begin{pmatrix} c_{i1} \\ \vdots \\ c_{iN} \end{pmatrix} \tag{1.7}$$

The Hamiltonian becomes:

$$HC_i = E_i(k)SC_i \tag{1.8}$$

This reveals some limits on the coefficient matrix. If there exists an inverse to the matrix $[H - E_i(k)S]$ then the minimum is at $C_i = 0$. Requiring all wavefunctions to equal 0 is an unphysical solution, it becomes a requirement of the problem that the matrix $[H - E_i(k)S]$ does not have an inverse:

$$\det[H - ES] = 0. \tag{1.9}$$

This is known as the secular equation. This equation may now be solved at iterated k values to find the electronic dispersion.

At this point, the problem departs from the theoretical tight binding setup and the material specifics for graphene must be included. As previously mentioned only one atomic orbital per carbon atom need be included in the model, which means one electron per carbon atom. Similarly there is one Bloch function per carbon atom as well. Thus for graphene, $n = N = 2$ as the honeycomb lattice has a basis of two. For a hexagonal Brillouin zone, the pertinent high symmetry points in reciprocal space which most characterize the energy dispersion will be the Γ point at (0,0), M at $(0, (4\pi)/(2\sqrt{3}a))$ (six total equivalent locations), and $K^{\pm}$ at $(\pm(4\pi)/(3a), 0)$ (each with three equivalent locations). Fig. 1.1(d) illustrates the locations of these points in reciprocal space. The dispersion calculation for graphene may be limited to nearest neighbors, which limits the overlap integrals to being between different sublattice atoms only. As may be seen in Fig. 1.1, atoms in the same sublattice are actually the 2nd tier of nearest neighbors. Thus in the overlap integrals implied by the secular equation are either at the same atom, or between two nearest neighbor atoms alone.

Recall Eq. 1.8 for graphene:

$$\begin{pmatrix} H_{11} & H_{12} \\ H_{21} & H_{22} \end{pmatrix} \begin{pmatrix} c_{i1} \\ c_{i2} \end{pmatrix} = E_j \begin{pmatrix} S_{11} & S_{12} \\ S_{21} & S_{22} \end{pmatrix} \begin{pmatrix} c_{i1} \\ c_{i2} \end{pmatrix} \tag{1.10}$$

The diagonal integral H_{AA} becomes:

$$\begin{aligned} H_{AA}(r) &= \frac{1}{N}\sum_{i=1}^{N} e^{ik(R-R')} \langle \phi_A(r-R')| H |\phi_A(r-R)\rangle \\ &= \frac{1}{N}\sum_{i=1}^{N} \epsilon_{2p} + \text{ neglected terms from } R > R' \pm a \text{ (second nearest neighbors)}, \\ &\simeq \epsilon_{2p}. \end{aligned} \tag{1.11}$$

Since sublattice A is mathematically identical to sublattice B save an offset, $H_{BB} = H_{AA}$. The variable ϵ_{2p} is chosen to represent this integral since this integral is a calculation of the energy of the $2p_z$ orbital [12]. It is the $2p_z$ orbital which donates one electron per carbon atom; the other components of the 2p orbital are bound up in the σ bonds between carbon atoms.

The overlap integral for atoms in two different sublattices becomes:

$$\begin{aligned} H_{AB} &= \frac{1}{N}\sum_{i=1}^{N}\sum_{j=1}^{3} e^{ik(R_{Bj}-R_{Ai})} \langle \phi_A(r-R_{Ai})| H |\phi_B(r-R_{Bj})\rangle \\ &= -\frac{1}{N}\sum_{i=1}^{N}\sum_{j=1}^{3} e^{ik(R_{Bj}-R_{Ai})} t_0 \\ &= -\frac{t_0}{N}\sum_{i=1}^{N}\sum_{j=1}^{3} e^{ik\delta_j} \equiv -t_0 f(k). \end{aligned} \tag{1.12}$$

Let $f(k) = \sum_{j=1}^{3} e^{ik\delta_j}$ for simplicity, where δ_j denotes the three nearest neighbor vectors for a carbon atom. For the zigzag lattice these are:

$$\text{Zigzag lattice: } \delta_1 = (-\frac{a}{2}, \frac{a}{2\sqrt{3}}),\ \delta_2 = (\frac{a}{2}, \frac{a}{2\sqrt{3}}),\ \delta_3 = (0, -\frac{a}{\sqrt{3}}) \tag{1.13}$$

The function $f(k)$ collects the phase from the three nearest neighbor terms, illustrated in Fig. 1.1. The lattice hoping parameter t_0 is assumed to be equal for all three parts. It is apparent that $H_{AB} = H_{BA}^*$ from this form.

The overlap integrals S_{AB} in Eq. 1.10 take the general form:

$$S_{AB} = \frac{1}{N}\sum_{i=1}^{N}\sum_{j=1}^{N} e^{ik(R_{Bj}-R_{Ai})} \langle \phi_A(r-R_{Ai}) \,|\, \phi_B(r-R_{Bj})\rangle \tag{1.14}$$

It may be seen that for S_{AA}, an overlap integral at the same atom, $S_{AA} = S_{BB} = 1$, which is expected for orthogonal wave functions. However orbitals from different atoms may not be orthogonal, thus S may have a value other than zero or unity. Using the previously defined function $f(k)$, let S_{AB} be represented by:

$$\begin{aligned} S_{AB} &\simeq \frac{1}{N} \sum_{i=1}^{N} \sum_{j=1}^{3} e^{ik(R_{Bj} - R_{Ai})} \left\langle \phi_A(r - R_{Ai}) \,|\, \phi_B(r - R_{Bj}) \right\rangle \\ &\equiv s_0 f(k) \end{aligned} \tag{1.15}$$

Summarizing from previous equations, t_0 is the inner product of the Hamiltonian between A and B sublattices, and s_0 is the overlap integral between sublattices.

From the previously defined functions, the matrix form Eq. 1.10 and respective secular equation Eq. 1.9 become:

$$\begin{pmatrix} \epsilon_{2p} & -t_0 f(k) \\ -t_0 f^*(k) & \epsilon_{2p} \end{pmatrix} \begin{pmatrix} c_{i1} \\ c_{i2} \end{pmatrix} = E \begin{pmatrix} 1 & s_0 f(k) \\ s_0 f^*(k) & 1 \end{pmatrix} \begin{pmatrix} c_{i1} \\ c_{i2} \end{pmatrix}, \tag{1.16}$$

$$\det \begin{pmatrix} \epsilon_{2p} - E & -(t_0 + E s_0) f(k) \\ -(t_0 + E s_0) f^*(k) & \epsilon_{2p} - E \end{pmatrix} = 0. \tag{1.17}$$

Solving the determinant for E, the eigenvalue and energy for a select k value, yields:

$$(E - \epsilon_{2p})^2 - ([E - \epsilon_{2p}] s_0 + \epsilon_{2p} s_0 + t_0)^2 |f(k)|^2 = 0, \tag{1.18}$$

$$E_{\pm} = \frac{\epsilon_{2p} \pm t_0 |f(k)|}{1 \mp s_0 |f(k)|}. \tag{1.19}$$

Experimental values for t_0 and s_0 are 3.033 eV and 0.129 respectively [12]. As commented previously, ϵ_{2p} may be set to 0 as a baseline energy. When graphed in Fig. 1.2 the characteristic circus tent dispersion is visible with precise connections of the valence and conduction bands at the 6 $K^{\pm}$ points of the Brillouin zone. As illustrated in Fig. 1.1, there are two inequivalent K points notated as K^+ and K^- which alternate around the Brillouin zone.

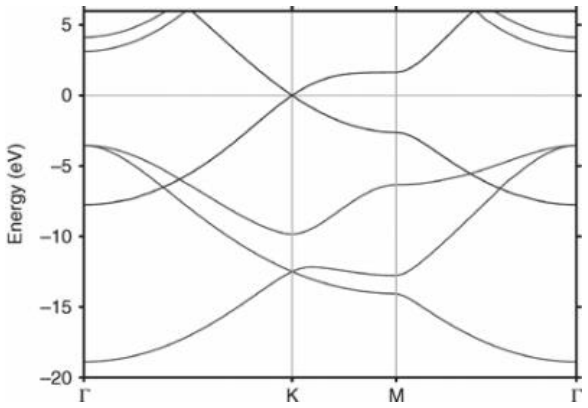

Figure 1.2: Graphene electronic dispersion. Note the 'X' crossover at the K point. Taken from [11].

1.2.1 Linear Dispersion at Low Energy

The dispersion near each $K^{\pm}$ point is linear for long wavelength (small energy), and can be shown to give a Dirac-like Hamiltonian in this regime. For a zigzag lattice, there are $K^{\pm}$ points at $(\pm(4\pi)/(3a), 0)$. At this point in reciprocal space the function $f(k)$ equals 0; the phase components cancel each other exactly resulting in a connection between the valence and conduction bands.

$$\begin{aligned} f(K^{\pm}_{ZZ}) &= \sum_{i=1}^{3} e^{i\delta_i \cdot (\pm\frac{4\pi}{3a},0)}, \\ &= e^{-i\frac{a}{2}(\pm)\frac{4\pi}{3a}} + e^{i\frac{a}{2}(\pm)\frac{4\pi}{3a}} + e^{i0}, \\ &= \cos[-(\pm)\frac{2\pi}{3}] + i\sin[-(\pm)\frac{2\pi}{3}] + \cos[(\pm)\frac{2\pi}{3}] + i\sin[(\pm)\frac{2\pi}{3}] + 1, \\ &= -\frac{1}{2} + (\pm)\cancel{-i\frac{\sqrt{3}}{2}} - \frac{1}{2} + (\pm)\cancel{i\frac{\sqrt{3}}{2}} + 1 = -1 + 1 = 0. \end{aligned} \tag{1.20}$$

The linear form of the dispersion can be now found by expanding around this point of connection at the $K^{\pm}$ points. Let q be a momentum originating at a K^{+} point such that $p_q = \hbar q = \hbar k - \hbar K^{+} = \sqrt{p_x^2 + p_y^2}$.

The function $f(k)$ may be rewritten with $p_{x,y}$ as the momentum coordinates in place of $k_{x,y}$.

$$f(k) = e^{ip_y a/\sqrt{3}\hbar} + 2e^{-ip_y a/2\sqrt{3}\hbar}\cos(\frac{2\pi}{3} + \frac{p_x a}{2\hbar}). \tag{1.21}$$

This may be expanded into a taylor series around 0 (since $q = 0$ at $k = K$) and simplified.

$$f(k) = (1 + \frac{ip_y a}{\sqrt{3}\hbar}) + 2(1 - \frac{ip_y a}{2\sqrt{3}\hbar})(-\frac{1}{2} - \frac{\sqrt{3}p_x a}{4\hbar}), \tag{1.22}$$

$$= -\frac{\sqrt{3}a}{2\hbar}(p_x - ip_y). \tag{1.23}$$

Note, this approximation which retains only linear terms in p is only valid in the regime where $pa/\hbar \ll 1$ [12].

Recall Eq. 1.12: $H_{AB} = -t_0 f(k)$. For $v = (\sqrt{3}at_0)/(2\hbar)$, the Fermi velocity, and setting the $2p_z$ energy, ϵ_{2p}, to zero, the full Hamiltonian in the linear approximation becomes:

$$H = v \begin{pmatrix} 0 & p_x - ip_y \\ p_x + ip_y & 0 \end{pmatrix} \tag{1.24}$$

This is referred to as the Dirac Hamiltonian, as it is linear in momentum. The Dirac Hamiltonian, which defines the energy of a free space electron while including relativity, achieves a similar form by expanding the relativistic Hamiltonian with matrix coefficients [16]. With no loss of terms, the graphene Hamiltonian may be written as: $H = v\sigma \cdot p$ where σ is the vector of 2x2 Pauli matrices, identical in form to the relativistic Hamiltonian. In 2D, p and σ will have no z component however. A mass term will even arise for a Hamiltonian describing graphene with a band gap. Thus, the graphene Hamiltonian can be considered equivalent to the Dirac Hamiltonian, save a change of constants in the dot product with p.

1.3 Magnetic Fields in Graphene

This thesis characterizes strained nitrogenated graphene in Chapters 4 and 5. STS of NG exhibits peaks indicative of Landau levels. Landau levels are typically seen in samples where an applied magnetic field is also present. The following sections will first derive and discuss the typical Landau levels seen in a free space electron with an applied field. This will be followed by a discussion of strain in the graphene lattice and a derivation of how strain effectively creates a pseudo field in graphene equivalent in effect to an applied field.

In the following, graphene will only be considered with an applied magnetic field in one direction: perpendicular to the graphene sheet and parallel to the z-axis. This sets some limits on the vector potential A. For a magnetic field such that $\nabla \times A = B$, if $B = (0, 0, B_z)$, then A may take the form $(0, B_z x, 0)$ or $(-\frac{1}{2}B_z y, \frac{1}{2}B_z x, 0)$. A magnetic field may be included in the Hamiltonian of a system by including the field component of the canonical moment: $p \to p - eA$. Note, e will herein always denote the magnitude of an electron's charge $|e|$; the sign will already be included in the given expressions. In SI units, the vector potential has units of Tesla-meters: [Tm] = [Js/Cm], thus the field component of the momentum is eA with units of momentum.

The following will idealize graphene as a 2D material. Although there can be inter-layer (vertical) movement in multilayer graphene, for the most part rotational disorder dissuades interlayer electrical bonding and the forms of graphene subsequently characterized in this thesis are all rotationally disordered. The Hamiltonian for a free electron in 2D using the symmetric gauge $A = (-\frac{1}{2}B_z y, \frac{1}{2}B_z x, 0)$ is as follows:

$$\begin{aligned} H &= \frac{1}{2m}(p_x - eA_x)^2 + \frac{1}{2m}(p_y - eA_y)^2, \\ &= \frac{1}{2m}(p_x + \frac{eB_z y}{2})^2 + \frac{1}{2m}(p_y - \frac{eB_z x}{2})^2, \\ &= \frac{1}{2m}(p_x^2 + \frac{eB_z}{2}(p_x y + y p_x) + \frac{e^2 B_z^2}{4}y^2 + p_y^2 \\ &\qquad - \frac{eB_z}{2}(p_y x + x p_y) + \frac{e^2 B_z^2}{4}), \end{aligned} \tag{1.25}$$

The following will use unitless variables to begin with:

$$\text{Length: } x_o = x/\sqrt{\frac{2\hbar}{eB_z}}, \quad y_o = y/\sqrt{\frac{2\hbar}{eB}}. \tag{1.26}$$

$$\text{Momentum: } p_{oi} = p_i/\sqrt{2\hbar e B}. \tag{1.27}$$

$$H = \frac{\hbar e B_z}{m}(p_{ox} + \frac{y_o}{2})^2 + \frac{\hbar e B_z}{m}(p_{oy} - \frac{x_o}{2})^2. \tag{1.28}$$

Recall the Hamiltonian for a harmonic oscillator [16]:

$$H = \frac{P^2}{2m} + \frac{1}{2}m\omega^2 X^2. \tag{1.29}$$

To use the well known solutions to this Hamiltonian, Eq. 1.28 will need to be be rewritten with alternative variables. Note, neither Eq. 1.28 nor the harmonic oscillator Hamiltonian is unitless, so the alternate variables will need to include the correct units.

$$\begin{aligned} \text{Let } \frac{\xi^2}{2m} &= \frac{\hbar e B_z}{m}(p_{oy} - \frac{x_o}{2})^2, \\ \xi &\rightarrow \sqrt{2\hbar e B_z}(p_{oy} - \frac{x_o}{2}) = p_y - \frac{eB_z}{2}x. \\ \text{Let } \frac{1}{2}m\omega^2\eta^2 &= \frac{\hbar e B_z}{m}(p_{ox} + \frac{y_o}{2})^2, \\ \eta &\rightarrow \sqrt{\frac{2\hbar e B_z}{m^2\omega^2}}(p_{ox} + \frac{y_o}{2}) = \frac{p_x}{eB_z} + \frac{y}{2}. \end{aligned} \tag{1.30}$$

After these variable substitution, the Hamiltonian is in the desired form:

$$H = \frac{\hbar e B_z}{m}(p_{ox} + \frac{y_o}{2})^2 + \frac{\hbar e B_z}{m}(p_{oy} - \frac{x_o}{2})^2 = \frac{\xi^2}{2m} + \frac{1}{2}m\omega^2\eta^2. \tag{1.31}$$

The pre-factor for ξ is precisely the scaling factor used previously for the unitless momentum. For η the units should similarly be of length which determines what the units for ω must be. The previous showed that $\sqrt{2\hbar/eB_z}$ has units of length; if $\omega = eB_z/m$ then the units are entirely satisfied. Alternatively, unit analysis on the pre-factor to η requires ω to have units of frequency, and eB_z/m is the only combination of the constants intrinsic to the problem which fulfills that requirement. In the harmonic oscillator problem, ω is the oscillation frequency; here ω is named the cyclotron frequency, ω_c. Classically, a free electron with velocity v in a uniaxial magnetic field will spiral at a related radius [13]: $r_c = v/\omega_c$. In the following example for one sheet of 2D graphene the electron will 'circle' in the x-y plane at this radius and frequency, although the calculated wavefunctions will in truth be a superposition of Gaussian functions creating a probability density.

These substitutions allows the use of the known solutions to the harmonic oscillator problem. The 1D harmonic oscillator wavefunctions are of the form:

$$\psi_n(x) = (\frac{eB_z}{\pi\hbar 2^{2n}(n!)^2})^{1/4} H_n[\sqrt{\frac{eB}{\hbar}}x] \exp[-\frac{eB_z}{2\hbar}x^2]. \tag{1.32}$$

Here, $\psi(x)_n$ is the nth solution to a harmonic oscillator in 1D and allows the calculation of wavefunctions from the ground state, $n = 0$, to excited levels, n= integers ≥ 1. The

function H_n is a Hermite polynomial. In the case of the applied field problem, ξ and η mix x and p, thus this solution cannot be taken wholesale.

In the next section, the raising and lowering operator form of the harmonic oscillator will be introduced, wherein the lowering operator a is defined to be $a = D * (p_x - ip_y) + (eB_z)/(2\hbar) * (y + ix))$ with a normalization constant D (see Eq. 1.41 to come). It is known that the lowest Landau level should obey $a\,|0\rangle = 0$ (or in plain speech, one should not be able to remove an electron from an empty state with no electrons). Using the position space representation of the operators that make up a, this may also be written:

$$[\frac{\delta}{\delta z*} + \frac{eB_z}{2\hbar}z]\psi_0(z, z*) = 0. \tag{1.33}$$

Here, $z = (x + iy)$. This differential equation shows that the lowest Landau level is formed from a superposition of functions of the form [16]:

$$\phi_{0,m}(x, y) = D(x + iy)^m exp[-\frac{eB_z}{2\hbar}(x^2 + y^2)]. \tag{1.34}$$

Again, D is a normalization constant, and m is any positive integer. This family of wavefunctions are all Gaussian functions, with the magnetic length $l_B = \sqrt{\hbar/eB_z}$ in place of the standard deviation. The magnetic length is often used as a rough estimate of the size of a Landau wavefunction. This is a lower estimate, however; a Gaussian is known to have a full width at half max (FWHM) of $2\sqrt{2\ln(2)}\sigma$ for a Gaussian with standard deviation σ. For $\sigma = l_B$ at fields of 50 and 100 T, this implies that the ground state Landau level extends to a diameter of 21 and 15 nm respectively.

The eigenenergies for the harmonic oscillator are:

$$E_n = \hbar\omega_c(n + \frac{1}{2}). \tag{1.35}$$

This is drawn directly from the known solutions for the harmonic oscillator.

This derivation illustrates that in a magnetic field, electrons are quantized in energy into a ladder of functions similar to the levels of a harmonic oscillator. These are named 'Landau levels'. This derivation shows the energy of each Landau level to be proportionate to an integer index, however subsequent derivation will conclude that in graphene these

levels are proportionate to a square root index. This contrast can be intuitively predicted because the previous derivation was for free electrons which are parabolic in momentum whereas in graphene the dispersion is linear in momentum around the K points.

1.3.1 Landau Levels in Graphene

This derivation will continue by using second quantization formalism, in particular raising and lowering operators, to show how Landau levels behave in graphene. Returning to the previous derivation, Eq. 1.29 can be recast using composite operators of P and X instead of the previous form:

$$\begin{aligned}
\text{Let } \hat{a} &= \sqrt{\frac{m\omega}{2\hbar}}X + i\sqrt{\frac{1}{2\hbar\omega m}}P, \\
\text{and } \hat{a}^\dagger &= \sqrt{\frac{m\omega}{2\hbar}}X - i\sqrt{\frac{1}{2\hbar\omega m}}P. \\
\hat{a}^\dagger\hat{a} &= \frac{1}{2\hbar\omega m}P^2 + \frac{m\omega}{2\hbar}X^2 + i\frac{1}{2\hbar}[X,P], \\
\text{Since } [X,P] = i\hbar,\ \hat{a}^\dagger\hat{a} &\to \frac{1}{2m\hbar\omega}P^2 + \frac{m\omega}{2\hbar}X^2 - \frac{1}{2}.
\end{aligned} \tag{1.36}$$

By inspection, the harmonic oscillator Hamiltonian (Eq. 1.29) can be written as:

$$H \to \hbar\omega(\hat{a}^\dagger\hat{a} + \frac{1}{2}). \tag{1.37}$$

These new operators are unitary ($[\hat{a}, \hat{a}^\dagger] = 1$), but they do not commute with the Hamiltonian:

$$\begin{aligned}
[\hat{a}, \hat{a}^\dagger] &= \hat{a}\hat{a}^\dagger - \hat{a}^\dagger\hat{a} = (\frac{1}{2m\hbar\omega}P^2 + \frac{m\omega}{2\hbar}X^2 + i\frac{1}{2\hbar}[P,X]) \\
&\quad - (\frac{1}{2m\hbar\omega}P^2 + \frac{m\omega}{2\hbar}X^2 + i\frac{1}{2\hbar}[X,P]) = -\frac{i}{\hbar}[X,P] = 1 \\
[\hat{a}, \hat{H}] &= \hbar\omega(\hat{a}\hat{a}^\dagger\hat{a} + \frac{1}{2}\hat{a} - \hat{a}^\dagger\hat{a}\hat{a} - \frac{1}{2}\hat{a}) \\
&= \hbar\omega([\hat{a}, \hat{a}^\dagger]\hat{a}) = \hbar\omega\hat{a}, \\
[\hat{a}^\dagger, H] &= \hbar\omega(\hat{a}^\dagger\hat{a}^\dagger\hat{a} + \frac{1}{2}\hat{a}^\dagger - \hat{a}^\dagger\hat{a}\hat{a}^\dagger - \frac{1}{2}\hat{a}^\dagger) = \hbar\omega(\hat{a}^\dagger[\hat{a}^\dagger, \hat{a}]) = -\hbar\omega\hat{a}^\dagger.
\end{aligned} \tag{1.38}$$

These operators do share an eigenbasis with the Hamiltonian which can be shown because an eigenfunction with a raising or lowering operator acting on it is still an eigenfunc-

tion of the Hamiltonian:

$$\begin{aligned}\hat{H}\hat{a}\left|\varepsilon\right\rangle &= (\hat{a}\hat{H} - [\hat{a},\hat{H}])\left|\varepsilon\right\rangle \\ &= \hat{a}\hat{H}\left|\varepsilon\right\rangle - \hat{a}\left|\varepsilon\right\rangle \\ &= (\varepsilon - 1)\hat{a}\left|\varepsilon\right\rangle\end{aligned} \tag{1.39}$$

Note, however that the eigenfunction $\hat{a}\left|\varepsilon\right\rangle$ has the eigenvalue of an eigenfunction with one less unit of energy. This is where the moniker 'raising' and 'lowering' comes from as $\hat{a}$ lowers eigenfunctions by one unit and $\hat{a}^\dagger$ increases them.

These raising and lowering operators can similarly be used in the case of the electron with an applied magnetic field. Using ξ and η as previously defined, $\hat{a}$ and $\hat{a}^\dagger$ become:

$$\begin{aligned}\hat{a} &\to \sqrt{\frac{m\omega}{2\hbar}}(\frac{p_x}{eB_z} + \frac{y}{2}) + i\sqrt{\frac{1}{2\hbar\omega m}}(p_y - \frac{eB_z}{2}x), \\ &= \sqrt{\frac{m}{2\hbar}\frac{eB_z}{m}}\frac{1}{eB_z}(p_x + \frac{eB_z}{2}y) + i\sqrt{\frac{1}{2\hbar m}\frac{m}{eB_z}}(p_y - \frac{eB_z}{2}x), \\ &= \sqrt{\frac{1}{2\hbar eB_z}}(p_x + \frac{eB_z}{2}y + ip_y - \frac{ieB_z}{2}x). \\ \hat{a}^\dagger &\to \sqrt{\frac{m\omega}{2\hbar}}(\frac{p_x}{eB_z} + \frac{y}{2}) - i\sqrt{\frac{1}{2\hbar\omega m}}(p_y - \frac{eB_z}{2}x), \\ &= \sqrt{\frac{1}{2\hbar eB_z}}(p_x + \frac{eB_z}{2}y - ip_y + \frac{ieB_z}{2}x).\end{aligned} \tag{1.40}$$

Note that had these gymnastics been calculated with a symbolic vector potential A, $\hat{a}$ and $\hat{a}^\dagger$ are functions of just momentum. Recall that $A = (-\frac{1}{2}B_z y, \frac{1}{2}B_z x, 0)$.

$$\begin{aligned}\hat{a} &= \sqrt{\frac{1}{2\hbar eB_z}}(p_x - eA_x + ip_y - ieA_y), \\ \hat{a}^\dagger &= \sqrt{\frac{1}{2\hbar eB_z}}(p_x - eA_x - ip_y + ieA_y),\end{aligned} \tag{1.41}$$

All this algebra is attempting to work towards a form of the graphene Hamiltonian which can utilize these raising and lowering operators. Using Eq. 1.24, an applied magnetic field is included in the same way; the momentum must now include the vector potential: $p \to p - eA$.

$$\hat{H} = v\begin{pmatrix} 0 & (p_x - eA_x) - i(p_y - eA_y) \\ (p_x - eA_x) + i(p_y - eA_y) & 0 \end{pmatrix}. \tag{1.42}$$

By inspection, the previously defined raising and lowering operators can be directly included and the Hamiltonian becomes very simple:

$$\hat{H} = v\sqrt{2\hbar eB_z}\begin{pmatrix} 0 & \hat{a}^\dagger \\ \hat{a} & 0 \end{pmatrix}. \tag{1.43}$$

With this new Hamiltonian, the eigenvalues may be found in similar fashion to the previous derivation. Again, as in the tight-binding derivation of the dispersion, these matrices represent separate wavefunctions on each sublattice, 1 or 2.

$$v\sqrt{2\hbar eB_z}\begin{pmatrix} 0 & \hat{a} \\ \hat{a}^\dagger & 0 \end{pmatrix}\begin{pmatrix} c_1 \\ c_2 \end{pmatrix} = E\begin{pmatrix} c_1 \\ c_2 \end{pmatrix}. \tag{1.44}$$

$$\begin{aligned} c_1 &\rightarrow \frac{v\sqrt{2\hbar eB_z}}{E}\hat{a}c_2, \\ \text{another substitution: } E\cancel{c_2} &= v\sqrt{2\hbar eB_z}\hat{a}^\dagger(\frac{v\sqrt{2\hbar eB_z}}{E}a\cancel{c_2}), \\ E^2 &= 2\hbar eB_z v^2\hat{a}^\dagger\hat{a}, \\ E &\rightarrow \pm\sqrt{2\hbar eB_z v^2 n}, \end{aligned} \tag{1.45}$$

The previous calculations assured that $\hat{a}$ and $\hat{a}^\dagger$ were normalized, thus $\hat{a}^\dagger\hat{a} = \hat{n}$, the number operator which counts in integers. Here, it counts the number of electrons in a given sublattice. Thus, for linear dispersion in momentum, Landau levels induced by a perpendicular field have square root integer dispersion. Chapter 2 will derived how STS can probe the density of states for a material, and in Chapter 5 Landau levels following $E \propto \sqrt{n}$ will be displayed for graphene. The last section of Chapter 1 will illustrate how strain gradients can cause electrons to behave as though there is an applied magnetic field and how the Landau levels visible in Chapter 5 can result from these pseudo-magnetic fields.

1.3.2 Landau Levels in Graphene with a Bandgap

The previous section derived Landau levels in pristine graphene. The graphene from nitrogen-seeded SiC however shows a band gap in angle-resolved photoelectron spec-

troscopy (ARPES), so it is important to asses how the Landau level energy dependence will shift when a band gap is included in the derivation.

Still using raising and lowering operators, return to the Hamiltonian in Eq. 1.43. To induce a band gap in the spectra, the easiest theoretical model is to include asymmetric terms in the A and B graphene sublattices, namely to include inequivalent diagonal terms:

$$\hat{H} = v\sqrt{2\hbar e B_z}\begin{pmatrix} \frac{\Delta}{2} & \hat{a} \\ \hat{a}^\dagger & -\frac{\Delta}{2} \end{pmatrix} \tag{1.46}$$

Solve for eigenvalues as before:

$$v\sqrt{2\hbar e B_z}\begin{pmatrix} \frac{\Delta}{2} & \hat{a} \\ \hat{a}^\dagger & -\frac{\Delta}{2} \end{pmatrix}\begin{pmatrix} \psi_1 \\ \psi_2 \end{pmatrix} = E\begin{pmatrix} \psi_1 \\ \psi_2 \end{pmatrix}, \tag{1.47}$$

$$\begin{cases} \frac{\Delta}{2}\psi_1 + \hat{a}\psi_2 = \frac{E}{v\sqrt{2\hbar e B_z}}\psi_1 \\ \hat{a}^\dagger\psi_1 - \frac{\Delta}{2}\psi_2 = \frac{E}{v\sqrt{2\hbar e B_z}}\psi_2 \end{cases}$$

$$\psi_1 \to \frac{\hat{a}}{E/(v\sqrt{2\hbar e B_z}) - \Delta/2}\psi_2.$$

$$\text{with substitution: } \hat{a}^\dagger(\frac{\hat{a}}{E/(v\sqrt{2\hbar e B_z}) - \Delta/2}\cancel{\psi_2}) - \frac{\Delta}{2}\cancel{\psi_2} = \frac{E}{v\sqrt{2\hbar e B_z}}\cancel{\psi_2}, \tag{1.48}$$

$$\hat{a}^\dagger\hat{a} = \hat{n} = (\frac{E}{v\sqrt{2\hbar e B_z}} - \frac{\Delta}{2})(\frac{E}{v\sqrt{2\hbar e B_z}} + \frac{\Delta}{2}).$$

$$E \to \sqrt{2\hbar v^2 e B_z(n - \frac{\Delta^2}{4})}.$$

Again, the solution is for integer values of $n = 0, \pm1, \pm2...$ With a bandgap in graphene, Landau levels shift to allow for a Δ sized gap, creating an $n = 0$ level for both conduction and valence bands at $E \propto \pm\frac{1}{2}\Delta$ [17].

1.4 Graphene Under Strain

As mentioned in the previous section, strain can cause electrons in graphene to behave as if there were an applied field; strain-induced fields of this type are known as pseudo-magnetic

fields. Pseudo-magnetic fields in graphene can be defined in terms of the lattice strain, and may be affected by the lattice orientation with respect to strain gradients. These pseudo fields are found in essentially any graphene lattice which has height variations or ripples. This section will first consider strain as defined for an elastic membrane and the apply these considerations to graphene. The last sections will derive the connection between strain and a pseudo-magnetic field and will compare the magnitude of the strain-causing graphene ripples and these pseudo fields. One of the main relationships derived subsequently highlights that pseudo-magnetic field magnitudes are directly proportional to the change in gradient of a ripple's slope; it is the strain gradients which induce pseudo fields and thus if a ripple is severe and condenses a change in height to a small length, the pseudo field may be very large despite the tiny atomic scale of the area. Another key result is that pseudo fields are influenced by the orientation of the graphene lattice with respect to a strain gradient. A pseudo field will not be induced if the strain gradient is oriented along the armchair axis, for instance. This rotational dependence of pseudo field magnitude maps to the symmetry of the graphene lattice (as expected) and thereby exhibits three-fold rotational symmetry.

The following relationships will be derived in this section: (1) A direct relationship between a pseudo-magnetic field and strain for a graphene lattice (2) An expression for the pseudo-magnetic field induced by 1D sinusoidal ripples, and (3) The dependence of a pseudo-magnetic field on the angle of a pleat in the graphene with respect to the zigzag axis of the graphene lattice. Table 1.1 lays out these expressions explicitly and gives cross-references for clarity (many of the constants are defined in the following sections).

1.4.1 The Strain Tensor in Graphene

The strain tensor u_{ij} is a unitless percentage-like measure of the strain in every direction in a defined region. Fig. 1.3 shows a figure which is strained enough to change length by $\Delta L = L - L_0$. The length change is a result of the displacement at point A, u_x, and the displacement at point B. The total change is equal to the displacement at A plus the change in the displacement over that distance: $u_x + \Delta u_x$ [18].

Pseudo Field	B	$\nabla \times A = \frac{\delta A_y}{\delta x} - \frac{\delta A_x}{\delta y}$	Page 12
Vector Potential	(A_x, A_y)	$\frac{\sqrt{3}\hbar\beta}{2ae}(u_{xx} - u_{yy}, -2u_{xy})$	Eq. 1.67, Page 26
Height Function for 1D Ripple	$h(y)$	$h\sin(\frac{2\pi y}{w})$	Eq. 1.69, Page 28
Pseudo Field for 1D Ripple	B_{1D}	$-\frac{2\sqrt{3}\hbar\beta}{ae}\frac{\pi^3 h^2}{w^3}\sin(\frac{4\pi y}{w})$	Eq. 1.71, Page 29
Pseudo Field for 1D Ripple at θ from Zigzag Axis	$R[3\theta]A$	$B_{1D}\cos(3\theta)$	Eq. 1.72, Page 30

Table 1.1: Derived Relationships in Strained Graphene

An overall change in length due to strain can be calculated by the strain tensor. The strain tensor components are defined as:

$$u_{ij} = \frac{\delta u_i}{\delta r_j} = \frac{1}{2}(\frac{\delta u_i}{\delta r_j} + \frac{\delta u_j}{\delta r_i}). \tag{1.49}$$

This can be shown to be equivalent to the change in overall length, as follows:

$$\begin{aligned} &\frac{\Delta L}{L_0} = \frac{L - L_0}{L_0} = \frac{u_x - (u_x + \Delta u_x)}{\Delta x} = \frac{\Delta u_x}{\Delta x}. \\ &u_{xx} = \frac{\delta u_x}{\delta x} \simeq \frac{\Delta u_x}{\Delta x} \to \frac{\Delta L}{L_0}. \end{aligned} \tag{1.50}$$

In 2D, the strain tensor has four components:

$$u_{ij} = \begin{pmatrix} u_{xx} & u_{xy} \\ u_{yx} & u_{yy} \end{pmatrix} \tag{1.51}$$

Tensors may be rotated using a rotation matrix through a unitary transformation (the given rotation matrix R is a clockwise rotation for example). u^O gives the original strain tensor, and u^R the strain tensor after rotation. R^T is the standard transpose of the rotation

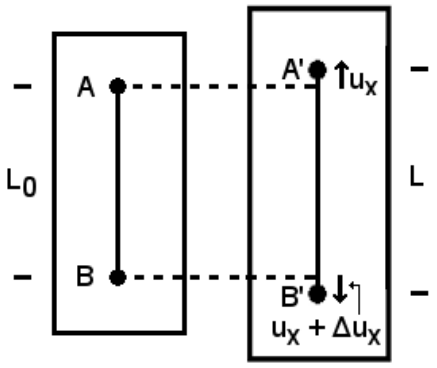

Figure 1.3: Linear strain along one axis. The displacement vector u and length before and after strain, L_0 and L, are defined.

matrix.

$$u^R = R\, u^O\, R^T, \text{ for e.g.: } R = \begin{pmatrix} \cos(\theta) & \sin(\theta) \\ -\sin(\theta) & \cos(\theta) \end{pmatrix}. \tag{1.52}$$

1.4.2 A Strained Graphene Lattice

A relationship between the electron hopping potential t and the strain tensor is required to understand the effects of strain on graphene through the lens of the previous tight binding derivation. In particular, consider the relationship between the hopping potential and the nearest neighbor vectors of the graphene crystal lattice described by a particular strain tensor. The overlap integral between two sublattices was previously defined as $H_{AB} = t_0 f(k)$ in Eq. 1.12. As two atoms are strained and approach or retreat from each other as a result, both the nearest neighbor vectors δ_i and t_0 would be expected to change. For simplicity all of the change to the overlap integral is assumed to be wrapped up in individual t values for each atomic pair.

Fig. 1.4 illustrates strained lattice vectors, defining ρ_i as the vector between two unstrained atoms in a crystal, u_0 and u_i as individual displacements for atoms, and ρ_i' as the vector between the atoms after strain.

From this, it may be seen that $\rho_i' = u_i + \rho_i - u_0$. For $a_C = 1.42$ Å, let δa_i be the change in the carbon-carbon spacing after displacement. For the unstrained lattice vector

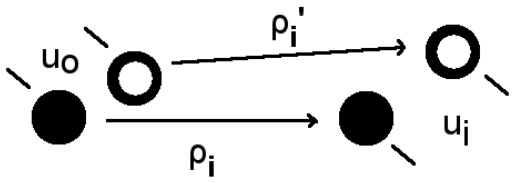

Figure 1.4: Lattice vectors before and after strain. The solid circles represent unstrained atoms; the ring-circles those same atoms after strain causes displacement. The displacement vectors u_o and u_i and the lattice vectors before and after strain ρ_i and ρ_i' are illustrated.

$|\rho_i| = a_C$.

$$\delta a_i = |\rho_i'| - |\rho_i| = \sqrt{\rho_i^2 + 2\rho_i(u_i - u_0)} - a_C \tag{1.53}$$

This treatment neglects the $(u_i - u_0)^2$ term from $\rho_i'^2$ as being too small. A Taylor expansion around $(u_i - u_0) \simeq 0$ will simplify this expression:

$$\begin{aligned}\sqrt{\rho_i^2 + 2\rho_i(u_i - u_0)} &\simeq (\rho_i^2)^{1/2} + \frac{1}{2}(\rho_i^2)^{-1/2} 2\rho_i \cdot (u_i - u_0) - a_C, \\ &= a_C + \frac{\rho_i \cdot (u_i - u_0)}{a_C} - a_C = \frac{\rho_i \cdot (u_i - u_0)}{a_C}\end{aligned} \tag{1.54}$$

This is now an expression of the change in lattice constant after strain, δa_i, however it is the hopping parameter after strain which is of particular interest. The function may be expanded with a derivative, and multiplying by $(ta_C/a_C t)$ will transform the derivative into a derivative of the natural log of the variables t and a_C. This in turn is a definition of the Grüneisen parameter $\beta = -d\ln(t)/d\ln(a_C)$, a known material constant which is $\sim$2 for graphene [19].

$$\begin{aligned}t_i &= t(\rho_i + (\rho_i' - \rho_i)), \\ &= t(\rho_i) + (\frac{a_C}{t}\frac{dt}{d\rho})(\rho_i' - \rho_i)\frac{t}{a_C}, \\ &= t + \frac{d\ln(t)}{d\ln(a_C)}\frac{\rho_i \cdot (u_i - u_0)}{a_C}\frac{t}{a_C}, \\ &= t - \frac{\beta t}{a_C^2}\rho_i \cdot (u_i - u_0).\end{aligned} \tag{1.55}$$

To continue, $(u_i - u_0)$ may be expanded as well. u_i was previously defined to be the strain-induced displacement of lattice vector ρ_i, u_0 is the displacement of ρ_0 and so on, thus u is a function of ρ: $u_0 = u(\rho_0)$. Consider first the relation between the x-axis components of the displacement of two near neighbors:

$$\begin{aligned} u_{ix} &= u_x(\rho_0) + \nabla u_x \cdot \rho_i, \\ u_{ix} - u_{0x} &= \nabla u_x \cdot \rho_i = \rho_i \cdot \nabla u_x, \\ u_i - u_0 &= \rho_i \cdot \nabla u. \end{aligned} \tag{1.56}$$

The last line returns to considering the complete vectors, not just the x-axis component, and the switch in order is achieved because dot products commute. This results in a formula for the inhomogenous hopping potential [11]:

$$t_i = t - \frac{\beta t}{a_C^2} \rho_i \cdot (\rho_i \cdot \nabla u). \tag{1.57}$$

1.4.3 Strain-induced Pseudo-magnetic Fields

The individual hopping parameters previously defined create a gauge field in the graphene lattice. This is termed a strain-induced pseudo-magnetic field; in the following it may be seen how although the alterations to graphene's electronic structure result solely from strain gradients within the lattice, the mathematical formalism is identical to the application of a magnetic field. As a result, the theoretical framework for applied magnetic fields in graphene may similarly be used to describe strain-induced pseudo-magnetic fields.

Recall the calculation of the graphene tight-binding Hamiltonian's off-diagonal terms which were overlap integrals between the A and B sublattices, Eq. 1.12. Strain will now be modeled as individual hopping probabilities, t_i, for each nearest neighbor pair. Eq. 1.57 showed that these individual t_i values can be directly related to the strain tensor. The graphene Hamiltonian may now be re-derived, concentrating on calculating H_{AB} starting from before t_0 was factored out. Let $\delta k = k - K = q$, and the following will proceed assuming that q is a small momentum with respect to the K point. For a zigzag lattice, $K^{\pm} = \pm(4\pi/3a, 0)$ for lattice constant $a = 2.46$ Å. Recall the nearest neighbor vectors in

a zigzag lattice are:

$$\delta_1 = (-\frac{a}{2}, \frac{a}{2\sqrt{3}}), \quad \delta_2 = (\frac{a}{2}, \frac{a}{2\sqrt{3}}), \quad \delta_3 = (0, -\frac{a}{\sqrt{3}}). \tag{1.58}$$

The off diagonal overlap integral will now be calculated for the positive K^+ point with individual hopping parameters. The nearest neighbor phase (exponential) terms will immediately be expanded to first order, assuming q is small.

$$\begin{aligned}
H_{AB} =& -\sum_{i=1}^{3} t_i e^{iK\cdot\delta_i} e^{iq\cdot\delta_i}, \\
=& -t_1 e^{-i(\frac{4\pi}{3a})(\frac{a}{2})}(1 + i(-\frac{a}{2}q_x + \frac{a}{2\sqrt{3}}q_y)) \\
& - t_2 e^{i(\frac{4\pi}{3a})(\frac{a}{2})}(1 + i(\frac{a}{2}q_x + \frac{a}{2\sqrt{3}}q_y)) - t_3 e^0 (1 + i(-\frac{a}{\sqrt{3}}q_y)), \\
=& -t_1(-\frac{1}{2} - \frac{i\sqrt{3}}{2})(1 - \frac{ia}{2}q_x + \frac{ia}{2\sqrt{3}}q_y) \\
& - t_2(-\frac{1}{2} + \frac{i\sqrt{3}}{2})(1 + \frac{ia}{2}q_x + \frac{ia}{2\sqrt{3}}q_y) - t_3(1 - \frac{ia}{\sqrt{3}}q_y), \\
=& q_x a(\frac{i}{4}(t_2 - t_1) + \frac{\sqrt{3}}{4}(t_1 + t_2)) + q_y a(\frac{i}{4\sqrt{3}}(t_1 + t_2 + 4t_3) \\
& + \frac{1}{4}(t_2 - t_1)) + (\frac{i\sqrt{3}}{2}(t_1 - t_2) + \frac{1}{2}t_1 + \frac{1}{2}t_2 - t_3),
\end{aligned} \tag{1.59}$$

As a check on the algebra, if the magnitude of each hopping potential is considered equal, $t_i \approx t_0$, the original low energy Hamiltonian should reappear. Toward that end, consider the equation after neglecting differences between hopping parameters, $(t_i - t_j)$, since $t_i \approx t_j \approx t_0$ the terms are very small. Terms which are a sum will be estimated as an average value of the hopping integrals, $\bar{t} \approx t_0$.

$$\begin{aligned}
H_{AB} =& q_x a(\cancel{\frac{i}{4}(t_2 - t_1)} + \frac{\sqrt{3}}{4}(t_1 + t_2)) + q_y a(\frac{i}{4\sqrt{3}}(t_1 + t_2 + 4t_3) \\
& + \cancel{\frac{1}{4}(t_2 - t_1)}) + (\cancel{\frac{i\sqrt{3}}{2}(t_1 - t_2)} + \cancel{(\frac{1}{2}t_1 + \frac{1}{2}t_2 - t_3)}, \\
=& \frac{\sqrt{3}}{2}\bar{t}q_x a + \frac{6}{4\sqrt{3}}\bar{t}iq_y a = \frac{\sqrt{3}}{2\hbar}\bar{t}a(p_x + ip_y)
\end{aligned} \tag{1.60}$$

The result is reassuringly similar to the linear dispersion near K which was derived earlier in Eq. 1.23. If, however, the individual hopping parameters are maintained, the terms may not be neglected quite so ruthlessly. That $q_i a$ is a small value is intrinsic to both the earlier linear low energy expansion and the following. As the terms involving subtraction of hopping parameters are also small, the small terms multiplied by small terms may be neglected; they become an order of magnitude smaller. Similarly, this argument allows the use of the average hopping parameter $\bar{t}$ for the momentum terms. After these approximations, the remaining terms may be redefined or modeled as a vector potential arising from the strain which created the individual hopping parameters in the first place. Recall the Fermi velocity $= (\sqrt{3}at_0)/(2\hbar)$.

$$\begin{aligned}
H_{AB} &= q_x a(\cancel{\frac{i}{4}(t_2 - t_1)} + \frac{\sqrt{3}}{4}(t_1 + t_2)) + q_y a(\frac{i}{4\sqrt{3}}(t_1 + t_2 + 4t_3) \\
&\quad + \cancel{\frac{1}{4}(t_2 - t_1)}) + (\frac{i\sqrt{3}}{2}(t_1 - t_2) + (\frac{1}{2}t_1 + \frac{1}{2}t_2 - t_3), \\
&= \frac{\sqrt{3}}{2}\bar{t}q_x a + \frac{3}{2\sqrt{3}}\bar{t}iq_y a + \frac{i\sqrt{3}}{2}(t_1 - t_2) + \frac{1}{2}(t_1 + t_2 - 2t_3), \\
&= \frac{\sqrt{3}a}{2\hbar}\frac{\hbar}{a}\bar{t}q_x a + \frac{\sqrt{3}a}{2\hbar}\frac{\hbar}{a}\bar{t}iq_y a + \frac{\sqrt{3}a}{2\hbar}\frac{\hbar}{a}t_0 i(\frac{t_1}{t_0} - \frac{t_2}{t_0}) \\
&\quad + \frac{\sqrt{3}a}{2\hbar}\frac{\hbar}{a\sqrt{3}}t_0(\frac{t_1}{t_0} + \frac{t_2}{t_0} - 2\frac{t_3}{t_0}), \\
&= v\hbar q_x + vi\hbar q_y + v\frac{i\hbar}{at_0}(t_1 - t_2) + v\frac{\hbar}{\sqrt{3}a}(t_1 + t_2 - 2t_3).
\end{aligned} \tag{1.61}$$

Let a vector potential be defined as:

$$\begin{aligned}
A_x &\equiv -\frac{\hbar}{\sqrt{3}at_0 e}(t_1 + t_2 - 2t_3), \\
A_y &\equiv -\frac{\hbar}{at_0 e}(t_1 - t_2),
\end{aligned} \tag{1.62}$$

This reveals a familiar form for the graphene Hamiltonian's off diagonal terms again:

$$H_{AB} = v(p_x - eA_x + ip_y - ieA_y). \tag{1.63}$$

The complex conjugate provides the alternate off-diagonal term. The full Hamiltonian

becomes:

$$H = v \begin{pmatrix} 0 & (p_x - eA_x) - i(p_y - eA_y) \\ (p_x - eA_x) + i(p_y - eA_y) & 0 \end{pmatrix} \tag{1.64}$$

Recall Eq. 1.57 which related the individual hopping parameters and the strain tensor:

$$t_i = t_0 - \frac{3\beta t}{a^2}\delta_i(\delta_i \cdot \nabla) \cdot u. \tag{1.65}$$

This can be used to directly relate the vector potential to the strain tensor as well. Recall $a_C = a/\sqrt{3}$; the following will use the lattice parameter a instead of a_C. For a zigzag lattice:

$$\begin{aligned} t_1 &= t_0 - \frac{3\beta t}{4}(u_{xx} + \frac{1}{3}u_{yy} - \frac{1}{\sqrt{3}}(u_{xy} + u_{yx})), \\ t_2 &= t_0 - \frac{3\beta t}{4}(u_{xx} + \frac{1}{3}u_{yy} + \frac{1}{\sqrt{3}}(u_{xy} + u_{yx})), \\ t_3 &= t_0 - \beta t u_{yy}. \end{aligned} \tag{1.66}$$

The vector potential becomes:

$$\begin{aligned} A_x =& -\frac{\hbar}{\sqrt{3}aet_0}(t_1 + t_2 - 2t_3), \\ =& -\frac{\sqrt{3}\hbar}{3aet_0}(\cancel{t_0} - \frac{3\beta t_0}{4}(u_{xx} + \frac{1}{3}u_{yy} - \cancel{\frac{1}{\sqrt{3}}(u_{xy} + u_{yx})}) \\ & + \cancel{t_0} - \frac{3\beta t_0}{4}(u_{xx} + \frac{1}{3}u_{yy} + \cancel{\frac{1}{\sqrt{3}}(u_{xy} + u_{yx})}) \\ & - \cancel{2t_0} + 2\beta t_0 u_{yy}, \\ =& \frac{\sqrt{3}\hbar\beta}{2ae}(u_{xx} - u_{yy}). \\ A_y =& -\frac{\hbar}{aet_0}(t_1 - t_2), \\ =& -\frac{\hbar}{aet_0}(\cancel{t_0} - \frac{3\beta t_0}{4}(\cancel{u_{xx}} + \frac{1}{\cancel{3}}\cancel{u_{yy}} - \frac{1}{\sqrt{3}}(u_{xy} + u_{yx})) \\ & - \cancel{t_0} + \frac{3\beta t_0}{4}(\cancel{u_{xx}} + \frac{1}{\cancel{3}}\cancel{u_{yy}} + \frac{1}{\sqrt{3}}(u_{xy} + u_{yx}))), \\ =& -\frac{\sqrt{3}\hbar\beta}{ae}u_{xy}. \end{aligned} \tag{1.67}$$

This derivation is equivalent to similar derivations of the strain field algebra derived by Katsnelson as well as others [11, 20, 14, 21].

1.4.4 The Pseudo-magnetic Fields of a Graphene Ripple

These derivations imply that every topographic feature in graphene will change the atomic spacing of the carbon incrementally and thereby induce pseudo-magnetic fields in the graphene. The simplest calculation to model pseudo fields in graphene is to consider 1D ripples creating uniaxial strain in a graphene lattice. Several calculations of this problem can be found in the literature [14, 22]. Short of calculating a pseudo field from an atomistic model at every carbon atom in the film [23], the strain tensor for a given film can be approximated using elastic theory. For 1D ripples, assuming a sinusoidal form along the x-axis, the arc length of a section Δs can be found from a function describing the height $h(x, y)$. For a ripple of height h and width w, in the regime where $h/w \ll 1$ the arc length can be approximated by $\Delta s \approx (1 + \frac{1}{2}h'(y)^2)dy$. Therefore in this regime, $u_y \approx (\Delta s - \Delta y)/\Delta y = \frac{1}{2}h'(y)^2$. This approximation is illustrated in Fig. 1.5

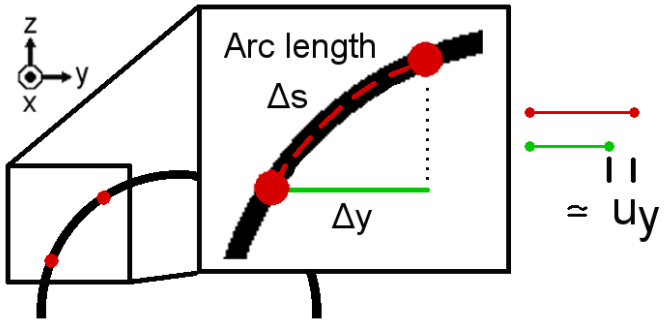

Figure 1.5: The strain-induced displacement caused by a ripple, u_y, can be approximated by the difference between the projected distance between two atoms along an axis, Δy and the arc length Δs.

In 2D, allowing for a height function inducing deformations in x and y, the strain tensor

becomes [14, 24, 18]:

$$\begin{aligned} u_{xx} &= \frac{\delta u_x}{\delta x} + \frac{1}{2}\frac{\delta h(x,y)}{\delta x}^2, \\ u_{yy} &= \frac{\delta u_y}{\delta y} + \frac{1}{2}\frac{\delta h(x,y)}{\delta y}^2, \\ u_{xy} &= \frac{1}{2}(\frac{\delta u_x}{\delta y} + \frac{\delta u_y}{\delta x}) + \frac{1}{2}\frac{\delta h(x,y)}{\delta x}\frac{\delta h(x,y)}{\delta y}. \end{aligned} \tag{1.68}$$

The vector potential can now be calculated for $u_y = \frac{1}{2}h'(y)^2$ given a height function. If 1D ripples are modeled by a sine function ripple along the y-axis with height h and period $2\pi/w$, u_{yy} may be assumed to be the only non-zero component to the strain tensor. The 1D ripples are assumed to only strain the lattice along the axis perpendicular to the ridge of a ripple.

$$\begin{aligned} h(y) &= h\sin(\frac{2\pi y}{w}). \\ \frac{\delta h(y)}{\delta y} &= \frac{2\pi h}{w}\cos(\frac{2\pi y}{w}), \\ u_y &= \frac{1}{2}h'(y)^2 = \frac{2\pi^2 h^2}{w^2}\cos^2(\frac{2\pi y}{w}), \\ \frac{\delta u_y}{\delta y} &= -\frac{8\pi^3 h^2}{w^3}\sin(\frac{2\pi y}{w})\cos(\frac{2\pi y}{w}), \\ u_{yy} &= \frac{\delta u_y}{\delta y} + \frac{1}{2}(\frac{\delta h(x,y)}{\delta y})^2, \\ &= \frac{2\pi^2 h^2}{w^2}\cos^2(\frac{2\pi y}{w}) - \frac{4\pi^3 h^2}{w^3}\sin(\frac{4\pi y}{w}). \end{aligned} \tag{1.69}$$

The pseudo field may now be calculated, assuming $u_{yy} \neq 0$ and $u_{xx} = u_{xy} = 0$.

$$\begin{aligned} A_x &= \frac{\sqrt{3}\hbar\beta}{2ae}(\cancel{u_{xx}} - u_{yy}), \\ A_y &= -\frac{\sqrt{3}\hbar\beta}{ae}\cancel{u_{xy}}, \\ B &= \nabla \cdot A = \frac{\cancel{\delta A_y}}{\cancel{\delta x}} - \frac{\delta A_x}{\delta y} = \frac{\sqrt{3}\hbar\beta}{2ae}\frac{\delta}{\delta y}u_{yy}, \\ &= -\frac{2\sqrt{3}\hbar\beta\pi^3 h^2}{aew^3}\sin(\frac{4\pi y}{w}) - \frac{8\sqrt{3}\hbar\beta\pi^4 h^2}{aew^4}\cos(\frac{4\pi y}{w}). \end{aligned} \tag{1.70}$$

So long as $h \ll w$ holds as an approximation, or more particularly $h \ll w/16\pi$, the pseudo-magnetic field is essentially a sine function at twice the period of the original 1D

ripples:

$$B \propto -\frac{2\sqrt{3}\hbar\beta}{ae}\frac{\pi^3 h^2}{w^3}\sin(\frac{4\pi y}{w}). \tag{1.71}$$

This is plotted in Fig. 1.6, illustrating the pseudo-magnetic field of a 1D ripple against the height function of the ripple. It is the change in gradient of the ripple's slope that most effects the magnitude of the pseudo field.

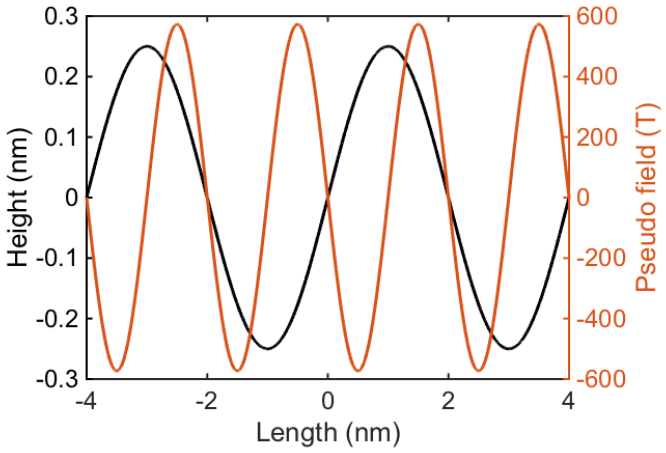

Figure 1.6: A 1D sinusoidal ripple profile (black) plotted against the strain-induced pseudo-magnetic field magnitude (red) induced by the curvature of the ripple. The ripple profile is Eq. 1.69 plotted with h=0.5 nm and w=4 nm, and the pseudo field is Eq. 1.71.

Several calculations have been made as to the size of wrinkle required before the induced pseudo field is visible by experimental means. The pseudo-magnetic flux from a ripple is about $\sim[(h^2)/(wa_C)]\Phi_0$ for a ripple of width w, height h, and a flux quanta $\Phi_0 = (\hbar\pi)/e$ [14, 16]. For an applied perpendicular field it is known that there are $(N-1)$ zero energy states given N flux quanta. This leads to the prediction that pseudo fields will only be visible on ripples which satisfy $(h^2)/(wa_C) \geq 1$ [14, 22, 25].

This section modeled 1D ripples in graphene with a ridge line along the x-axis parallel to the zigzag axis and sinusoidal form along the y-axis. From the symmetries of the graphene lattice, a rotation of these 1D folds reveals that no pseudo-magnetic field magnitude is induced by folds with a ridge line parallel to the armchair axis [14, 26, 21]. This

must be considered in any model which considers a graphene ripple at a random angle to the lattice. The pseudo field dependence on angle is visible when a rotation is applied to the vector potential by first finding the strain tensor u^O in the rotated coordinates. u^O will denote the strain tensor in original coordinates, u^R in rotated coordinates. Analogous superscripts will be used for the vector potential A as well:

$$\begin{aligned} u^O &= R^T\, u^R\, R \\ (u^O_{xx} - u^O_{yy}) &= (u^R_{xx} - u^R_{yy})\cos 2\theta + 2u^R_{xy}\sin 2\theta, \\ -2u^O_{xy} &= (u^R_{xx} - u^R_{yy})\sin 2\theta - 2u^R_{xy}\cos 2\theta. \end{aligned} \tag{1.72}$$

Eq. 1.72 reproduces the strain tensor components of the vector potential (Eq. 1.67) with rotated strain tensor components. From this rotation of the strain tensor by $-\theta$, the rotated expression for the vector potential are by inspection also equal to a forward rotation of the vector potential by 2θ: $R[-\theta]A^O = R[2\theta]A^O$. This relation can equivalently be written as: $A = R[3\theta]A$, or that the graphene lattice symmetry creates three-fold symmetry in the pseudo-magnetic field [21, 26]. Chapter 5 will use this subsequently to model an off-axis ripple viewed via STM in NG graphene.

1.4.5 Bandgaps Induced by Pseudo-magnetic Fields

Pseudo-magnetic fields are theoretically predicted to induce a band gap in graphene under certain conditions [27]. As the pseudo field fluctuates following the topography of the graphene ripples, every region with a particular polarity of pseudo field is bounded by a region of alternate polarity. It is well known that in an inhomogenous magnetic environment, electrons travel by way of snake states along the transition region between two polarities; this is also the case for inhomogenous pseudo-magnetic fields, and is illustrated in Fig. 1.7(a) [28, 27]. Fig. 1.7(b) illustrates the case where a general potential is applied to this environment. It can be seen from this simplified view how a direct correlation between pseudo field and potential can localize all electron orbits in strained graphene. More precise calculations confirm this intuition finding that a pseudo-magnetic field in direct correlation

with an applied potential can induce a band gap of Δ where [29, 30, 27]:

$$\Delta \propto \int \frac{d^2k}{|k|^2} Im(U_{-k})(B_k). \tag{1.73}$$

Here, U_{-k} and B_k are the Fourier components of each oscillating field, potential and pseudo-magnetic, respectively. Simply, a gap is predicted to open in proportion to how directly these two fields are correlated. This theory will be considered with more detail in the context of graphene grown on nitrogen-seeded SiC in Chapter 5.

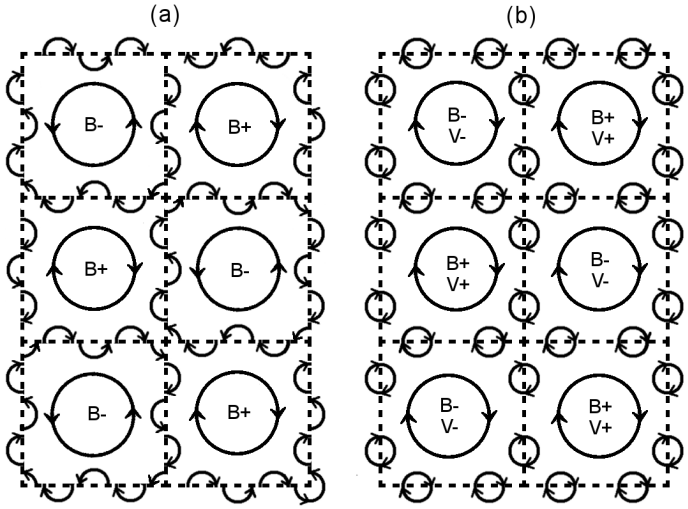

Figure 1.7: (a) Snake states in an inhomogenous magnetic field; six regions of alternating polarity are illustrated. (b) Snake states in an inhomogenous magnetic field with a correlated potential. Adapted from [31].

Chapter 2

Theory Behind Characterization Techniques

Several analysis techniques are used throughout this thesis to characterize graphene. A brief overview of the techniques and some of the grounding theory of the most heavily used tools in Chapters 3-5 is given here in Chapter 2. Characterization techniques considered include angle-resolved photoemission spectroscopy (ARPES), atomic force microscopy (AFM), Raman spectroscopy, and X-ray photoelectron spectroscopy (XPS). A more in-depth overview of scanning tunneling microscopy and spectroscopy (STM and STS) is also included, as well as a full derivation relating STS spectra to the local density of states for a sample.

2.1 Angle-resolved Photoemission Spectroscopy

Angle-resolved photoemission spectroscopy (ARPES) takes advantage of the conservation of energy and parallel crystal momentum to probe the valence band dispersion of a crystal structure. By collecting electrons ejected at a particular trajectory from a sample ARPES resolves the component of the electron's momentum parallel to the sample surface. By measuring the electron's energy, ARPES also resolves the energy of the electron's original

state with respect to the Fermi level. Fig. 2.1 and 2.2 illustrate the energies and geometry involved.

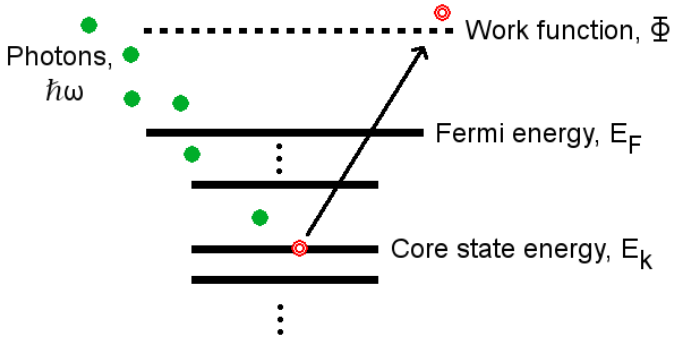

Figure 2.1: Definition of ARPES energy variables, core state (valence band) energy level E_k, work function Φ, and incident photon energy $\hbar\omega$.

A beam of incident photons is shot at a thin film and this causes valence band electrons to be ejected from the material. A single ejected electron starts at an original core state energy; this energy can be extracted because the incident photon energy is known and the change in energy should be proportional to the energy jump to vacuum for the electron: the energy to get to the Fermi level plus the work function. Fig. 2.1 and Eq. 2.1 illustrate how the desired core energy E_k may be extracted from an electron of energy E, the work function Φ, and the incident photon energy $\hbar\omega$.

$$E_k = \hbar\omega - \Phi - E. \tag{2.1}$$

As Fig. 2.2(a) illustrates, given the angle of the ejected electron and the crystal face of the probed material, the parallel component of the internal dispersion can be collected [32]. The perpendicular component of the momentum is not always conserved as the electron exits the sample, however. It is easiest to illustrate the connection assuming parabolic dispersion for both the electrons in the sample and after ejection. The primed variables all describe variables within the probed material, the unprimed variables are the electron that have been ejected. After equating the parabolic dispersion within the sample to the parabolic dispersion outside, the ejected electron's energy can be related to the internal

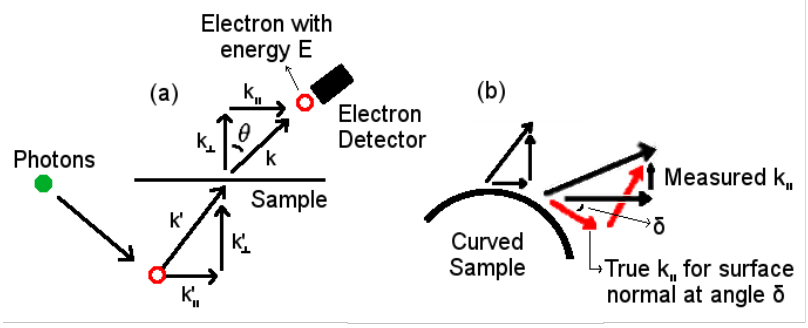

Figure 2.2: The angles involved in an ejected electron in ARPES. (a) An electron within the material (primed variables) is ejected and then collected at a particular angle θ. (b) Collected electrons with a surface normal at an angle δ to the macroscopic surface normal introduce. The apparent difference in the measured vs. true surface normal illustrates how surface roughness can introduce intensity broadening.

parallel momentum component as follows:

$$\begin{aligned} k_{\|} &= k'_{\|}. \\ E &= \frac{\hbar^2}{2m}(k_{\perp}^2 + k_{\|}^2), \\ k &= \sqrt{\frac{2m}{\hbar^2}E} \rightarrow k_{\|} = \sin\theta\sqrt{\frac{2m}{\hbar^2}E}. \\ k'_{\|} &= \sin\theta\sqrt{\frac{2m}{\hbar^2}E}. \end{aligned} \tag{2.2}$$

The rate of ejected photoelectrons collected for ARPES is low, thus a high intensity photon source of excellent energy precision is required for good ARPES data collection. As a result, ARPES often uses synchrotron radiation as a source; the Cassiopée synchrotron in Gif sur Yvette, France, was used to collect the ARPES spectra shown in Chapter 5.

Fig. 2.2(b) illustrates how error in $k_{\|}$ can result from surface roughness if the sample is not perfectly flat. For a curved surface, $k_{\|}$ is taken to be parallel to the macroscopic surface of the sample and if there is a discrepancy then the measured $k_{\|}$ becomes a projection of the true $k_{\|}$ vector. Fig. 2.2(b) highlights with red vectors the true $k_{\perp}$ and $k_{\|}$ vectors for a curved section of the surface. The black vectors show the $k_{\|}$ component which is actually measured, however. Fig. 2.2(b) greatly exaggerates the angles involved, but illustrates how

surface roughness can contribute to intensity broadening of a measured ARPES spectra. If the surface normal of a curved section is at an angle δ to the macroscopic normal, and the electron is collected at an angle of θ as in Fig. 2.2(a), then the measured $k_{m\|}$ can be related to the true $k_{t\|}$ by a proportion of the angles involved:

$$k_{m\|} = \left(\frac{\sin\theta}{\sin(\theta - \delta)} \right) k_{t\|}. \tag{2.3}$$

As derived in Chapter 1, the dispersion expected for graphene is a linear cone or 'X' shape. Chapter 5 discusses ARPES taken on graphene grown on nitrogen-seeded SiC, which displays an energy offset to the typical linear graphene dispersion as well as intensity broadening due to surface roughness.

2.2 Atomic Force Microscopy

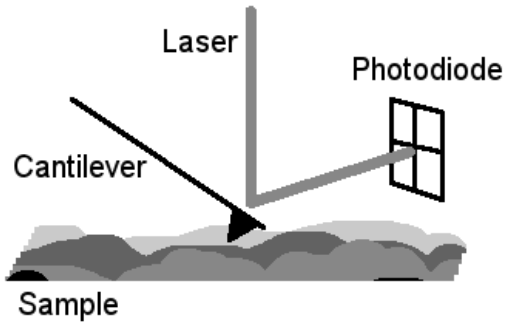

Figure 2.3: Atomic force microscopy cantilever tip and laser illustrated. The laser is reflected from the cantilever to a photodiode independently sensitive to movement in each quadrant [33].

Atomic force microscopy (AFM) is an imaging technique which is particularly sensitive to height variation on a sample surface. AFM is based on monitoring a sharp cantilever tip vibrating at resonance as the tip is lowered toward a surface until close enough that surface forces alter the resonant vibrating frequency. This setup is versatile, so that with minor changes to the tip the AFM can be sensitive to many different textural and topographic changes. The primary technique used in this thesis is tapping mode AFM wherein the

AFM tip never truly touches the surface of the sample, but closely follows the 3D contours with a resolution in height down to $\sim$1 nm [33]. A laser is reflected off of the tip to monitor the tip's heigh, tilt, and resonant frequency. The laser's reflection is sensed by four independent photodiodes which allow a feedback loop to respond to changes in topography very quickly. Fig. 2.3 shows a diagram of the AFM tip moving over a surface, with the laser reflection monitored by the four photodiodes.

Graphene is a very inert material under standard conditions, and it is relatively simple to use AFM to characterize graphene topography. Graphene typically has many ripples and pleats which are often large enough to be visible within AFM resolution. The atomic corrugations from graphene's honeycomb lattice are too small in x and y to resolve (with the exception of a few highly calibrated vacuum AFMs with particularly high resolution), but for mechanically exfoliated graphene on SiO_2, layer thicknesses may be resolved with AFM. Similarly step heights for sapphire and SiC may also be visible.

2.3 Raman Spectroscopy

Raman spectroscopy analyzes photons which are inelastically scattered from a solid sample. When a photon is inelastically scattered, one of the most common scattering mechanisms is an interaction with a phonon: a lattice vibration of a particular energy. These phonon interactions lead to scattering energy losses which are a function of the phonon's energy (as well as the photon) and enable some characterization of the phonon spectra present in a solid. Fig. 2.4 shows peaks at energies characteristic of phonons in several varieties of graphene.

In graphene, lacking defects to activate more, there are only a few low energy phonon states [34]. Fig. 2.4(a) illustrates a typical Raman spectrum for single layer graphene (CVD graphene on SiO_2) and (b), atomic illustrations of the phonon modes which correspond to these peaks. The most prominent peak is at $\sim$1575 cm^{-1} called the G peak which corresponds to a breathing mode phonon known as the E_{2g} mode. If there are defects in the graphene lattice then the D peak (the A_{1g} mode in Fig. 2.4(b)) can manifest and create a

peak at $\sim$1350 cm^{-1}. For graphene characterization, the most helpful peak is the 2D peak at $\sim$2700 cm^{-1} which is identified as a second harmonic of the D peak. While the D peak is present only if there are defects in the graphene lattice, the 2D peak is always present. This peak changes the most in correspondence with mechanical and electronic changes in a graphene sample, and thus is most often considered when Raman spectroscopy is used to estimate a graphene sample's quality. The D' is a minor peak at $\sim$1620 cm^{-1}, also associated with defects in the lattice and may create minor satellites to the G and 2D peaks in samples with very small domain sizes and frequent lattice defects [34].

In monolayer graphene, the 2D peak has one component and may be fit with a single Lorentzian. For bilayer and multilayer graphene the 2D peak has more components, a result of inter-layer coupling increasing the number of permitted phonon transitions in the system. This increase in peak components has been used to identify thicknesses from monolayer to five-layer graphene in exfoliated graphene on SiO_2, however is only present if the graphene in question is Bernal stacked [35, 36]. If there is negligible inter-layer coupling in a graphene sample then a multilayer graphene sample will still maintain a single-component 2D peak [37]. For samples of a known thickness, this may be used to identify samples with negligible inter-layer coupling.

The lattice domain size may be estimated from the relative peak intensities of the D and G peaks [38]. This estimation assumes that the defects which have caused the D peak are primarily domain boundaries, however there are many other types of defects possible in graphene, rendering this assumption often rather chancy. Point defects may be present in the center of domains for instance. When reasonable however, the crystal domain size in nm is of the order [39, 38]:

$$L_a = \frac{c}{E_l^4}\frac{I(G)}{I(D)}. \tag{2.4}$$

Either the D or D' peak may be used for this calculation, using the integrated intensity $I(D')$ for $I(D)$ as applicable above compared to the G peak intensity $I(G)$. The empirical constant c is $\sim$560 for the D peak and $\sim$160 for the D' peak and the laser energy E_l in [eV] is the laser used in the Raman spectroscopy setup. An Argon laser at 514.5 nm (2.41 eV)

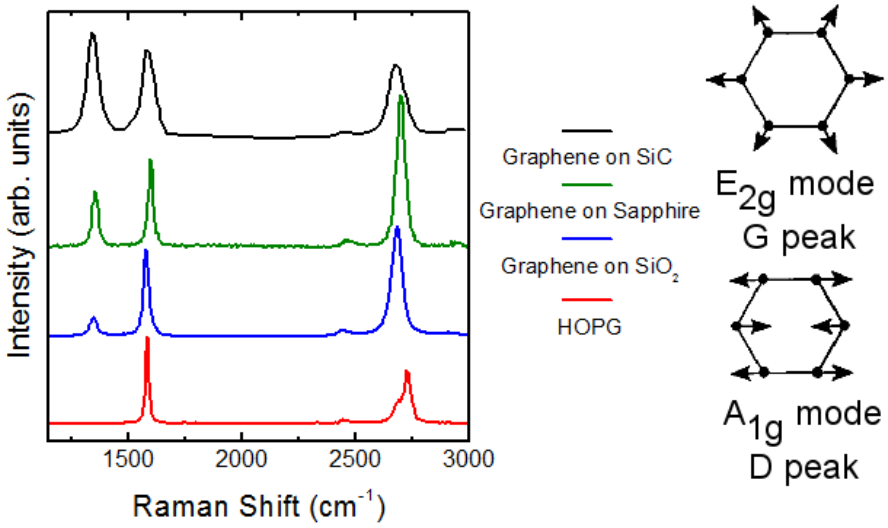

Figure 2.4: (a) Raman spectra for graphene grown on SiC with a SiC background subtracted (top, black), graphene grown on sapphire (second from top, green), CVD graphene grown on copper foil transferred to SiO_2 (Graphene on SiO_2, third from top, blue), and HOPG (bottom, red). Spectra are shifted vertically for clarity and are normalized in intensity to the G peak. (b) Illustration of lattice vibrations corresponding to the E_{2g} and A_{1g} phonon modes for graphene. Adapted from [37].

was used for the experimental spectra shown here and in Chapter 3. If the D peak is primarily induced by domain boundary defects, then the intensity ratio between D and D' should be $\sim$3.5, which calculation can serve as a check of whether the calculated domain size is reasonable [39].

Charge and strain are known to affect the graphene Raman spectrum by shifting peaks to either higher or lower frequencies depending on the disturbance. Vector analysis of peak shift trends may be used to separate whether strain or doping is shifting a particular peak [40], however without a very well known base spectrum for comparison it is sometimes difficult to detect the definitive origin of a shift. Particular substrates often induce uniform strain in graphene, for both epitaxially grown and mechanically transferred varieties, which can confuse the issue of a baseline spectrum [41–43]. Graphene transferred to a flexible substrate and then stretched has experimentally verified the magnitude of shifts of the 2D and G peaks due to uniaxial strain at least, which are -27.8 cm^{-1} to the 2D peak and -

14.2 cm^{-1} to the G peak per 1 % strain [44].

Unfortunately is it difficult to get absolute data from Raman characterization of graphene, but Raman affords a simple way to get a sense of sample quality. More in depth analysis can give insight into strain and doping, but might require another characterization technique to give a starting point for some peak shifts and widths.

2.4 Scanning Tunneling Microscopy and Spectroscopy

The scanning tunneling microscope (STM) was invented and implemented in the '80's by Binning, Rohrer, Gerber and Weibel. STM has since become a workhorse in the scientific community for surface structure characterization [45]. STM, similar to AFM, characterizes a surface by bringing a tip very close and scanning across the surface. The STM tip senses the surface through a tunneling current, however, not a resonant vibration. Also unlike AFM, STM uses independent piezoelectric transducers in x, y, and z and is an electrical technique requiring conductive probe tips and conductive samples. STM is very sensitive to the surface condition as well, therefore also works best with clean samples in ultra-high vacuum (UHV). Tungsten and platinum-iridium tips (PtIr) are the most common, as they have simple electrical wavefunctions and may be etched to atomically sharp points.

2.4.1 The Density of States via STM and STS

In everyday interaction, tunneling currents do not play a large role as the probability for an electron to tunnel out of a material to elsewhere falls exponentially with distance. However, as a metal tip is brought close to a sample (in the range of 1 nm [46]), when a bias is applied between sample and tip, a tunneling current becomes easily detectable (in the range of 0.1-10 nA).

A simple starting point to modeling the current of an STM tip is to consider the solution to a particle wavefunction impinging on a square potential barrier. Classically, for a wavefunction with energy less that that of the potential barrier, the particle should reflect

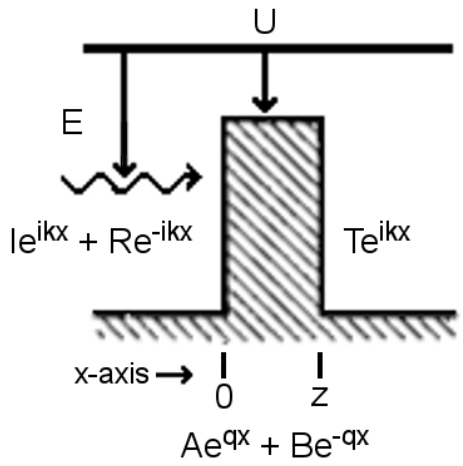

Figure 2.5: Tunneling through a square potential barrier of width z and height U by a particle with energy E. The three regions to the left, inside, and the right of the barrier are each assigned respective wavefunctions.

100 % of the time. Solving Schrödinger's equation for this system gives insight to the possibilities which appear when the problem is shrunk to the quantum regime. Particles may tunnel through with a non-zero probability, given a narrow enough barrier. The following derivation shows that this probability falls exponentially as the barrier width grows.

In the quantum regime, it is known that particles may be represented by a wavefunction which, to satisfy Schrödinger's equation, must be continuous throughout all regions [47, 16]. The following will consider a particle approaching from one direction only, which particle may be transmitted creating a transmission probability $|T|^2$ and a reflection probability $|R|^2$. The particle wavefunction will be modeled as summed plane waves with complex coefficients. Fig. 2.5 illustrates a barrier of height U and width z, and the three regimes which will subsequently be addressed. The three regimes generate 5 coefficients which need to be determined in order to find the ratio of transmitted to incident particles.

$$\psi = \begin{cases} Ie^{ikx} + Re^{-ikx} & x < 0 \\ Ae^{qx} + Be^{-qx} & 0 < x < z \\ Te^{ikx} & x > z. \end{cases} \tag{2.5}$$

The wavevectors $k = \sqrt{2mE/\hbar^2}$ and $q = \sqrt{2m(U-E)/\hbar^2}$ are used for the particle in free space (k when $x < 0$ and $x > z$) and within the barrier (q when $0 < x < a$) respectively.

By requiring the wavefunction ψ to be continuous over all boundaries, at $x = 0$ the wavefunctions on either side and their derivatives must be equal. This creates four relationships (two at each boundary between regions). These may be solved for the ratio $|T/I|$ to find the tunneling probability $P_T = |T/I|^2$ [47]:

$$P_T \equiv \left|\frac{T}{I}\right|^2 = \frac{1}{(\frac{k^2+q^2}{2kq})^2 \sinh^2 qz + 1}. \tag{2.6}$$

For the regime where $qz \gg 1$, the tunneling probability goes to an exponential relationship with the barrier width z (which in the case of STM would be the tip-sample separation):

$$\begin{aligned} \sinh qz \to \frac{1}{2}(e^{qz} - e^{-qz}) \to \lim_{qz \gg 1} \frac{1}{2} e^{-qz}, \\ P_T \simeq (\frac{4kq}{k^2+q^2})^2 e^{-2qz}. \end{aligned} \tag{2.7}$$

If the barrier in question is a smooth function which may be approximated by a Riemann sum, this approximation may be used to estimate the tunneling probability through an arbitrary barrier [47, 45]:

$$P_T \propto \exp(-2\sum_i q_i \Delta z) \approx \exp(-2\int dz \sqrt{\frac{2m}{\hbar^2}(U(z) - E)}). \tag{2.8}$$

This exponential relationship is often cited as a back-of-the-envelope calculation technique to estimate tunneling currents. It is an excellent approximation for calculating field emission currents from a metal, however perturbation theory offers a better model for the STM tip-sample tunneling current. Loosely following Bardeen [48], the following derivation considers tip-sample van der Waals forces and tip-sample tunneling by applying first order time dependent perturbation theory to Fermi's golden rule.

Fermi's golden rule uses first order perturbation theory to calculate a formula for the rate of a particle jumping from an initial state $|i^0\rangle$ to a final state $|f^0\rangle$ at time t in a periodic

perturbation of the form $H_1 = e^{-i\omega t}$. The transition rate between these states is [16]:

$$R_{i\to f} = \frac{2\pi}{\hbar} |\langle f^0| H_1 |i^0\rangle|^2 \delta(E_{fi} - \hbar\omega). \tag{2.9}$$

This is dependent on the difference in energy between the two states, $E_{fi} = \hbar\omega_{fi} = E_f^0 - E_i^0$, and ω, the perturbation frequency. For tip to sample tunneling, $\langle f^0| H_1 |i^0\rangle$ is most referred to as the tip-sample wavefunction overlap tunneling matrix element M_{ts} [45]. It is a calculation of the overlap between the tip and sample wavefunctions as a result of the perturbation H_1.

The tunneling current becomes an integral over this tunneling rate multiplied by the electron occupation of the tip and of the sample. In turn, the occupation is a function of the density of states (DOS) of the tip or sample, $\rho_{t,s}$, and the Fermi function $f(E)$, offset by the bias voltage. This formulation considers a tunneling current where the tip electrons ($f_t(E - eV)$) tunnel into unoccupied states in the sample ($1 - f_s(E)$). For the full current, both tunneling from the tip to the sample and from the sample to the tip need to be summed:

$$\begin{aligned} &I_{t\to s} - I_{s\to t} = \\ &-\frac{2\pi e}{\hbar} \int_{E_F}^{E_F+eV} |M_{ts}|^2 \rho_t(E - eV)\rho_s(E)[f_s(E) - f_t(E - eV)]dE. \end{aligned} \tag{2.10}$$

By inspection, for a constant tip DOS, the current is proportional to the DOS of the sample.

To continue, the tunneling matrix element must be considered in more detail. Bardeen [48] showed that for larger tip-sample separations, it is reasonable to approximate the system as having zero potential between the tip and sample, and separate systems with a tip potential U_T and a sample potential U_S that sum for the potential of the entire system $U_T + U_S = U$. Under these assumptions, the wavefunction of an electron within this barrier is the primary calculation needed to predict the tunneling current. Bardeen's approximations allow partial integration of the given current equation so that the final equation is a surface integral:

$$M_{ts} = \frac{\hbar^2}{2m} \int_S (\psi_s \nabla\psi_t^* - \psi_t^* \nabla\psi_s) \cdot dS \tag{2.11}$$

The last significant piece of Bardeen's calculation of the STM tunneling current is to consider the tip and sample wavefunctions. These functions are required to use Eq. 2.11

to calculate the current. STM tips are selected to be metal with well defined terminating wavefunctions. As mentioned previously, tungsten and PtIr tips are common tips as they may both be modeled using a spherical s-orbital wavefunction which allows the tip DOS to be considered nearly constant. For most cases it is entirely reasonable to consider the tunneling current from a sample to be proportional to the DOS of the sample [45].

Scanning tunneling spectroscopy (STS) is a technique which takes advantage of the previous derivation to measure the local density of states (LDOS) of a sample. STS experimentally measures a derivative of Eq. 2.10. Theory finds this derivative by treating the bias (eV) as a perturbation [49]:

$$\frac{d\ln|I|}{dV} = -\frac{e\kappa z}{2\Phi_s} + \frac{\rho_S(eV)|M(eV)|^2}{|\int_0^{eV}\rho_S(\epsilon)|M(\epsilon)|^2 d\epsilon|}. \tag{2.12}$$

Here, z is the tip-sample distance, κ is the electron decay length $\sqrt{2m|E|/\hbar}$, and Φ_S is the work function of the sample. For a constant tunneling matrix component, the derivative is proportional to the LDOS of a sample.

Finally, the lateral resolution of STM can resolve atoms. An upper limit for the lateral resolution of a given STM tip, Δx, is related to the tip radius R_T and distance from the surface z [46].

$$\Delta x = \sqrt{2(R_T + z)}\ \text{Å} \tag{2.13}$$

For a typical tip radius of ~ 10 nm and tip-sample distance $z = 1$ nm, $\Delta x \approx 1.5$ nm. Many STM images clearly resolve the graphene honeycomb, and features less than 1 Å have also been resolved, so clearly this is very approximate [46].

2.4.2 STM Characterization of Graphene

Graphene is a rather ideal material for STM studies. Graphite has long been the material of choice for STM calibration because a clean, atomically flat surface may be prepared very simply, and the bond length between carbon atoms is very stable. The graphite lattice constant is often used to calibrate STM x-y distances, particularly in extreme temperature regimes where the piezo transducers exhibit hysteresis [45]. Graphene, possessed of

very similar properties, may be viewed just as easily, as long as adsorbed surface water is removed either through heating or electron bombardment.

Graphene fabrication was first confirmed when exfoliated graphite was transferred to SiO_2 [50]. SiO_2 is a notoriously poor substrate for STM research; STM inherently requires a conductive substrate and even when covered by a conductive coating SiO_2 often exhibits charge pooling and rough topography. Added to this difficulty, graphene transfer techniques have so far utilized either resist or polymer coatings which still leave residue behind despite extensive cleaning techniques [9]. Often the most successful cleaning techniques damage the graphene as well. This combines to make exfoliated graphene very difficult to characterize with STM. Epitaxial and vacuum techniques are essential to fabricate graphene samples which are clean and flat enough for STM analysis. This thesis concentrates on STM studies of graphene grown epitaxially on silicon carbide.

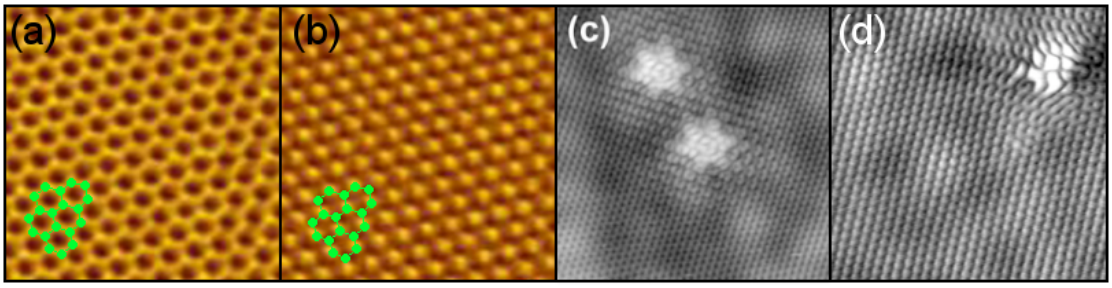

Figure 2.6: STM of (a) uncoupled and (b) coupled graphene, illustrating the shift in intensity between the two graphene sublattices. The carbon honeycomb lattice is highlighted in green in the bottom left corner for both images. 4.5 nm side for both (a) and (b). (c) Two point rotational defects in graphene, creating a distinctive six-point star scattering pattern with ringing (continued scattering) visible in the surrounding area as a continued disturbance in the graphene honeycomb pattern. 9 nm side, 1.0 V, 0.1 nA. (d) A defect in Si-face SiC graphene with inter-valley scattering visible as horse-shoe shaped ringing emanating around the bright area in the top right. 9 nm side, 0.15 V, 0.5 nA at 6 K [51]. Adapted from [52, 53, 51].

There are many things which have been shown to affect the relative intensity of carbon atoms in atomically resolved graphene STM images. For instance, graphene which is Bernal stacked appears in STM images with a hexagonal lattice: the intensity of one

graphene sublattice is much greater than the other. This effect is due to interlayer coupling modifying the charge density in bilayer or multilayer Bernal stacked graphene. Bernal stacking breaks the sublattice symmetry: one sublattice is located directly above subsequent layers, while the other sublattice sits in the middle of a honeycomb hexagon (recall Fig. 1.1). This is visible on graphite, where the top layers may be uncoupled from the substrate [52] and is illustrated by comparing Fig. 2.6(a) and (b) which illustrate STM images of a pristine honeycomb lattice next to a Bernal stacked coupled lattice.

Sources of electron scattering are very visible in STM images of graphene. These scattering patterns have characteristic traits dependent on their origin [54, 53, 51]. A pattern typically has a distinctive shape immediately at a scattering defect, but the effect is visible for many angstroms around the defect; this modulation of the intensity of the lattice immediately surrounding a defect is termed 'ringing' in the following. For instance, a defect induced scattering pattern may be seen in the top right portion of Fig. 2.6(d). This is a sample of bilayer graphene on Si-face 4H SiC and the repeated horseshoe-like pattern is attributed to inter-valley scattering [51]. The 2D fourier transform of a pattern like the horseshoe ringing can give insight into the particular scattering induced [54]. Fig. 2.6(c) shows two point rotational defects which induce scattering in the image of a six-pointed star. Similar to Fig. 2.6(d), the star in (c) is surrounded by ringing as well. Slip planes induce similar ringing along a visible line instead of at one point [53].

Scattering patterns are not only visible from defects within a pristine graphene lattice. Foreign elements in the lattice can induce similarly characteristic patterns as well. Nitrogen has been shown to create a trimer pattern, also with ringing, when it is a graphitic substitutional dopant in graphene. Fig. 2.7 illustrates STM of a pristine graphene lattice side by side with a lattice with visible scattering from graphitic substitutional nitrogen. Nitrogen can take several other lattice positions as well; two of the most common bonding arrangements are known as pyridinic and pyrrolic nitrogen, illustrated in Fig. 4.2. The change in intensity between a carbon atom and a nitrogen is due to charge transfer from the nitrogen to the carbon in the graphene lattice. For graphitic nitrogen, although the nitrogen occupies exactly the same lattice position as a carbon atom, the increased electron density from the

nitrogen atom with one more electron than carbon is very visible [55]. Graphitic, pyridinic, and pyrrolic nitrogen as imaged in STM are considered in more detail in Chapter 4.

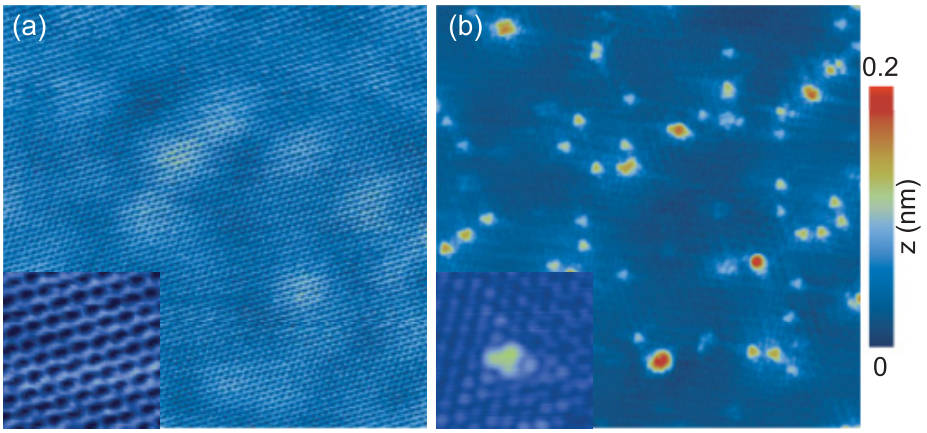

Figure 2.7: Comparison of STM on (a) pristine graphene and (b) graphene with graphitic substitutional nitrogen. Adapted from [55].

2.4.3 STS Characterization of Graphene

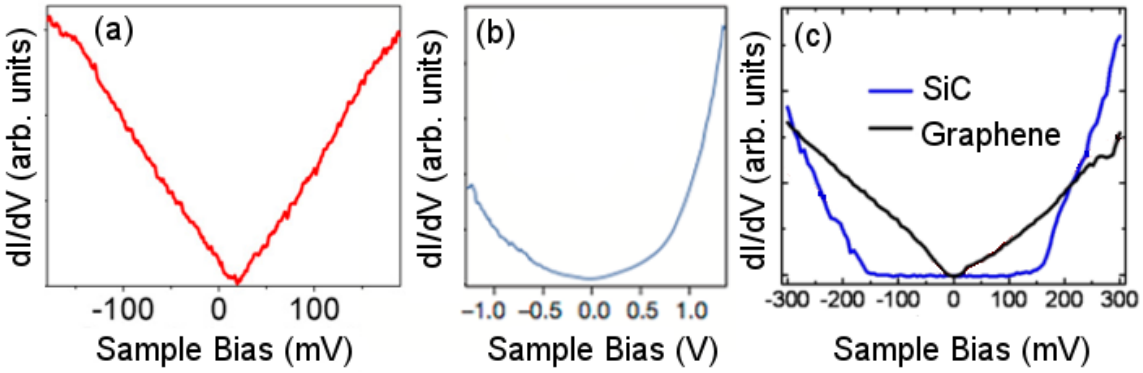

Figure 2.8: (a) STS of monolayer graphene; a decoupled layer on graphite [52]. (b) STS of Si-face SiC graphene [56]. (c) STS of Si-face SiC (gapped, blue) and monolayer graphene (linear 'V', black) [46]. Adapted from [52, 56, 46].

The cleanest scanning tunneling spectroscopy (STS) spectra possible of graphene may be collected from samples of graphite where some top layers are rotated with respect to the

bulk and thereby uncoupled; see Fig. 2.8(a) [52]. Such layers may be recognized through their pristine honeycomb pattern in STM images (as coupled layers will show moiré structures or the hexagonal lattice shown in Fig. 2.6).

On silicon carbide however, graphene STS spectra have more of a 'bowl' shape as may be seen in Fig. 2.8(b). Layers which are strongly bonded to the SiC show more metallic or flat dispersion (Fig. 2.8(c)), whereas completely uncoupled layers revert to the more linear dispersion (compare Fig. 2.8(a) and (c)).

An applied magnetic field will induce square-root law Landau levels in graphene, which is shown at 4 T in Fig. 2.9. Interlayer coupling will also influence the shape of STS with Landau levels. STS spectra of coupled layers will be less symmetric in intensity for both the function envelope and individual peaks as shown in Fig. 2.9(b). Landau levels are also visible when induced by pseudo-magnetic fields; these levels are typically broader in STS than those induced by an applied magnetic field.

There are several intrinsic features which create the shape seen in a Landau level spectrum taken via STS. Landau level peaks intrinsically increase in width with increasing energy responding to a finite quasiparticle lifetime [52]. Taking this into account along with square root spacing and equal degeneracy (Landau peaks of the same integrated area), the background envelope of a Landau level spectrum rises sharply. Landau peaks inherently decrease in height with respect to the background as the peaks rise in index [52].

All published STS measurements of Landau levels in graphene to this date have been taken at liquid nitrogen temperatures at least, and a number at 7-5 K [57–59, 14, 60–62, 52]. However, there is experimental data showing visible Landau level transitions via far infrared transmission at room temperature [63]. This has been considered indicative that graphene Landau levels could be used in magnetic devices at room temperature.

STM and STS are valuable techniques which allow precise local measurement of a graphene sample's LDOS and atomic quality. As the qualities of a graphene sample are greatly influenced by the local lattice structure of a graphene sample, STM enables extremely fine characterization.

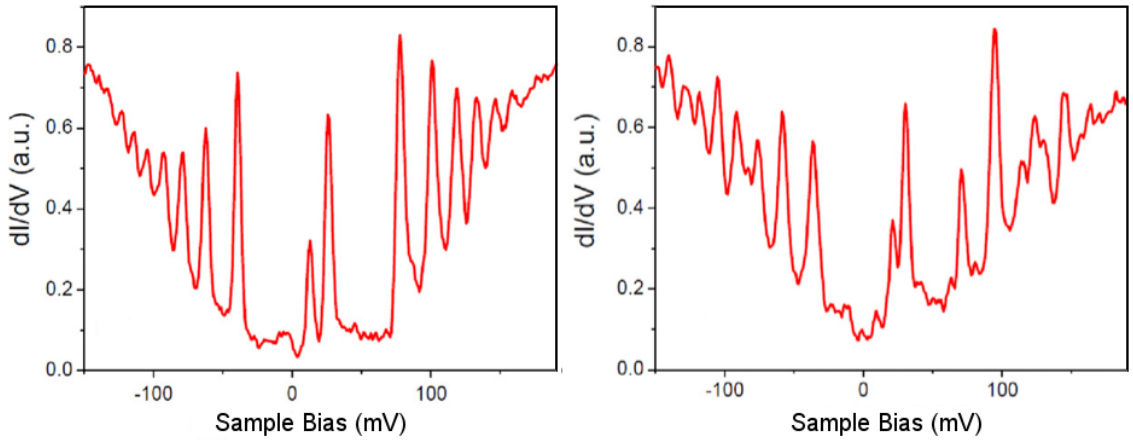

Figure 2.9: STS spectra showing Landau levels on (a) uncoupled and (b) coupled graphene. Applied field is 4 T. Adapted from [52].

2.5 X-ray Photoelectron Spectroscopy

X-ray photoelectron spectroscopy (XPS) may be used to analyze the bonding and proportion of elements in a sample. XPS is based on analyzing electrons ejected from a sample by incident X-rays (photons). The technique is optimized to analyze ejected core electrons in particular, although some Auger electrons are also visible in the same energy range. These ejected core electrons enable the identification of individual elements in the sample, including an analysis of the general proportion of elements present overall to precision of ~ 0.1 atomic %. XPS is typically used for thin films because the technique only penetrates one inelastic mean free path into the analyzed sample, typically a thickness of < 10 nm or even much less [64]. Fig. 2.10 gives a schematic representation of the ejection of a core electron and a typical XPS spectrum.

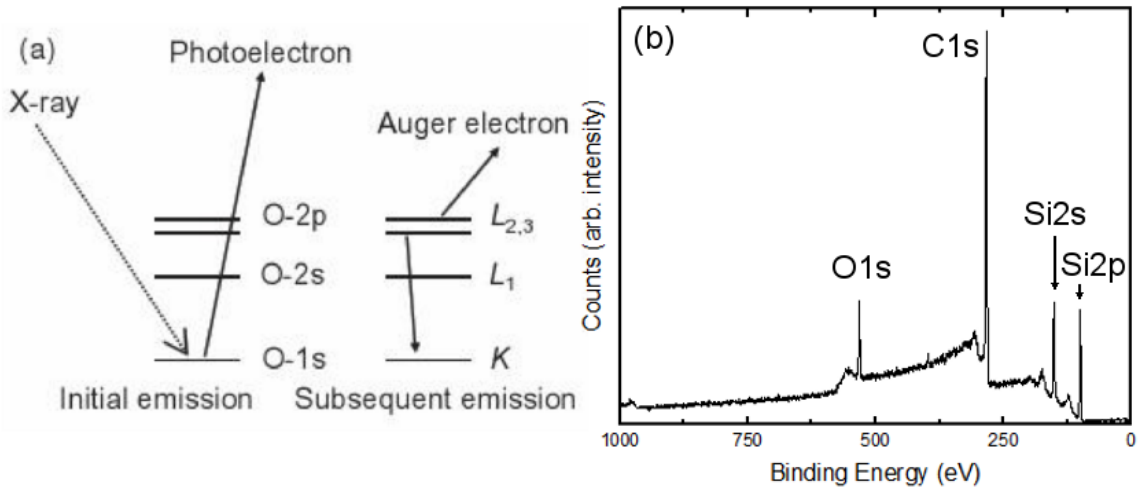

Figure 2.10: (a) Core electrons ejected by an incident photon. Adapted from [64]. (b) An example of an XPS spectrum of graphene grown on C-face SiC.

The value of interest for an XPS spectrum is the energy of the original core state of the sample, E_{core}. This can be calculated from the ejected electron's energy. The kinetic energy of the electron, KE_{XPS}, is known to be related to the instrument's work function, Φ_{XPS}, and the incident X-ray energy, E_{photon} as follows [64]:

$$E_{core} = E_{photon} - \Phi_{XPS} - KE_{XPS}. \tag{2.14}$$

The instrument and the sample are presumed to be in conductive contact, so it is commonly assumed that the work function Φ in Eq. 2.14 is of both instrument and sample.

The sensitivity of an XPS spectrum to bonding configuration allows the separation of different bond species within the same element. The C1s peak is the primary carbon peak, and for SiC graphene, the carbon bound in SiC sp^3 bonds and the sp^2 bonded graphene carbon create distinct peak components. The different polar faces of SiC also create distinct components; the interface layer on Si-face SiC graphene adds a satellite peak at higher binding energy which disappears as more graphene is grown on the Si-face. The evolution of the C1s peak components as graphene grows from nonexistent to 4 layers or more thick is illustrated in Fig. 2.11.

The C1s and Si2p peak can be used in tandem to measure graphene thickness for SiC graphene samples. The two components of the C1s peak may be decomposed to find the relative proportion of graphene-bound carbon and SiC carbon. As a graphene sample grows thicker on the surface, it screens or attenuates the Si2p peak. As it is known that in the bulk silicon and carbon atoms should be of equal proportion in SiC, this attenuation of the Si2p can be used to check the fit of the SiC carbon portion of the C1s peak (as the attenuation to the SiC carbon should be the same as the silicon). The thickness can then be found by fitting the attenuation of the SiC carbon peak and the proportion of the graphene carbon simultaneously [65–67].

Since the electron mean free path changes with energy, XPS may probe different depths of a thin film dependent on the incident X-ray energy. This is known as variable energy XPS, and can give significant information on the depth distribution of bonding configurations.

XPS is used to calculate the thickness of SiC graphene samples in Chapter 3 and 5. Chapter 4 presents a more in-depth analysis of the N1s peak in NG graphene supported by variable energy XPS.

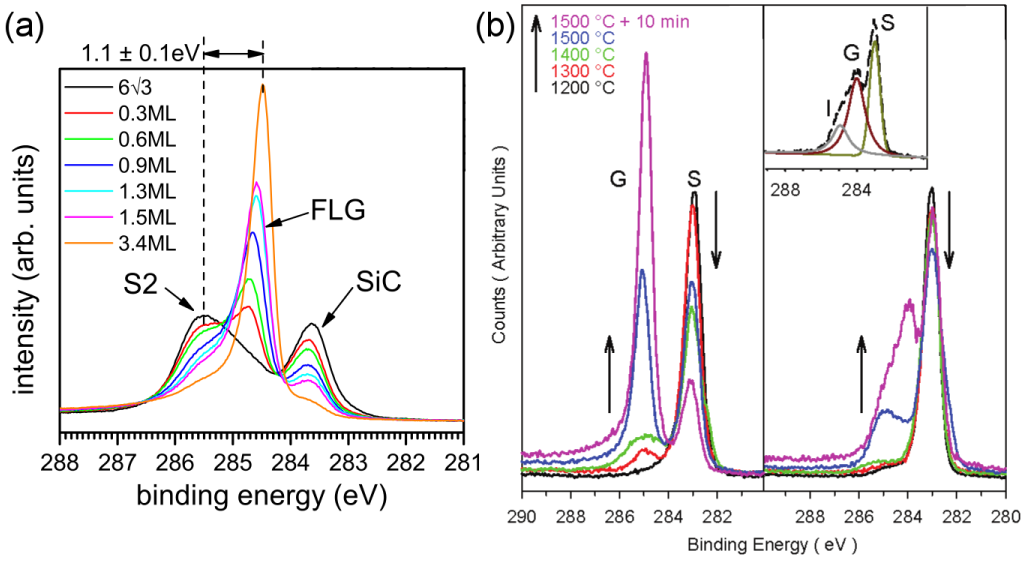

Figure 2.11: High resolution XPS of the C1s peak as graphene is grown at different temperatures and to different thicknesses. (a) Si-face 4H SiC graphene at various ML thicknesses and (b) C-face 4H SiC graphene grown at progressively higher temperatures, 1200-1500 °C. The peak components attributed to the graphene (∼285 eV; G or FLG) and SiC (∼283 eV; S or SiC) are indicated. Note the extra component visible for the Si-face graphene (S2) which is attributed to the interface layer. Adapted from [66, 67].

Chapter 3

Epitaxial Graphene

Graphene was first viewed experimentally by transferring exfoliated flakes from highly ordered pyrolytic graphite (HOPG) to a substrate on which it was visible and able to be handled [50]. However, such transfer processing and subsequent handling essentially assures that all exfoliated graphene will have residues from some process or another still present on the sample. This makes it difficult to pin down the dopant level of the graphene, how strained it might be, and the effects of impurities [9]. Mechanical exfoliation also tends to produce small flakes of graphene, much smaller than a wafer of any size making large batch processing of exfoliated graphene devices still a future fantasy rather than a present reality.

Thin film growth directly on an insulating substrate is the ideal alternative, potentially allowing for wafer or large sized single crystal graphene. Epitaxy is the growth of a thin film in registry with the crystal face of the substrate below; oriented overgrowth will be used for a thin film growth without registry and independent of the substrate crystal face. Direct thin film growth produces clean, wafer sized samples of graphene which are easily processed into devices with existing integrated circuit procedures. Direct growth on metals, such as CVD growth on copper foil, has been shown to be viable [68], however the metal must be removed before graphene devices may be patterned. Direct grown on an insulating substrate is clearly a simpler source for graphene intended for devices. Among the possible

insulating substrate materials, graphene growth has been reported experimentally on SiC, sapphire, and mica [69, 39, 70]. This thesis will discuss the experimental set up and results of growing graphene on sapphire by the thermal decomposition of acetylene in vacuum (GOS), and also presents a review of epitaxial graphene grown on SiC grown by controlled silicon sublimation (CSS).

3.1 Graphene on Sapphire

Sapphire offers many potential benefits as a graphene substrate. The lattice structure of on-axis C-plane sapphire is hexagonal with a lattice constant approximately twice that of graphene (sapphire: 4.75 Å and graphene: 2.46 Å), which lends hope that ordered epitaxial growth might be possible. Sapphire is also highly stable. Sapphire undergoes a reconstruction above $1200°$C, but is stable down to room temperature after reconstruction [71]. This substrate stability allows for graphene growth at high temperatures, which can correspond to higher graphene film quality. As an insulating material, graphene circuits may be printed directly on a sapphire substrate without the need for exfoliation or transfer. Sapphire wafers are also significantly cheaper than SiC single crystal wafers currently.

3.1.1 Experimental Methods

Graphene on sapphire (GOS) is grown by the thermal decomposition of acetylene gas. Acetylene pressures between 0.1-20 Torr are investigated in the following. Single crystal on-axis sapphire wafers were purchased from University Wafer and diced into 1x7 mm samples. The sapphire substrates are then heated in high vacuum (base pressure $1*10^{-8}$ Torr) by resistive heating of tantalum foil. Earlier samples were heated by sandwiching two pieces of sapphire with tantalum foil in-between, providing physical as well as radiative heat transfer. Later samples enclose a sapphire sample in a boat of tantalum foil. A foil boat provides more uniform heating, however does not allow the surface to be monitored with reflection high-energy electron diffraction (RHEED). Temperature measurements are

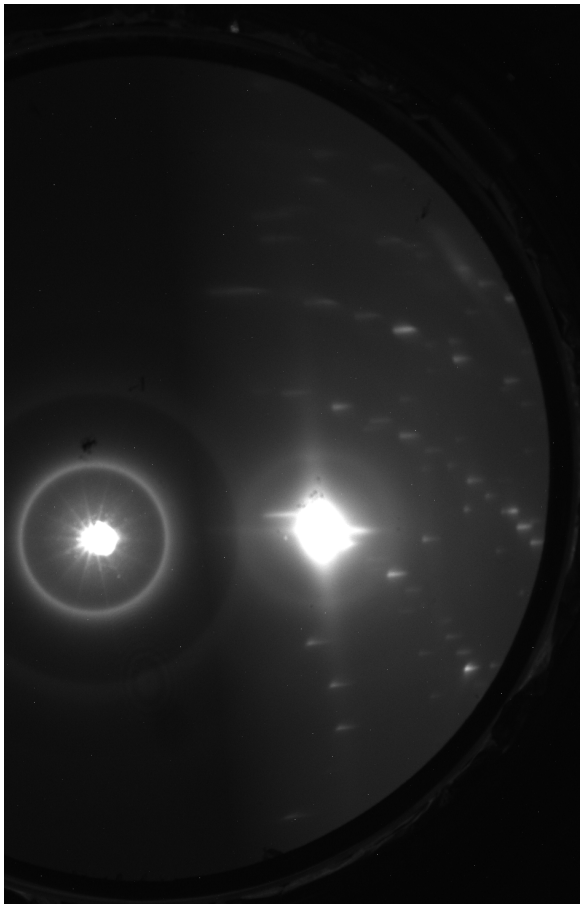

Figure 3.1: RHEED image of reconstructed sapphire surface after flashing to >1250°C.

taken via pyrometer with an emissivity set to 0.3. Temperature trends were confirmed to within ± 100°C by comparison with a thermocouple held in contact with the sapphire surface.

At high temperatures, the surface of single crystal sapphire achieves a stable $\sqrt{31} \times \sqrt{31}$ surface reconstruction due to oxygen leaving the top few layers of the wafer. The temperatures found to produce high quality GOS films are certainly above this threshold temperature. This reconstruction has been studied in detail; the transformation is achieved in good vacuum above 1250°C and is stable at least up to 1700°C [71]. The reconstruction was confirmed to be the result of desorbing oxygen from the sapphire surface, since the original sapphire surface structure may be recovered by annealing in the presence of oxygen. The highest quality GOS films are grown at substrate temperatures between 1350-1450°C, thus

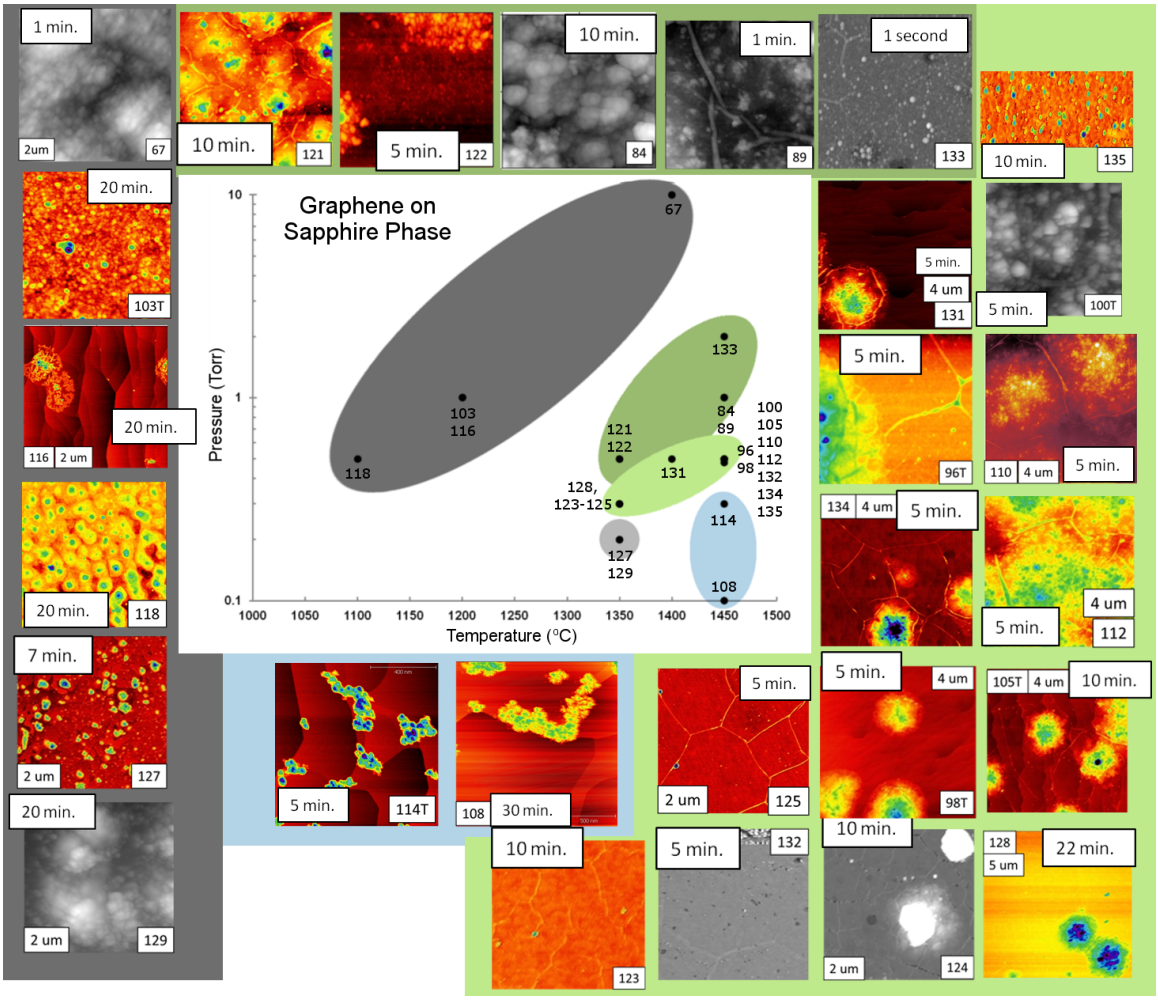

Figure 3.2: Pressure (log(Torr)) vs. Temperature (°C) of GOS samples. Regions of consistent morphology are indicated by color and correspond to color-coded AFM images. Light blue indicates growth on steps, but no film coverage. Light green indicates some of the best single or few layer graphene samples. Several light green samples also show amorphous carbon hills as well. Darker green indicates thicker multilayer GOS. Dark and light gray indicate amorphous graphitic films which no longer have the characteristics of turbostratic graphene.

to achieve a stable surface for epitaxial growth all sapphire substrates are flashed to achieve reconstruction prior to growth. Fig. 3.1 shows an example of the RHEED pattern visible after reconstruction.

GOS samples are initially flashed to > 1500°C 3-4 times to achieve a stable and clear

RHEED pattern of the $\sqrt{31} \times \sqrt{31}$ sapphire surface. Acetylene gas (Toll Gas & Welding Supply, 99.996% pure) is admitted to the vacuum chamber, raising the pressure to between 0.10-20 Torr. After a stable pressure is achieved, the sample temperature is raised to a growth temperature, typically $\sim$1450°C, and held for between 1 second to 20 minutes in the acetylene atmosphere. The best single layer GOS samples were grown for between 5-10 min. at 300-500 mTorr and 1350-1450°C as may be seen in Fig. 3.2. The sample temperature is maintained for a predetermined growth time, after which the acetylene gas is pumped out. The growth temperature is held stable until the base pressure reaches $5*10^{-7}$ Torr, at which point the temperature is decreased and the sample is allowed to cool to room temperature.

3.1.2 Characterization and Discussion

Turbostratic is used in the following sections to describe a material composed of stacked layers with rotational disorder. Turbostratic graphite appears as graphite to all characterization techniques, except for greater inter-layer separation than ordered graphite and completely randomized rotations between all layers [15]. Ordered graphite, like HOPG, is Bernal stacked. Turbostratic graphene is used in the following section to describe few layer graphene which maintains some of the characteristics of graphene and yet has significant rotational disorder and larger inter-layer stacking. Turbostratic graphene may be distinguished from turbostratic graphite by considering the Raman 2D peak: graphite has a 2D peak with two-components which is lower in intensity than the G peak [37, 15]. Graphene's 2D peak is a single Lorentzian (for monolayer or decoupled multilayer) and the 2D peak intensity can be twice that of the G peak [34]. GOS samples fall on the continuum between turbostratic graphene and graphite; macroscopically thick samples of GOS are turbostratic graphite, but thinner GOS samples have many of the defining characteristics of graphene. Raman spectroscopy is used heavily in the following to determine if a sample is more characteristically turbostratic graphene or verging on turbostratic graphite.

GOS films ranging from monolayer to multilayer are imaged via AFM in Fig. 3.3. The

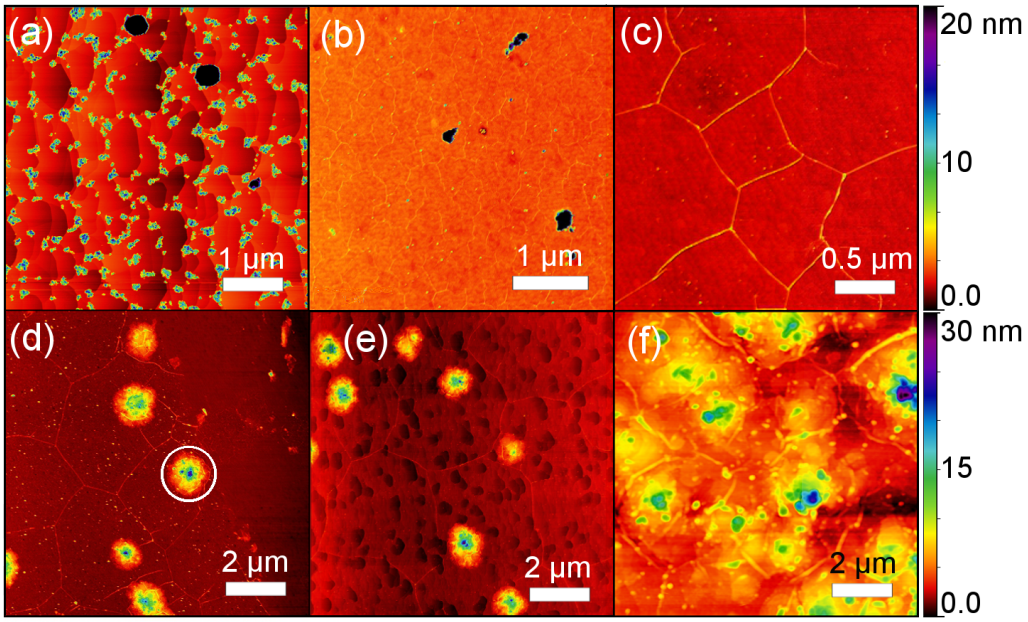

Figure 3.3: AFM images of several different morphologies of GOS samples. (a) Nucleation on sapphire step edges. (b)-(e) Monolayer or few layer graphene, primarily identified by visible sapphire steps under the graphene, and sharp folds with hexagonal character; confirmed with AFM or profilometer step measurement (see Fig. 3.4). (e) This film is the same sample shown in (d) after an anneal at 1500°C. Pits (darker areas) in the underlying sapphire have opened up, but graphene folds may be still seen traveling continuously across the pits. (f) Thick turbostratic graphene verging on graphite. Note in (d)-(e) hills of amorphous carbon or carbon flowers are visible: the white circle in (d) highlights a hill. These hills are a feature in many films. As GOS films grow thicker, these hills become more abundant until they merge to form films hundreds of nanometers thick as illustrated in (f). The height scale is the same for all, 0-20 nm from dark red through the rainbow to violet black.

growth pressure and temperature dependence of the morphology displayed in Fig. 3.3 are displayed in Fig. 3.2. GOS appears to nucleate at step edges on the sapphire surface; films which were arrested in the growth process before uniform coverage was achieved show bunched areas of material at these step edges (see Fig. 3.3(a)). The thinnest monolayer GOS films have thin, long pleats $\sim$2 nm high and 0.5-5 μm long. These pleats are visible in Fig. 3.3(b)-(e). Sapphire steps are still visible beneath these thin GOS films as well (see Fig. 3.3(c)). The white circle in Fig. 3.3(d) highlights an amorphous carbon hill or carbon

flower. These hills are a common feature in all GOS films. As GOS films thicken, these hills multiply in quantity until they overlap and eventually merge to form the entire visible film. Fig. 3.3(f) is an example of a macroscopically thick GOS film wherein hills have merged; prominent pleats are visible in Fig. 3.3(f) which may serve to identify the edges of the merged hills.

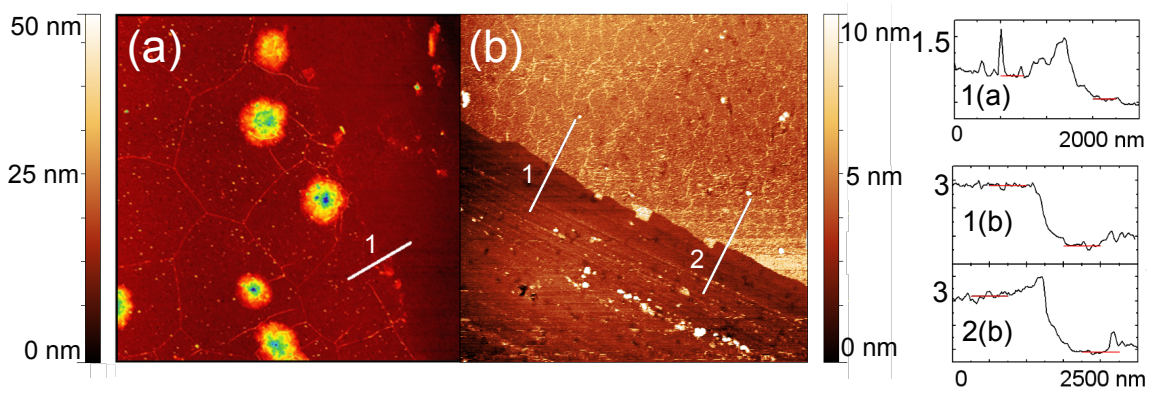

Figure 3.4: AFM images measuring the step height for two GOS samples. (a) Monolayer GOS, taken from Fig. 3.3(d). (b) Multilayer GOS. Step profiles are illustrated to the right; the step in (a) is ∼0.35 nm, or monolayer in height, the steps in (b) are ∼2.2 nm in height, or 7-8 layer graphene.

Monolayer graphene GOS samples are identified by measuring monolayer graphene thickness via AFM while simultaneously considering the Raman spectrum for the sample. Monolayer graphene films will display a single-component 2D peak of equal or greater intensity to the G peak. Multilayer GOS deemed turbostratic graphene is identified by a multilayer thickness measurement by AFM and a Raman 2D peak which is still single-component. A 2:1 intensity ratio of 2D to G peaks (I(2D)/I(G)) is typically reported for monolayer exfoliated graphene, however turbostratic graphene is recognized to have a lower I(2D)/I(G) ratio than exfoliated Bernal stacked graphene. A blue shift to the 2D peak is also reported as typical [72, 73]. Fig. 3.4 illustrates an AFM measurement for both mono- and multilayer GOS.

Fig. 3.5 shows the Raman spectrum of monolayer GOS compared to multilayer GOS and CVD grown graphene transferred to SiO_2. The blue shift to the 2D peak of turbostratic graphene may be seen in Fig. 3.6 which compares 2D peaks of monolayer and multilayer

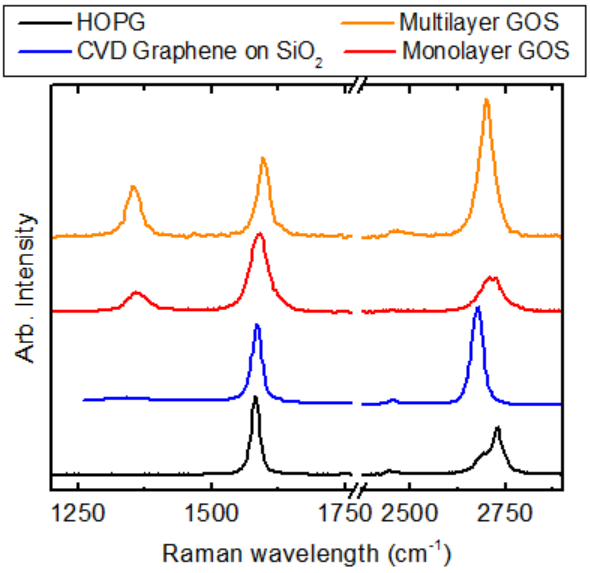

Figure 3.5: Comparison of the Raman spectrum for HOPG (bottom, black), CVD grown graphene transferred to SiO_2 (third from top, blue), single layer GOS (second from top, red), and multilayer GOS (top, orange). Spectra offset for clarity.

GOS. Just as with exfoliated graphene, the highest quality GOS films are characterized by narrow, tall 2D peaks, however at most a 1.25:1 ratio is more typical for the I(2D)/I(G) of GOS.

The 2D peak for single layer graphene may be fitted with a single Lorentzian peak [72, 35] (as discussed in Chapter 2). For multilayer films with Bernal stacking, related satellite peaks around the 2D peak are introduced by the interaction of phonon modes between layers [72], thus multilayer Bernal stacked graphene requires multiple Lorentz peaks for an adequate representation. The increased interlayer spacing and rotational disorder present in turbostratic graphene leads to much less interlayer phonon interaction thus the 2D peak of multilayer turbostratic material may still be fit by a single Lorentzian albeit broadened with respect to monolayer films [72]. This is illustrated in Fig. 3.6 which uses a single Lorentzian peak fit for the 2D peak of multilayer GOS.

Fig. 3.7 shows how GOS film quality is highly dependent on growth temperature. Higher temperature yields Raman spectra more indicative of graphene. At growth tem-

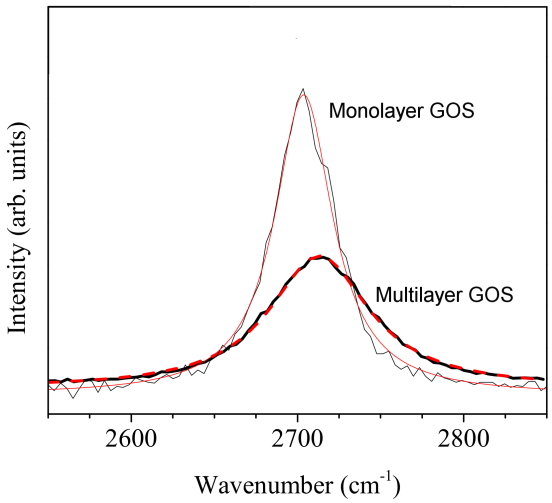

Figure 3.6: Comparison of the 2D peak for single and multilayer GOS. Single layer graphene (taller thinner peak, thin black) and multilayer graphene (thicker shorter peak, thick black). The Lorentz fit to each peak is also illustrated (red).

peratures below 1300°C Raman spectra show the films to be essentially amorphous carbon with little to no graphitic content: the 2D peak is not present, the G peak is broad, and the D peak is intense and broad as well. This trend is illustrated abstractly in Fig. 3.2 where the growth temperature and pressures which create amorphous films are highlighted in grey and the growth temperatures which result in thin turbostratic graphene films are in light green. Schumann [39] has presented MBE growth of graphene on sapphire with similar Raman spectra, however this graphene is of worse quality primarily due to the lower growth temperatures used.

Fig. 3.7 also illustrates how the width of the 2D peak decreases with increasing growth temperature as well. While many thicknesses (and hence film qualities) may be grown at each of the illustrated temperatures, to grow a film with the thinnest 2D peaks, higher temperatures are clearly required. Just as a 2D peak with higher intensity than the G peak points to a film with more graphene-like characteristics than graphitic, a narrow 2D peak points to high-quality graphene as well.

As discussed in Chapter 2, Raman peaks may also be used to gain knowledge of the

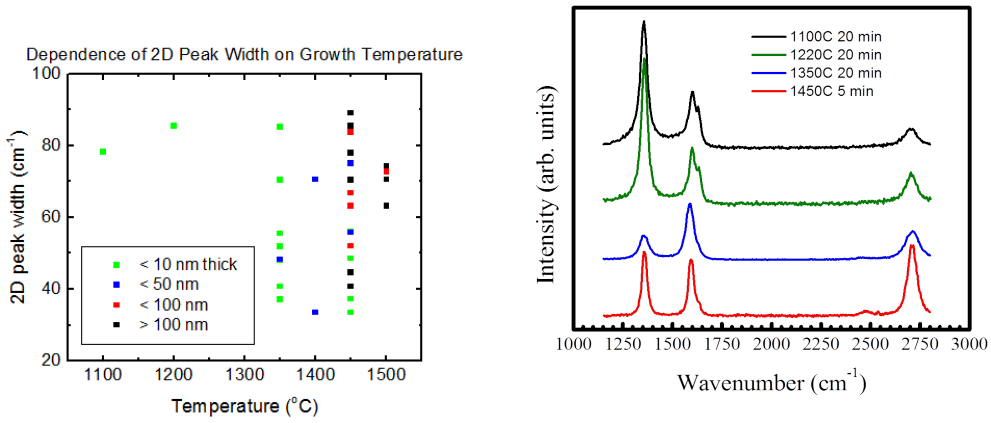

Figure 3.7: (a) Scatter of 2D peak width vs. growth temperature. (b) Raman spectra comparing GOS grown at equal acetylene pressure but differing temperatures. The improvement of the 2D peak as the temperature increases is evident. Spectra offset for clarity.

crystalline domain size of a film. The relative intensity or width of the G, D and 2D peaks may each give estimates of the domain size. Using Raman peaks to analyze the crystalline domain size for GOS, domain size clearly grows in size for thinner samples grown at high temperature than multilayer samples. However, I(D)/I(G) for GOS implies domains between 20-200 nm, which is significantly smaller than all the flat area visible in AFM between pleats. The I(D)/I(D') ratio is also $\sim$1, which does not correspond to the approximation expected if domain boundaries are the primary defect in GOS; the ratio should be $\sim$3.5 if domain boundaries were the primary defect. Thus, domain boundaries do not seem to be the only type of defect in GOS films and the crystalline domain measured by I(D)/I(G) is likely underestimating the true domain size.

If a single domain is assumed to be one area completely bounded by pleats such as those visible in AFM then GOS films have domains which are closer to 0.2-12 μm^2 in size, or 250-2000 nm in diameter. Furthermore, as visible in Fig. 3.3(c) folds with 60° rotations between are not uncommon. A 60° rotation would exactly mimic the rotational symmetry of the graphene lattice, thus the lattice could easily flow smoothly over these folds in particular, allowing crystalline domains to be even larger than the area bounded by pleats.

Transmission electron microscopy (TEM) of GOS films shows GOS samples to be rotationally disordered, as may be seen in Fig. 3.8. For Bernal stacked graphene, two overlaid hexagonal diffraction patterns would be expected. Rotational disorder is a characteristic of turbostratic graphene or graphite instead [15, 72].

GOS TEM samples are fabricated by mechanically exfoliating GOS samples to a piece of tape and transferring the exfoliated graphene to a piece of water-soluble polyvinyl alcohol (polymer; PVA) substrate. The PVA with graphene is inverted above a copper TEM grid in a water bath and left to sit until the water has evaporated entirely. Flakes of GOS were visible in the TEM hanging off of the copper grid bars. The single area diffraction image in Fig. 3.8 is taken from a thinner flake, although from the even intensity of the rotated rings the flake is estimated to be at least $\sim$30 nm thick.

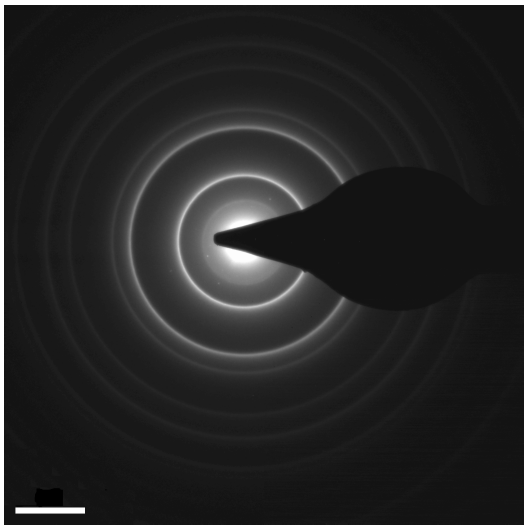

Figure 3.8: Single area diffraction image taken via TEM of GOS. The scale bar is 5 nm^{-1}

Fig. 3.9 shows the X-ray diffraction (XRD) peak corresponding to the interlayer spacing of graphite and graphene [74]. Cu K-α radiation was used with a spot size of 1 μm^2. For Bernal stacked graphene or graphite, the interlayer spacing would be 3.35 Å, corresponding to a peak at 26.6°, whereas turbostratic spacing at 3.44 Å would be at 25.9°. Fig. 3.9 illustrates these peak positions and it is clearly visible that GOS has turbostratic interlayer spacing [15].

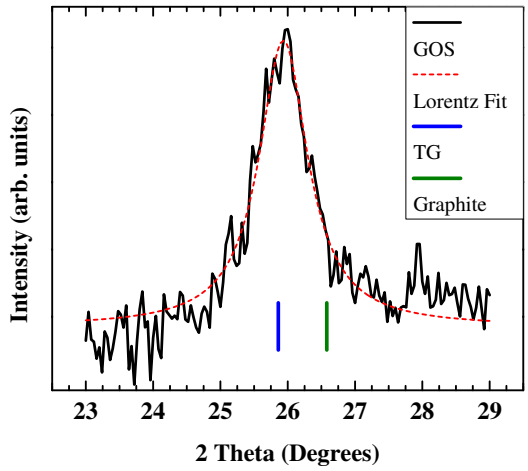

Figure 3.9: X-ray diffraction of GOS. The interlayer spacing for turbostratic graphite or graphene at 25.9° (left, blue) and Bernal stacked graphite at 26.6° (right, green) are notated on the x-axis.

3.1.3 Conclusion

In conclusion, high quality turbostratic graphene may be easily grown on sapphire through the thermal decomposition of acetylene. GOS is turbostratic because the inter-layer spacing of samples is clearly greater than that of graphite or Bernal stacked graphene, and Raman spectra of samples shows a single-component peak even for multilayer samples. The best thin GOS films are turbostratic graphene because AFM measurement confirms the films are mono- to few-layer in thickness and Raman spectra show a narrow single-component 2D peak of greater intensity than the G peak. Higher growth temperatures (up to 1550° investigated here) have been shown to directly increase film quality, with no higher limit set in the experiments presented. A certain pressure of acetylene seems required to start nucleation, however once nucleation is achieved film growth appears to proceed rapidly. TEM and XRD also confirm that GOS films are turbostratic with disordered rotations between layers and interlayer stacking greater than graphite. This turbostratic stacking suggests that GOS is made up of isolated graphene layers with the corresponding excellent electronic qualities of monolayer graphene. Thus, GOS is a potential fabrication method for device quality graphene grown directly on an insulating substrate.

3.2 Graphene on SiC

Epitaxial graphene on silicon carbide (SiC) has been characterized more extensively than any other epitaxial graphene to date. SiC offers a simple, reliable substrate for graphene growth, and is commercially available as high quality single crystal wafers.

An understanding of the bare substrate is the first place to start when studying graphene grown on SiC. SiC is a transparent crystal with hundreds of possible polytypes resulting from different crystal stacking orders. 6H and 4H are the hexagonal polytypes most commonly used for graphene growth. 4H SiC is used for the nitrogen-seeded SiC graphene samples studied in Chapter 5 and is illustrated in Fig. 3.10. 4H SiC is possessed of two polar faces known as the silicon face (Si-face; (0001)) and the carbon face (C-face; $(000\bar{1})$), illustrated in the unit cell in Fig. 3.10. These faces are named for the atoms which terminate the surface, assuming no reconstruction. While silicon and carbon are in equal numbers in bulk SiC, the crystal structure creates two single element planes slightly offset from each other allowing a termination composed wholly of either silicon or carbon dangling bonds. Graphene growth is significantly different between the Si-face and C-face. The graphene grown on nitrogen-seeded SiC (NG) characterized in Chapter 5 are all grown on the C-face, thus the growth characteristics of pristine C-face graphene are considered in more detail here, however some of the most significant differences between Si- and C-face growth are commented upon.

Graphene is grown on SiC by heating a SiC substrate to high temperatures which causes the silicon, which has a higher vapor pressure than carbon, to sublimate. The SiC surface becomes carbon rich as the silicon leaves and graphene is formed as it is a low energy state for carbon under certain pressure and temperature regimes. Each layer of graphene is formed at the SiC surface and further layers form below already-coalesced graphene and push the first layer out further (although it is the SiC which is receding). Approximately three bilayers of SiC (3/4 of the unit cell for 4H SiC; see Fig. 3.10) are consumed to form one layer of graphene [39]. Graphene growth can begin at $\sim 1200°$C in UHV, however the most uniform films are grown at greater pressures. At UHV pressures, the silicon leaves

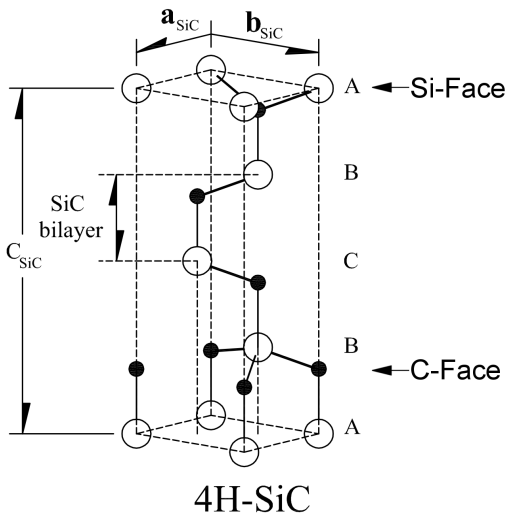

Figure 3.10: Crystal lattice of 4H SiC. This polytype is composed of four SiC bilayers. Silicon and carbon face planes are indicated. Adapted from [75].

too quickly, creating graphene which is patchy, pitted, and non-uniform. An atmospheric overpressure of Argon is often used to prevent the silicon from leaving too quickly. W. A. de Heer et al. have pioneered the technique of controlled silicon sublimation (CSS) whereby a SiC substrate is enclosed in a tiny (< 1 cm) graphite crucible with a small hole (< 1 mm) [76, 77]. This enclosure causes the sublimating silicon to build up a higher local silicon partial pressure around the sample, preventing silicon from abandoning the surface too quickly, and slowing the graphene growth process.

Surface preparation can be a significant factor in film quality for SiC graphene as well. Heating in the presence of atomic hydrogen will etch away many microns from the SiC substrate, eradicating scratches still present after polishing. A clean hydrogen etched SiC surface exhibits regular steps, typically $\sim$1 nm high, equivalent to one 4H SiC unit cell height. The step spacing is sensitive to the absolute cut angle and so is often variable [46, 75]. These broad terraces are visible in Fig. 3.11, as graphene grown on SiC conforms to the SiC steps. The samples used in Chapter 5 are miscut $\theta_c < \pm 0.25^\circ$, corresponding to terrace widths of $(0.75)/(\tan\theta_c)$ = 172 nm or greater.

Uniform graphene growth on the C-face is more difficult to achieve than on the Si-face.

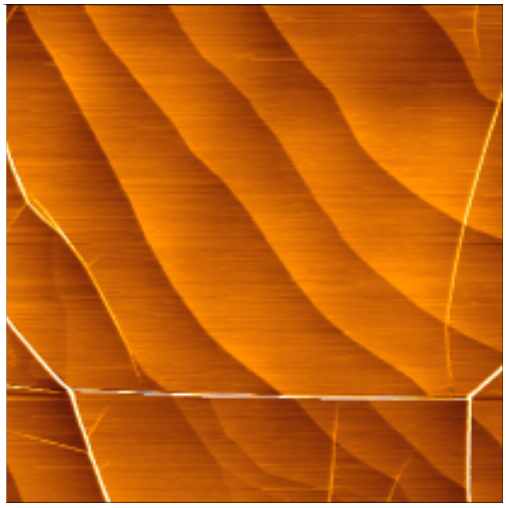

Figure 3.11: AFM of 10-12 layer pristine CSS C-face SiC graphene. 9 μm on a side. The white lines are graphene folds; the steps in color stretching from the top left to bottom right are SiC steps. Taken from [75].

Growth on the C-face is quicker than the Si-face, thus most of the difficulty is in preventing too much silicon evaporation [76, 77]. C-face growth appears to be nucleated by defect sites [78] rather than step-edge growth characterized on the Si-face [79]. Si-face graphene can be self-limiting at few layers at certain temperatures [80, 81]; in contrast C-face graphene grows much thicker films with many rotations and stacking defects [46]. However, C-face graphene typically has larger mobility and longer mean free paths than Si-face graphene [46]. A high quality, uniform C-face CSS SiC graphene sample is shown in Fig. 3.11. This AFM image clearly shows large areas (>5 μm^2) of CSS C-face graphene free of pleats or topography, with the graphene conforming cleanly to the underlying SiC steps. There are several reviews and studies which summarize the experimental parameters which lead to similarly uniform and defect free C-face graphene [39, 69, 76].

The initial graphene layer for C-face graphene, called the zeroth layer here, shows graphene-like bands in ARPES and no covalent bonding components in XPS [66]. This zeroth layer is still under study as there is some indication that it is carbon rich and possibly buckled. The C-face does not achieve a long-range reconstruction underneath the zeroth

layer; a 2×2 reconstruction is sometimes visible in low-energy electron diffraction (LEED), but probing the long range interface order implies that the surface is never fully ordered and is likely in different stages of graphitization [82].

A key feature of C-face SiC graphene is the rotational stacking. As discussed previously, Bernal stacked graphene has strong interlayer bonding which causes the linear dispersion of monolayer graphene to disappear for multilayer samples. On the C-face, however, graphene grows rotationally disordered. There is some preference for rotations at $\sim 58^\circ$ or $\sim 62^\circ$ and 30° with respect to the underlying layer, but the ordering mechanism is not fully understood [83]. Precise angles aside, the key result is that C-face graphene layers do not have significant interlayer bonds and thus even multilayer C-face graphene samples maintain a linear dispersion as well as excellent electron mobility and mean free path lengths [84]. Note that these rotations occur as a graphene layer forms beneath a top layer of graphene and the SiC substrate.

There is some charge transfer to C-face graphene from dangling bonds, measured to be up to 0.2 eV. This corresponds to a shift in the Fermi energy for single-layer graphene; as a SiC graphene sample grows thicker the graphene's Fermi energy returns to the Dirac point. ARPES measurements find that the dangling carbon bonds on the C-face locate their unassigned charge mostly within the plane of the substrate. The Si-face has even greater charge transfer, up to 0.44 eV, because the dangling silicon bonds on the Si-face donate much more charge outward, away from the substrate and into the graphene [85, 66].

During graphene growth the SiC steps are known to bunch and change height and frequency; indeed the whole surface changes as it is consumed in the graphene creation process. However, after growth the graphene on step edges is typically thicker than the graphene on the flat areas and may be strained differently or even have a different charge density [39]. Graphene growth can be limited to be solely on step edges, and these ribbons have been shown to create p-n junctions from this charge density difference between step edge graphene and terrace graphene. The ribbons have also shown to have exemplary electronic characteristics [56].

In conclusion, SiC graphene offers a simple, well controlled route to graphene growth.

NG, characterized in Chapter 5, takes advantage of this previously published knowledge concerning C-face SiC graphene in an attempt to tease apart the effects of nitrogen upon the entire system.

3.3 Thermal Strain in Epitaxial Graphene

The difference in the coefficient of thermal expansion (CTE) between graphene and its growth substrate can lead to strain which may relax into folds in the final graphene film after cooling. To calculate the global strain induced in this way, the CTE for graphene is necessary. In general the coefficient is reported to be negative, from $(-8.0 \pm 0.7) \cdot 10^{-6}$ K^{-1} for single layer graphene at room temperature [86], go through a negative to positive transitions between $350 - 900$ K, and rise to $2 - 4 \cdot 10^{-6}$ K^{-1} [86, 87]. Fig. 3.12 illustrates the conflicting literature, comparing several experimentally measured and theoretically calculated CTE functions for graphene. Fig. 3.13 illustrates the linear approximation used for the calculation detailed below, which attempts to incorporate the behavior of graphene's CTE in the different regimes.

The CTE calculates a change in size through integration:

$$\frac{\Delta L}{L} = \int_{T_i}^{T_f} \alpha \, dT \tag{3.1}$$

The lattice constant after the change in temperature becomes $L_{new} = L + \Delta L = L(1 + \frac{\Delta L}{L})$. This can be used to calculate the percent of lattice mismatch after a change in temperature between two materials. Percent lattice mismatch is calculated here with respect to the graphene lattice because the substrate is assumed to maintain a more stable lattice constant, thereby requiring the graphene lattice to take up all the thermal strain.

$$\begin{aligned} \frac{L_g - L_{sub}}{L_g} &\rightarrow \frac{(L_g + \Delta L_g) - (L_{sub} + \Delta L_{sub})}{L_g + \Delta L_g} \\ &= \frac{L_g(1 + \int_{T_i}^{T_f} \alpha_g dT) - L_{sub}(1 + \int_{T_i}^{T_f} \alpha_{sub} dT)}{L_g(1 + \int_{T_i}^{T_f} \alpha_g dT)} \end{aligned} \tag{3.2}$$

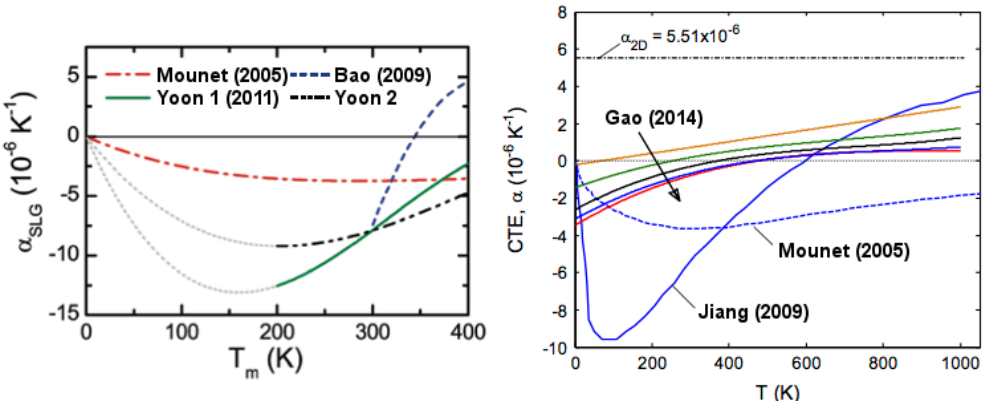

Figure 3.12: Comparison of experimentally measured and theoretically calculated coefficient of thermal expansion for single layer graphene. (a) CTE experimentally fit from Raman G peak shifts (solid green and dash dot black, Yoon et al. [86]), and measured from a sagging suspended membrane (dashed navy, Bao et al. [88]). (b) CTE theoretically calculated via DFT calculations (dash dot red and dotted blue, Mounet and Marzari [89]), molecular dynamic simulations (multicolored series, Gao and Huang [87]), and non-equilibrium Green's function (solid blue, Jiang et al. [90]). Adapted from [86, 87].

Sapphire has a uniformly positive CTE, from $\sim 5.9 * 10^{-6}$ K^{-1} at room temperature to $\sim 9 * 10^{-6}$ K^{-1} at $\sim$1550°C, illustrated in Fig. 3.13 [91]. The sapphire planar (hexagonal) unit cell is 2.97 Å, compared to graphene's 2.46 Å lattice constant.

For silicon carbide, the CTE is well defined from 0-1000°C, after which the CTE is approximated as remaining constant at the value for T =1000°C, $5.2 * 10^{-6}$ K^{-1}. This is not unreasonable as direct measurements of the lattice constant up to 2000°C show that the lattice slows in expansion above 1000°C.

For the approximation for graphene's CTE, there is some consensus that graphene's CTE at room temperature is negative, and has a value around $-8 * 10^{-6}$/°C. There is much more controversy concerning the temperature at which graphene's CTE crosses zero. It is approximated here to cross zero at 300°C (600 K) which is supported by both experimental and theoretical calculations [90, 86]. There are few reports of graphene's CTE over 700°C (1000 K); several directly contradict the value at high temperature giving between $2\text{-}5 * 10^{-6}$, mostly from theoretical predictions [90, 87]. For this calculation, the CTE for

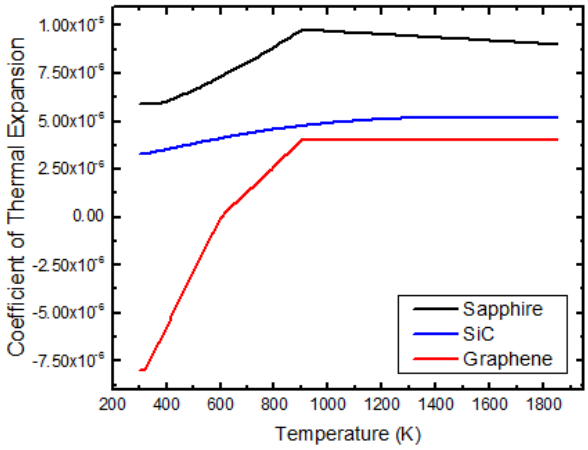

Figure 3.13: Coefficient of thermal expansion for graphene (bottom, red), sapphire (top, black), and 4H SiC (middle, blue).

graphene above 1000 K is taken to be 4*10^{-6} K^{-1} as shown in Fig. 3.13.

A Riemann sum was used to estimate the integral for each ΔL with a ΔT of 10°K. Fig. 3.14 compares how the graphene lattice parameter shrinks against the sapphire and SiC lattices. The sapphire lattice parameter (in-plane hexagonal lattice constant) goes from 3.01 Å at 1550°C to 2.97 Å at room temperature [91]. Graphene shrinks from 2.47 Å to 2.46 Å at room temperature. If the graphene is assumed to be in perfect registry with the sapphire, this implies 22.0 % strain at growth temperature decreasing to 17.2 % strain at room temperature. If, however, the graphene is allowed to be unstrained at growth temperature and compressed the differential thermal expansion as the sample cools, this implies 1.6 % compressive strain in the graphene film. This is calculated by dividing the change in the substrate lattice constant by the graphene lattice constant at room temperature. The graphene is only required to change size only as much as the substrate shrinks while cooling down in this model.

Fig. 3.14 also displays the lattice parameter change for SiC between growth and room temperature. The in-plane hexagonal 4H SiC lattice parameter starts out at 3.08 Å [75] at room temperature, rising to 3.10 Å at 1550°C. Again, first considering if the graphene is

in perfect registry there is a lattice mismatch creating 25.7-26.0 % strain which decreases to 25.2 % strain at room temperature. Similarly to the sapphire calculation, if the graphene floats unconstrained on SiC at growth temperature and is only compressed as the film cools, 0.9 % strain is expected. This a simplistic view of the SiC-graphene relationship as graphene is known to grow in a variety of rotations which have commensurate structures with the underlying substrate, resulting in strain relaxation within the film [75]. There is still ongoing research to characterize the exact character of the SiC-graphene interface for epitaxial graphene on SiC. Si-face SiC graphene has been experimentally measured to have 0.2 % compressive strain from Raman peak shifts [39].

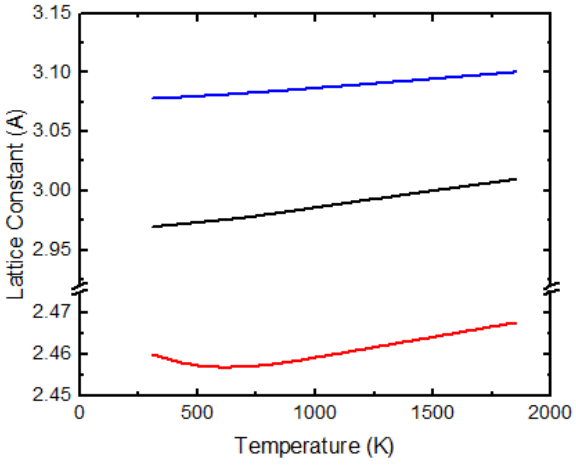

Figure 3.14: Lattice parameter for graphene (bottom, red), 4H SiC (top, blue), and sapphire (middle, black) as they shrink respectively from 1550° growth temperature to room temperature. Note the graphene changes the least overall, leading to compressive strain.

Chapter 4

Nitrogen in Graphene

In silicon, the classic semiconductor, dopants can be absorbed into the bulk by heating in the presence of a dopant source and allowing diffusion to infuse the bulk with alien atoms. Often these dopants take substitutional sites displacing a silicon atom, although dopant effects may be realized from interstitial sites as well [92]. Graphene cannot be doped so simply. Typically graphene doping is achieved through chemical functionalization both by exposure to a substitutional dopant either with plasma or a reactive gas and by adsorbed species. Substitutional dopants increase scattering and disorder [54, 55]. Adsorbates on the surface or charge transfer from the substrate will similarly donate localized charge and offer a non-invasive doping mechanism which maintains the pristine graphene lattice [2]. Adsorbates are notoriously changeable and few are stable at higher temperatures, requiring significant modifications for device fabrication. Substrate doping can be more fixed and will be considered more in depth here.

Nitrogen doping is often considered as a means to induce a bandgap in graphene. Theoretical predictions consistently agree that substitutional nitrogen in the graphene lattice will induce a bandgap. Estimations vary from 0.6-2 % for the nitrogen content that will open a bandgap [93, 3, 5, 2]. It is considered possible that it is not the added charge or potential from the nitrogen which opens a gap, but the sublattice asymmetry which is induced if more nitrogen is located on one sublattice than the other [5].

There have been many experimental reports of nitrogen doped graphene so far; cited references only offer a sampling of theoretical calculations and experimental reports [55, 94–104]. CVD based growth of nitrogen doped graphene is the most popular family of fabrication methods, with some form of nitrogen introduced either as part of the precursor gas, simultaneous with another carbon precursor, or introduced after growth with plasma treatments. Popular CVD carbon and nitrogen sources include ammonia, mixtures of ammonia with methane, hydrogen, and argon, acetonitrile, and pyridine [101]. Another common method to introduce nitrogen is to induce defects in graphene and then treat the graphene with a nitrogen plasma. Yet another method uses a nitrogen-coated boron layer as a substrate [101]. Experimental mobilities for nitrogen doped graphene range from 5-75 cm^2/Vs [102, 103], low, but growing quickly as newer reports are published.

4.1 Experimental Methods for Nitrogen Doped SiC

The introduction to this thesis presented the need for semiconducting graphene; the original goal for the bulk of the experimental work detailed in this thesis was to use nitrogen to open a gap in graphene grown on SiC. Toward that end, nitrogen doping of SiC by implantation was considered. If nitrogen was present near the surface in a SiC substrate, it was theorized that the nitrogen would be included in the graphene lattice during growth. This theory required nitrogen to be introduced in a SiC substrate close to the surface.

Silicon carbide substrates were implanted with nitrogen at various doses between 3-9*10^{16} nitrogen/cm^2 resulting in 0.1-0.5 % atomic percent nitrogen (calculated against the SiC atomic density) at the surface. TRIM, a software which performs Monte Carlo simulations of ion scattering in a crystal, was used to simulate the resting location of the implanted nitrogen. Ion implantation shoots ions into a material at a selected current and energy. Higher energy results in a deeper average resting depth for the implanted species; higher current implies a greater dose or concentration of ions. TRIM takes into account the density and elemental scattering cross section of a crystalline material while calculating the final resting depth of a given concentration of ions shot at a particular energy and current.

A sacrificial SiO_2 cap was grown over the SiC substrates to allow the implantation profile to peak at the interface, thereby maximizing the nitrogen concentration at the surface of the SiC. Fig. 4.1(a) shows a TRIM simulated profile for nitrogen implanted from the left into 70 nm of SiO_2 on SiC. The nitrogen is implanted at 25 keV with a dose of $3*10^{16}$ N/cm^2. This results in a concentration of $\sim 4.8*10^{21}$ N/cm^3, or 0.1 % nitrogen at the interface between the SiO_2 and SiC. The SiC is clearly much more dense than the SiO_2; the profile starts on the left as a very broad peaked implantation profile in the SiO_2 but quickly shoots up in concentration at the interface as many ions are halted upon reaching the SiC. The nitrogen peaks 5 nm below the SiO_2-SiC interface in this example. After etching the oxide cap away, there will be a large peak of substitutional nitrogen in SiC, starting at a concentration of 0.1 % at the surface and rising to 0.13 % at 5 nm.

After the SiC substrates were implanted, visible bubbles could be seen in an optical microscope at the interface between SiC and SiO_2. Fig. 4.1(b) shows an optical image of ~ 5 μm bubbles visible after implantation. The nitrogen apparently segregates into gaseous bubbles rather than staying in the SiC matrix as interstitial dopants. This method of nitrogen introduction was abandoned as a result. The nitrogen bubbles did not create a dopant density of nitrogen within the SiC, even after annealing implanted samples. Subsequent graphene growth was inconsistent, and often plagued by an overabundance of carbon and extreme topography.

After implantation, another method of introducing nitrogen into SiC was considered. SiC may be oxidized by NO gas creating SiO_2 oxide with nitrogen. This technique is primarily used as a trap-passivation method in anticipation of using the SiC-SiO_2 interface for devices; a concentration of nitrogen segregates out of the bulk to passivate interface traps. After etching the oxide cap, about ~ 0.3 monolayers (ML) of nitrogen remains at the interface, strongly bonded to the SiC. From XPS binding energy studies, this is two- and three-coordinated nitrogen in carbon sites, bonding to carbon and silicon atoms at the surface of the SiC [105, 65].

This type of nitrogen-doped substrate did result in viable graphene termed graphene grown on nitrogen-seeded SiC (NG). Subsequent analyses presented in the following and

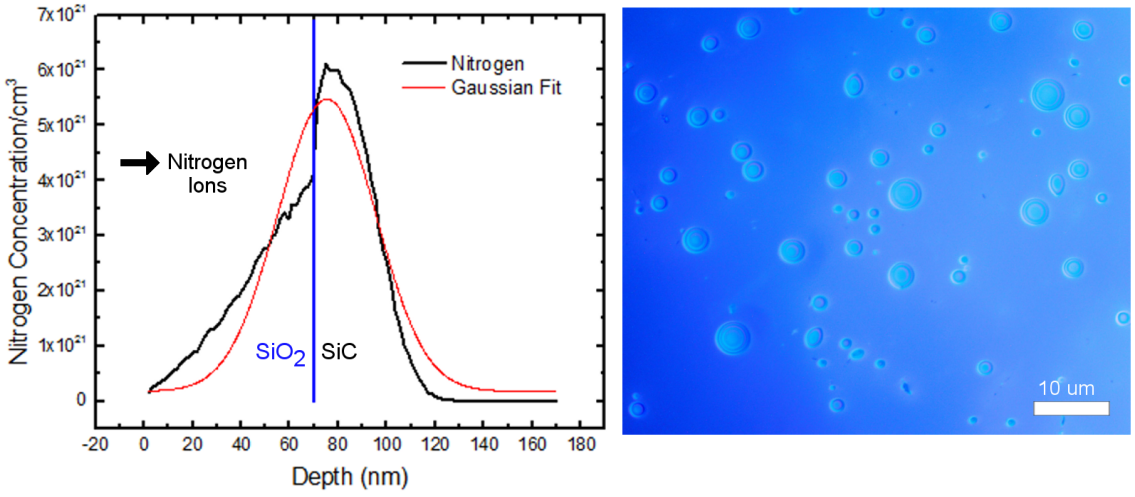

Figure 4.1: Nitrogen implanted SiC. (a) A TRIM calculation of the density of nitrogen vs. depth in SiC with a 70 nm SiO_2 cap. The nitrogen dose is $3.5*10^{19}$ N/cm^2 at 25 keV. (b) Optical microscope image of bubbles of nitrogen present in a SiO_2-SiC sample after implantation.

in Chapter 5 find that the nitrogen is located between the graphene and SiC and does not take substitutional sites in the graphene.

4.2 Characterization Techniques for Nitrogen Doping

In the graphene lattice, nitrogen has several bonding configurations which are known to be stable. Fig. 4.2 illustrates the possible lattice positions for substitutional nitrogen. These include (1) graphitic nitrogen, (2) pyridinic nitrogen, and (3) pyrrolic nitrogen. The bonding configuration present in a nitrogen-doped sample may be identified with many different techniques. For NG graphene, XPS and STM are the primary techniques presented and will be highlighted in the following.

4.2.1 Analyzing Nitrogen in Graphene with XPS

XPS is commonly used to analyze the bonding characteristics of nitrogen-doped graphene; Chapter 2 gives an overview of the general use of XPS for elemental analysis. The N1s

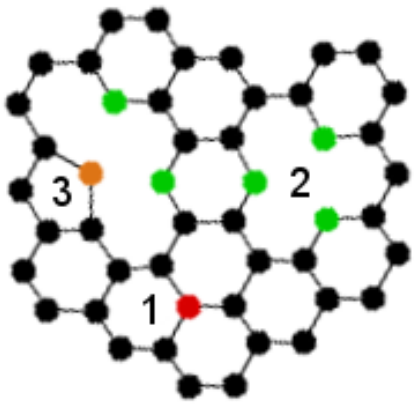

Figure 4.2: Lattice sites for substitutional nitrogen in graphene. (1) Graphitic or quaternary nitrogen, (2) pyridinic nitrogen, or (3) pyrrolic nitrogen.

peak at ∼400 eV in an XPS spectrum splits into multiple peaks corresponding to different nitrogen bonds. The proportion of the different bonds may be found by careful peak fitting of a scan with high energy resolution and comparing the integrated peak intensity of the components. Chapter 2 Fig. 2.11 illustrates how the C1s peak may be used to distinguish between sp^2 bonded carbon in graphene and the sp^3 bonded carbon in SiC.

Experimental reports of the N1s peak in nitrogen doped graphene cite several energy ranges for the different bonding configurations. Pyridinic is reported at between $397.7 - 399.7$ eV, pyrrolic at $399.8 - 401.2$ eV, and graphitic at $401.1 - 402.7$ eV [96, 99, 101]. Nitrogen oxides, including pyridinic bonded nitrogen involved in an oxygen complex, will also induce a peak at ∼402.8 eV [101]. Intercalated nitrogen would similarly be expected to have another distinct peak energy.

The nitrogen concentration in NG is calculated by comparing the nitrogen peak intensity to the silicon 2p peak. As SiC has a known density of silicon, with an established value for the mean free path, this comparison should give accurate concentration of nitrogen. The nitrogen coverage is thus: $n_{Si}\lambda * (I_N\sigma_{Si})/(I_{Si}\sigma_N)$ where I_N and I_{Si} are the N1s and Si 2p peak intensities from XPS and $\sigma_{Si,N}$ are the photoionization cross sections for Si and N respectively. The atomic density of silicon in SiC is $n_{Si} = 4.8 * 10^{22}$ cm^{-3} and the electron mean free path used for SiC is $\lambda = 2.2$ nm for incident X-ray radiation at 1486 eV.

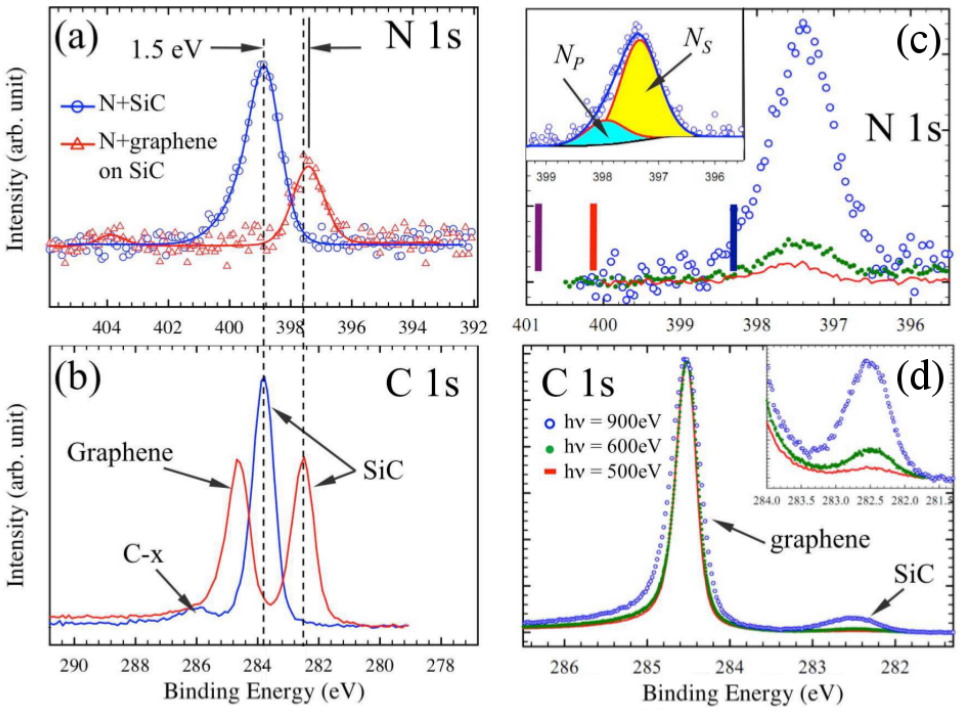

Figure 4.3: (a) N1s and (b) C1s XPS peaks ($\hbar\omega = 1486$ eV) from C-face SiC before (blue) and after (red) growth of 3 layer NG. The nitrogen coverage is 0.3 ML before growth and 0.2 ML after. A 1.3 eV shift after graphene forms is shown (dashed line). The C-x peak at 286 eV is from adventitious carbon contamination in the initial surface. (c) N1s and (d) C1s XPS peaks for 8 layer NG using photon energies of 500 (red), 600 (green solid circles), and 900 eV (blue circles). The intensities have been normalized to the graphene C1s peak. Insert in (c) shows the two component fit to the N1s peak. The purple, red, and blue bars (left to right respectively) in (c) mark the expected peak positions of pyrrolic, graphitic, and pyridinic nitrogen in the graphene lattice. Insert in (d) shows the SiC portion of the C1s peak. Adapted from [65].

Variable energy XPS enables depth profiling of the elemental concentrations of a sample. The incident X-ray energy determines the electron mean free path of the ejected core electrons. Electrons with less energy, an electron ejected by a lower energy X-ray, have a shorter mean free path. Thus, low energy X-rays probe a thinner depth in the same sample. Fig. 4.3 illustrates how the N1s peak decreases as the X-ray energy is decreased, showing clearly that the nitrogen is located below the graphene in NG.

Fig. 4.3(a) and (b) show the C1s and N1s for a 3 layer NG sample. The scans in Fig. 4.3(a) and (b) are taken at the greatest X-ray energy, $\hbar\omega = 1486$ eV, and thus probe the greatest thickness of NG. Fig. 4.3(c) and (d) show the C1s and N1s peaks as the incident X-ray energy is varied. Fig. 4.3(c) shows that for thinner depths, there is significantly less nitrogen in NG. This can be compared to the intensity decrease of the SiC component of the C1s peak, illustrated in Fig. 4.3(d). The nitrogen and SiC-carbon contents visibly disappear as the X-ray energy decreases. Conversely (as expected) the C1s peak component for graphene in Fig. 4.3(d) remains at a constant intensity, as the top is expected to be entirely graphene.

Aside from the absolute atomic percent of nitrogen, the N1s peak components specify the bonding sites of the nitrogen in NG. The N1s peak components show that all of the nitrogen visible in Fig. 4.3 is either bonded to the top layer of SiC or the interface between the SiC and graphene. These two peak components are highlighted in the inset to Fig. 4.3(c) wherein the N_S component is identified as nitrogen bonded to SiC in a carbon site bonded to silicon [106, 107] and the N_P component is identified as nitrogen in sp^3 bonds between the carbon in graphene and the carbon in SiC. The blue, red, and purple bars in Fig. 4.3(c) identify the binding energies expected for pyridinic, graphitic and pyrrolic nitrogen in graphene; their respective locations show that the nitrogen in NG does not take any of these substitutional sites in graphene [65]. Intercalated nitrogen between layers of graphene would also have a distinct XPS peak and no peak for intercalated nitrogen is seen in NG either. In corroboration, nitrogen is not visible in any STM images of NG samples. This will be discussed further in Chapter 5. What nitrogen that is present in NG films either left the surface as the graphene was grown or was trapped by the graphene at the interface.

4.2.2 Analyzing Nitrogen in Graphene with STM and STS

Chapters 5 will present STM and STS of graphene grown on nitrogen-seeded SiC. The STM and STS of NG do not show any direct indication of nitrogen. It is difficult to confirm the absence of nitrogen without a thorough understanding of what nitrogen typically looks

like with STM and STS, so this section reviews the current reported features of nitrogen in graphene.

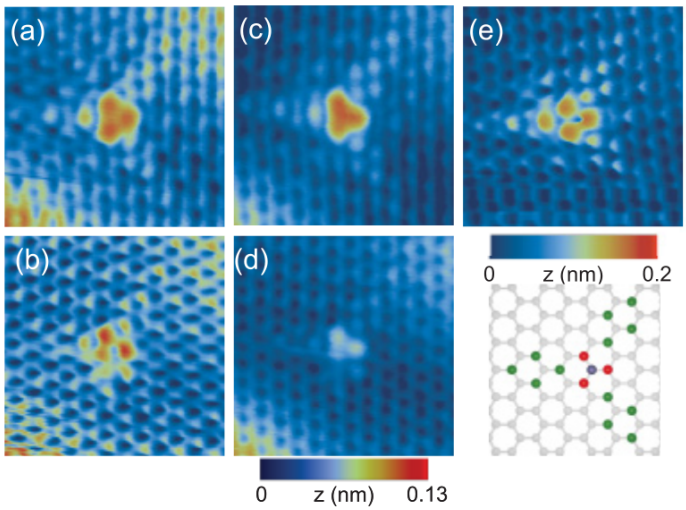

Figure 4.4: STM of a graphitic nitrogen atom in graphene at several different sample biases. (a) 0.2 V, 0.2 nA, (b) -0.2 V, 0.1 nA, (c) 0.5 V, 0.7 nA, (d) -0.4 V, 0.1 nA, and (e) 0.35 V, 0.8 nA. Below (e) is a schematic of the nitrogen (blue, center) in the graphene lattice. The red (trio around center) and green carbon atoms indicate atoms with greater DOS as suggested by (a)-(e). From [55].

The different bonding configurations of nitrogen in the graphene lattice, illustrated in Fig. 4.2, all create different local charge configurations, often clearly visible in STM images. Joucken et al. [55] show beautiful STM images of nitrogen in graphitic sites in the graphene lattice after exposing C-face 6H SiC graphene to a nitrogen plasma. These graphitic inclusions have a characteristic triangular scattering pattern illustrated in Fig. 4.4. The apparent change in height of the nitrogen atom in the STM image (due to the greater intensity) is a purely electronic effect; DFT calculations confirm that graphitic nitrogen sits within the graphene plane [55]. Distinctive scattering patterns, such as the trimer pattern visible around graphitic nitrogen, are created by energy-dependent standing waves of surface charge in the graphene. A 2D Fourier transform of these patterns can reveal the origin of the scattering: often inter- or intra-valley transfers [54]. This is the exact same procedure mentioned in Chapter 2 when discussing scattering defects imaged in STM.

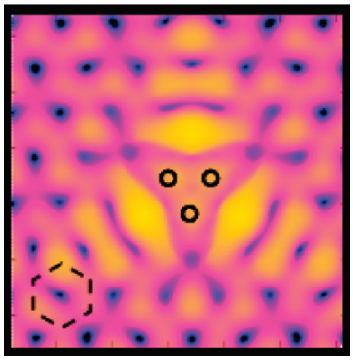

Figure 4.5: Simulated STM of three pyridinic nitrogen atoms in graphene. This image is centered on a lattice identical to the number '2' in Fig. 4.2 where three pyridinic nitrogens, indicated by black circles, create a triangle. From [108].

Pyridinic nitrogen has also been simulated in graphene and similarly displays a triangular pattern, but with more ringing and larger overall size [108] (see Fig. 4.5). DFT calculations can also simulate characteristic patterns from pairs of substitutional nitrogen [109]. All of these patterns show clear, visually arresting symmetries with visible long range ringing, even for single atoms. Substitutional nitrogen in graphene should be clearly visible in STM if atomic resolution can be achieved on a sample.

Since scattering patterns are standing waves of charge, defects and dopants can be associated with particular energy peaks in STS taken at a particular bias [54]. STS of substitutional graphitic nitrogen shows weak states at 0.4 eV and 0.9 eV, asymmetric and mostly a part of the background. Simulated DOS calculations confirm the presence of peaks only at positive bias voltages at $\sim$0.1, $\sim$0.5, and $\sim$1 eV as well [55]. A decrease in intensity is expected both from simulation and experimental STS at negative bias, due to the n-type doping from the nitrogen. Nitrogen primarily creates electronic features in the conduction band, particularly pyridinic configured nitrogen as previously mentioned. DFT calculations imply that most nitrogen pairs should also create states only in the conduction band [109], however experimental STS of identified nitrogen pairs show states in both conduction and valence bands. The states are often broad and asymmetric, although features on the order of the noise are visible as well [109].

Chapter 5

Graphene Grown on Nitrogen-seeded SiC

As stated in the introduction, one of the main thrusts of current graphene research is to reliably fabricate a semiconducting variety of graphene. Several ways to introduce a bandgap in graphene were considered in the introduction, including doping from substitutional atoms and adsorbed species, lithographically etched ribbons, and strain. The following work is the result of a collaboration interested in growing semiconducting nitrogen-doped graphene. The initial attempts at seeding SiC with implanted nitrogen were mentioned in Chapter 4; all samples in the following are grown on nitrogen-seeded substrates after oxidation in NO. Initial experiments show that graphene grown on nitrogen-seeded SiC (NG) does not have substitutional nitrogen in the lattice. Nevertheless, ARPES measures a valence band offset for NG samples. The measured gap was as large as 0.7 eV for 3 layer NG, and was found to depend on layer thickness [65]. Subsequent characterization of NG suggests that the bandgap is induced via strain. The following sections detail the experimental characterization of NG by STM and STS and thereby presents the bulk of the original experimental work presented in this thesis. Landau levels are clearly observed from STS spectra taken on NG, and are subsequently interpreted in terms of strain-induced pseudomagnetic fields. The sequence of observed levels can be fit with a model that includes a

bandgap, consistent with the gap measured via ARPES.

It has been predicted [27, 19, 110] and observed [59, 14] that a distortion or strain of the graphene lattice will create large pseudo-magnetic fields, as derived in Chapter 1. However, no semiconducting graphene has been reported in association with strain induced fields. STS spectra showing several Landau levels induced by pseudo-magnetic fields have been published for spectra taken across graphene nano bubbles [59, 111], graphene on ridges [14, 60], planar strained graphene on copper foil [61], and molecular graphene assembled from CO [112]. Graphene intercalated with potassium was also reported to have Landau levels which were attributed to varying electrostatic potentials rather than strain [58].

Previous publications have characterized the composition of NG films [65, 113]. Chapter 4 details the variable energy XPS analysis which shows that about 0.2 ML of nitrogen remain at the interface between the SiC and graphene, strongly bonded to the SiC substrate after graphene growth. About 25% of these nitrogen atoms bond with the graphene and the SiC in sp^3 bonds, indicating strong bonds between carbon atoms in the first layer of graphene and carbon atoms in the substrate. The nitrogen is not intercalated between graphene layers or substitutionally incorporated in the layers. ARPES measurements on 4 and 8 layer samples showed that the valence band maximum lies 0.3-0.7 eV below the Fermi level, but with broadened spectral intensity attributed to surface roughness [65].

Nitrogenated graphene samples are grown by first seeding C-face 4H SiC $(000\bar{1})$ substrates with nitrogen. SiC wafers are purchased from CREE, and both hydrogen etched samples and chemical-mechanically polished samples have been used as NG substrates. The SiC wafers used were miscut $< \pm 0.25^\circ$, corresponding to terrace widths of $(0.75)/(\tan\theta_c)$ = 172 nm or greater. The SiC sample surface is oxidized in NO as mentioned in Chapter 4 and then etched. This leaves $\sim$0.3 ML of nitrogen strongly bonded to the surface [106]; 0.2 ML remain after graphene growth as shown in the variable energy XPS in Chapter 4 [65]. Graphene is then grown on the nitrogen-seeded substrates via CSS [76, 65, 113]. CSS has been used previously to grow pristine graphene with hundred-micron across rotational domains and record electron mobilities [84, 83, 76].

5.1 STM Characterization of NG

STM and STS studies were primarily conducted at Argonne National Laboratory (ANL) in a UHV variable temperature Omicron STM with an electrochemically etched tungsten tip at room temperature. Reported voltages for STM images are sample biases, and constant current mode was used for all images. STS was taken at ANL after cooling to 100 K. Images were also taken at Oak Ridge National Laboratory (ORNL) at room temperature. STS and images taken at Brookhaven National Laboratory (BNL) were both at 4 K.

As seen in Fig. 5.1 and 5.2, STM on NG films reveals a topography of pleats and plateaus. Several topographic regimes are visible: Plateaus up to 20 nm in diameter appear as atomically flat islands with partial hexagonal features characteristic of graphene. On samples with monolayer graphene, plateaus stand out starkly as flat, bounded areas such as in Fig. 5.1(c). Even on thicker samples the plateaus are flat enough that moiré patterns are sometimes visible such as in Fig. 5.1(d), a common feature on multilayer C-face SiC graphene [76, 75]. Plateaus are typically bounded by smooth pleats at the edges which may roll over onto a subsequent plateau. The white circle in Fig. 5.1(a) highlights two smooth pleats at a plateau edge. Pleats are typically up to $\sim$2 nm high, $\sim$1-4 nm wide, and 2-20 nm long. Rippled regions, such as Fig. 5.1(b) and (e), are sometimes seen separating plateaus or within a plateau, particularly on thicker samples. Fig. 5.1(e) and (f) display atomic resolution over a rippled area and an edge pleat respectively. Despite the irregular surface, atomic resolution can often be achieved on pleats and ripples such as in Fig. 5.1(e) as well as on flat plateaus. Atomic resolution images reveal a defect free lattice flowing smoothly from one plateau to another. Finally some areas have distinctly rougher $\sim$1-5 nm spherical features which are difficult to image due to lower conductivity and low material stability. This spherical debris may be seen in Fig. 5.1(a) along the top edge as a rougher texture on the top plateau and in (b), clinging to the otherwise smooth ripples. Nanocaps are also visible, indicated in Fig. 5.1(a), (c), and (e) by arrows. Nanocaps are not seen on pristine CSS C-face graphene without nitrogen, but have been seen at a lower density in graphene grown on C-face SiC in Argon or UHV [114, 75, 51]. Pleats are commonly seen

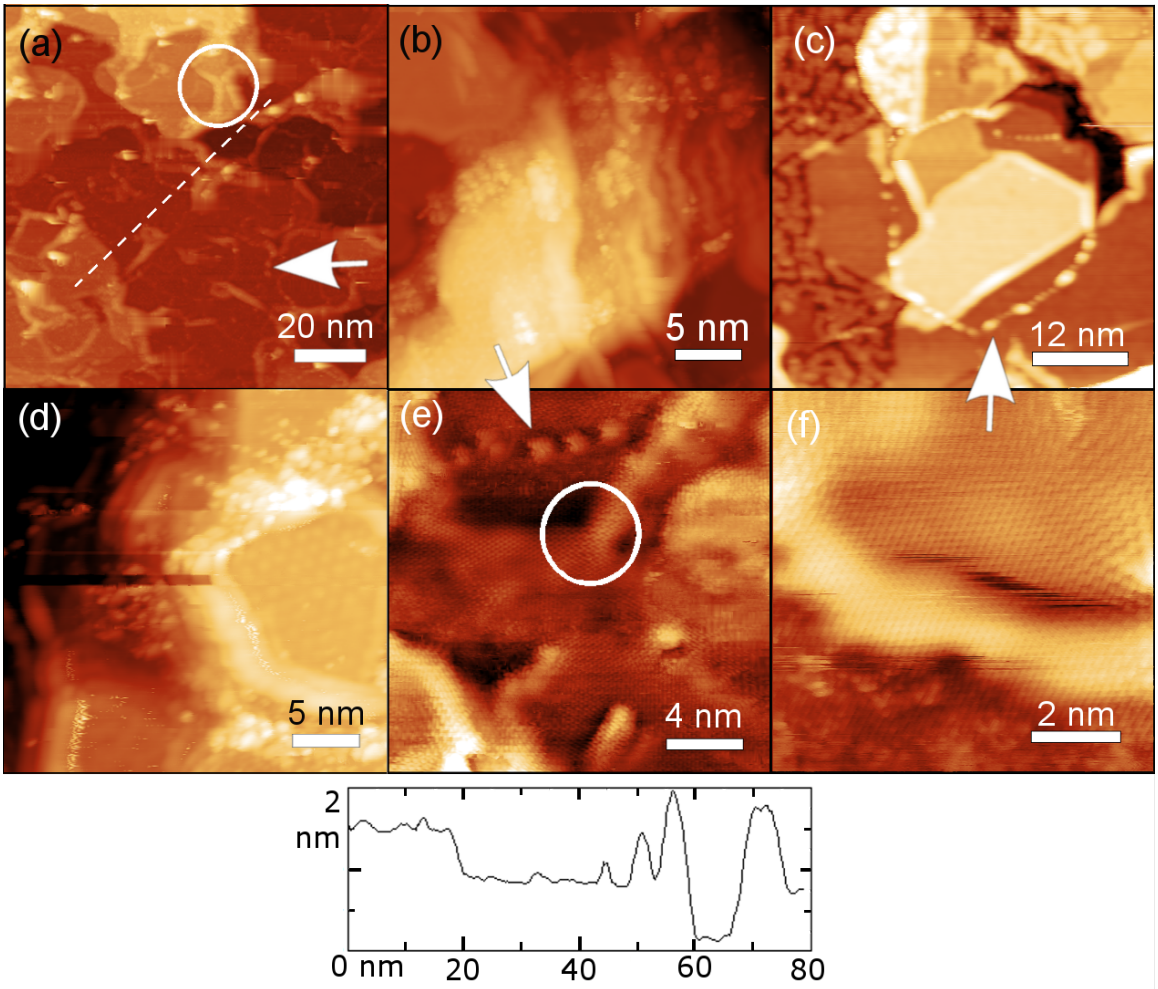

Figure 5.1: Scanning tunneling microscopy of graphene grown on C-face nitrogenated SiC. (a) Overview of 4 layer NG showing plateaus and smooth pleats. 1 V, 0.03 nA. Dashed line shows path of profile plotted below; white circle highlights smooth edge pleats; white arrow indicates nanocaps. (b) Area with smooth continuous ripples between plateaus. 4 layer NG, 0-3 nm height variation, -0.9 V, 0.1 nA. (c) Few layer NG plateaus on bare SiC at left edge. Nanocaps, indicated by the white arrow, are visible surrounding central plateau. 0-2 nm height variation, 4 V, 0.2 nA. (d) A plateau with a moiré pattern. 4 layer NG, 0-1.5 nm height variation, -1 V, 0.2 nA. (e) Atomic resolution of a region with ripples and nanocaps. 3 layer NG, 0-1 nm height variation, 0.1 V, 1 nA. (f) Atomic resolution on the smooth edge ripple of a plateau. 3 layer NG, 0-1 nm height variation, 2.5 V, 0.05 nA. Images taken at ORNL (a), (f), ANL (b), (e), and BNL (c), (d).

STM Image	Image Area with Plateaus	Average Plateau Area	Average Plateau Diameter
Fig. 5.1(a)	25.7 %	61.2 nm^2	8.8 nm
Fig. 5.2(a)	24.7 %	20.7 nm^2	5.1 nm
Fig. 5.2(b)	37.0 %	111.0 nm^2	11.9 nm
Fig. 5.2(c)	25.0 %	16.3 nm^2	4.6 nm

Table 5.1: Plateau statistics for Fig. 5.1(a) and Fig. 5.2.

on pristine CSS C-face graphene, however they are typically larger than those in NG and appear with a much lower density [76].

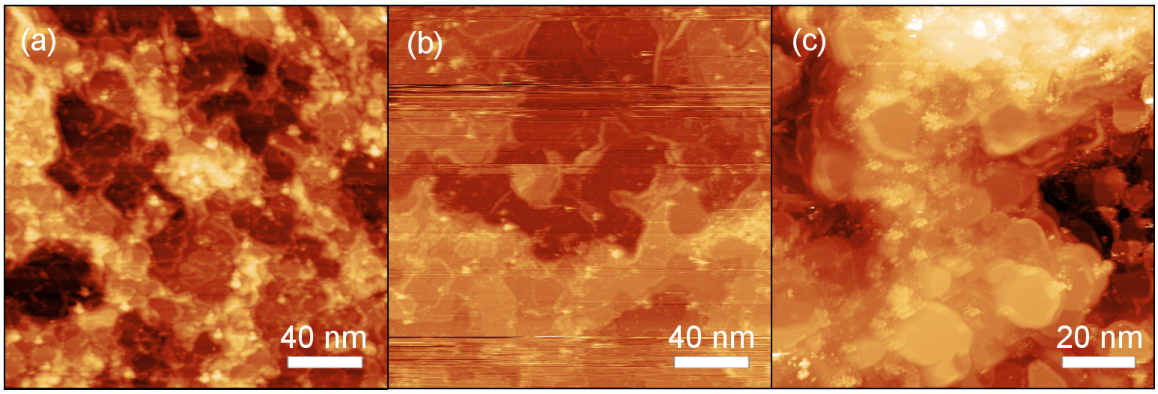

Figure 5.2: STM of NG plateaus. (a) 3 layers. 1 V, 0.2 nA. (b) 3 layers. 1 V, 0.05 nA. (c) 4 layers. -1 V, 0.2 nA. Taken at ANL (a), ORNL (b), and BNL (c).

Plateaus with hexagonal character are one of the most common features on all NG samples. Fig. 5.2 shows three overview images and Table 5.1 lists the statistics associated with the visible plateaus. Overall, plateaus range from 2-20 nm in diameter and are visible at every thickness of NG imaged in STM (1-8 layer). On the thinnest samples plateaus stand out as atomically flat islands agains the backdrop of rougher SiC surface texture (see Fig. 5.1(c); the SiC surface texture is visible at the left edge of the image). NG samples are commonly not fully covered with graphene until 3 layers are measured via XPS. This is not unexpected as C-face SiC graphene inherently has greater variation in graphene

thickness than Si-face graphene. Fig. 5.1(c) is a very thin sample, measured at fewer than 1 ML of graphene in XPS, yet Fig. 5.1(c) shows a central plateau that is at least 3 layers thick, just from counting step heights. Plateaus among large flat areas like the middle of Fig. 5.1(a) are most commonly seen on samples of intermediate thickness, 3-5 layers. The flat area in Fig. 5.1(a) clearly extends far beyond a diameter of 20 nm, but large pleats are strewn throughout the area so it is misleading to characterize it as a single flat plateau. The measurement of 20 nm as the maximum plateau diameter attempts to give a quantitative number to the largest areas with no pleats or ripples whatsoever. Overall plateaus (or larger flat areas) take up 25-40 % of the surface area on NG samples. The rest is filled by pleats surrounding plateaus, smooth rippled areas, and debris filled areas.

Substitutional nitrogen atoms in the graphene lattice are expected to have characteristic scattering patterns visible in STM images. However, in support of previously reported XPS analyses placing the nitrogen below the graphene, no scattering patterns indicating substitutional nitrogen were seen in NG [55, 53, 115]. Since XPS showed the interfacial nitrogen to be in sp^3 bonds, the nitrogen apparently pins the graphene to the substrate during growth, causing the film to buckle and form the observed wrinkles [65]. The line profile in Fig. 5.1 captures typical pleat and step heights following the dashed line in the Fig. 5.1(a). The step heights in this profile, as well as others not shown, indicate that often changes in NG surface height are created by SiC steps combined with graphene steps. This implies that changes in the surface topography are not solely the result of changes in graphene thickness. A study of step bunching on C-face SiC shows that nitrogen can increase the size of steps on the SiC surface [116]. In the case of NG, the graphene is able to conform to and maintain the substrate step profile or rippled morphology even after 4 layers as is seen in Fig. 5.1. Note that the interfacial nitrogen remains at the interface as SiC is consumed in the growth process.

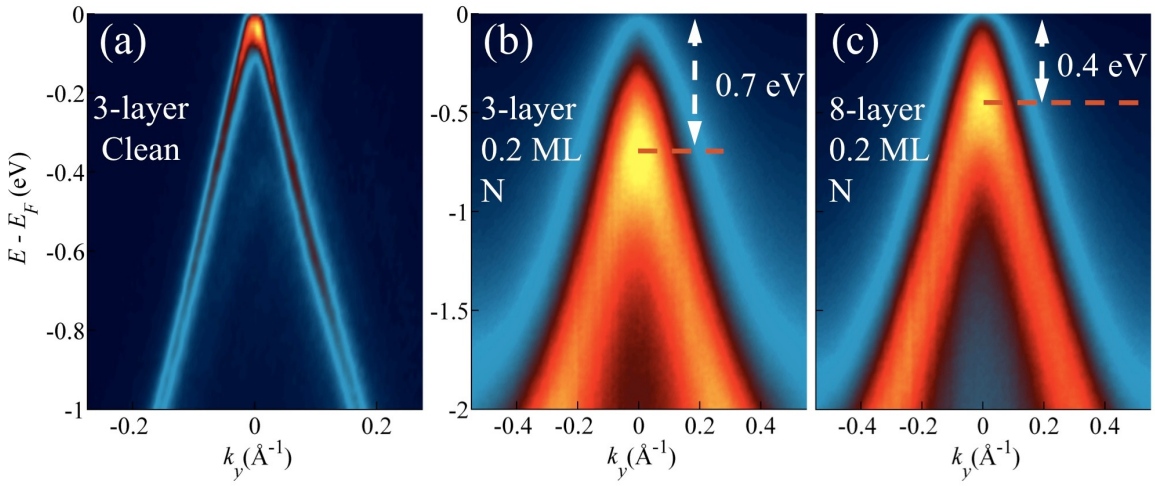

Figure 5.3: The ARPES band structure taken with $\hbar\omega = 36$ eV near the K-point of (a) CSS C-face SiC 3 layer graphene without nitrogen (T=100K), (b) 3 layer graphene grown on a 0.2 ML nitrogen SiC $(000\bar{1})$ surface (T=300K), and (c) 8 layer graphene grown on a 0.2 ML nitrogen SiC $(000\bar{1})$ surface (T=300K). k_y is perpendicular to the ΓK direction. Adapted from [65].

5.2 ARPES Characterization of NG

Fig. 5.3 reproduces ARPES taken on pristine C-face SiC graphene as well as two samples of NG of varying thickness. The Cassiopée beamline at SOLEIL synchrotron in Gif sur Yvette, France was used for the ARPES and variable energy XPS characterization.

The interfacial nitrogen preparation used for NG causes a valence band offset to open in the graphene π bands. The ARPES results, published in [65] and illustrated in Fig. 5.3, are taken at the graphene K-point (rotated 30° from the SiC $< 10\bar{1}0 >$ direction). Fig. 5.3(a) shows the typical band dispersion perpendicular to the ΓK direction at the graphene K-point from a clean 3 layer film. The linear π-bands are very distinctive [117]. The graphene band structures of a 3 and 8 layer film with 0.2 ML interfacial nitrogen content in contrast show an offset dependent on the number of layers in the NG. This is illustrated in Fig. 5.3(b) and (c) [65]. Unlike pristine graphene, the peak in the measured energy distribution along $k_y = 0$ from the nitrogen-seeded samples is shifted to higher binding energies, away from the measured Fermi energy. This valence band maximum, shifted down from the Fermi

energy, corresponds to an energy gap. The Dirac cone from the 3 layer NG sample has a 0.7 eV shift while the 8 layer film has a smaller 0.45 eV shift. The effective Fermi velocity (v) is reduced compared to pristine graphene, consistent with the opening of a bandgap. Both the 3 and 8 layer samples have $v = 0.8 \pm 0.05 * 10^6$ m/s.

The ARPES measurements from nitrogen-seeded graphene π bands are broader in k than for pristine graphene, largely due to the corrugation of the graphene surface shown in Fig. 5.1. Small modulations in the local graphene height cause a local angular variation in the surface normal; this is illustrated in Chapter 2 Fig. 2.2. Since the surface normal determines the orientation of the graphene Brillouin zone, the corrugated surface leads to local k_x and k_y shifts in the K-point. This leads to an ARPES image that is an area average of a distribution of parabolic cuts through Dirac cones from locally tilted graphene, resulting in an E- and k-broadened spectra.

The single, linear Dirac cone in Fig. 5.3(b) and (c) implies that the top layers of multilayer NG are not electrically coupled and that these layers behave as electronically distinct monolayer graphene sheets [118]. Therefore, any STS would be expected to similarly measure the LDOS and electronic features of monolayer graphene. It is known that multilayer graphene with inter-layer coupling no longer displays linear dispersion and has two visible cones in ARPES [119, 120]. If the band structure was from multiple coupled layers, a second cone (or more) would be expected. Bernal stacking would produce a band shifted 0.5 eV from the observed cone at higher binding energy [119], however no other cones shifted in k_y are visible. Shifted cones would also be expected because of the rotational stacking of C-face graphene [84]. The lack of these cones in Fig. 5.3 means that the rotation angle between the top two layers of graphene captured in the 50μm ARPES beam diameter must be rotated $> 10^\circ$ with respect to each other (this angle is set by the detector slit window). Such a large relative rotation angle between the two layers is known to keep the layers electronically decoupled [121, 69]. Thus these multilayer NG films act as electrically uncoupled, multiple, independent graphene layers.

5.3 STS Characterization of NG

STS was used to probe the LDOS in NG. Each STS spectrum is found by taking a derivative of current with respect to voltage as the STM tip is held fixed at one location and height, and is proportional to the LDOS in that area as derived in Chapter 2 [49]. Fig. 5.4(a) shows four typical NG STS spectra taken within 2 nm of the pleat at the edge of a plateau. Fig. 5.6 shows the observed spatial variation in NG STS spectra across a 0.5 nm high ripple. Fig. 5.5 shows the spatial location and variation of the spectra in Fig. 5.4. All STS figures display spectra vertically shifted for clarity. Following Levy et al. [59] and others [59, 14, 60] the symmetric peaks are identified as Landau levels due to a pseudo-magnetic field. The peaks are indexed with integer values of n and are fit to energies proportional to $\sqrt{n}$ since the ARPES measurements show independent, single layer graphene electronic behavior. Importantly, STS spectra from NG consistently lack a central peak near 0 V, close to the expected Dirac point. In contrast, other experimental measurements of pseudo field induced Landau levels in graphene all show a single, clearly visible central peak at the Dirac point [59, 111, 14, 60].

A bandgap in graphene may arise from an asymmetry between the A and B sublattices which may be modeled in the Dirac Hamiltonian by adding diagonal terms, $\pm\frac{\Delta}{2}$. The positions of Landau levels in a magnetic field are then given by:

$$E - E_D = \pm\sqrt{2e\hbar v^2 B|n| + \frac{\Delta^2}{4}}. \tag{5.1}$$

This equation was derived in Chapter 1; recall Eq. 1.48. Again, e is the electron charge, v the Fermi velocity, B the pseudo field magnitude, n the integer Landau index, and $\pm$ refers to the solution for valence and conduction bands respectively [19, 17, 122]. Each of these levels is expected to have the same number of states [11]. By this model, a gap splits the ground state Landau level into two $n = 0$ peaks for valence and conduction band such that $E_{gap} = \Delta$. No peak is visible at the Dirac point, E_D, which is assumed to be in the center of the gap.

Fig. 5.4 illustrates the method used to extract the pseudo-magnetic field magnitudes in

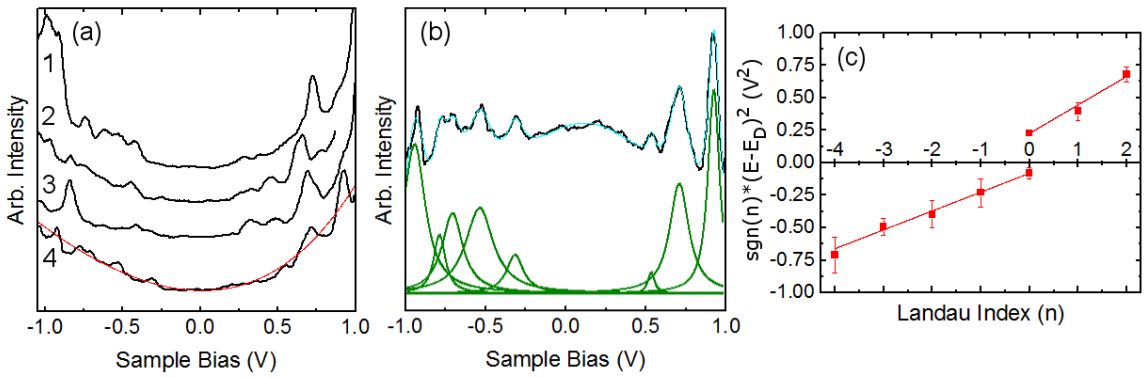

Figure 5.4: Scanning tunneling spectroscopy of 4 layer NG graphene (spectra vertically offset for clarity). (a) STS spectra (black) at different points near the edge of a plateau shown in Fig. 5.5; the bottom spectrum is fit with a polynomial background (red). (b) Residual after background subtraction (black) and Lorentzian peak fitting for spectrum 4 (cyan: total fit, green: individual Lorentzian peak fits). (c) Peak energy squared plotted against n, assuming a bandgap. The measured pseudo field magnitude is 256$\pm$12 T and 278$\pm$27 T for the valence and conduction bands respectively. STS taken at BNL at 4 K.

NG following Levy et al. [59]. The STS spectra in Fig. 5.4(a) were measured on a flat region, near the edge of a plateau as illustrated in Fig. 5.5. The spectrum background is fit with a fourth order polynomial (red). The top curve in Fig. 5.4(b) shows the residual spectrum for spectrum 4 after subtraction of the polynomial background. The bottom curves show Lorentzian fits to the peaks (green). The peaks are symmetric with widths of the order of 50-250 meV. Fig. 5.4(c) plots the square of the peak energies ($\pm$ for valence or conduction band) of the bottom spectrum against Landau index n; the expected linearity is evident. The Fermi velocity, $v = 0.8 \times 10^6$ m/s measured via ARPES [65], is used to determine the pseudo-magnetic field magnitude for both bands of spectrum 4 in Fig. 5.4 giving 256$\pm$12 T for the valence band and 278$\pm$27 T for the conduction band. The pseudo field magnitude varies between 160-300 T for all four spectra in Fig. 5.4, as shown in Fig. 5.5. This analysis is considered in further detail in the discussion section.

Fig. 5.6 shows a series of STS spectra taken across a typical 0.5 nm high ripple, found by zooming into a rippled region (similar to Fig. 5.1(e)). Each spectrum was taken mul-

Spectrum	E_D [eV]	Valence B [T]	Conduction B [T]
10	0.2790	1007±307	773±261
11	0.2813	1057±242	736±210
12	0.4841	1465±340	-
13	0.2768	1154±403	633±247
14	-0.0399	987±372	1970±411
15	0.2935	909±98	659±442
16	0.0114	-	958±211
17	0.2639	987±598	820±543
19	0.2986	1098±467	685±305
20	0.2675	572±117	745±294

Table 5.2: STS spectrum number, Dirac energies E_D, valence and conduction band pseudo-magnetic field magnitudes B for the series of STS spectra shown in Fig. 5.6. Conduction and valence band magnitudes are analyzed separately as illustrated in Fig. 5.4. Each Dirac energy E_D is the energy halfway between the first peaks on either side of 0 V in each spectrum.

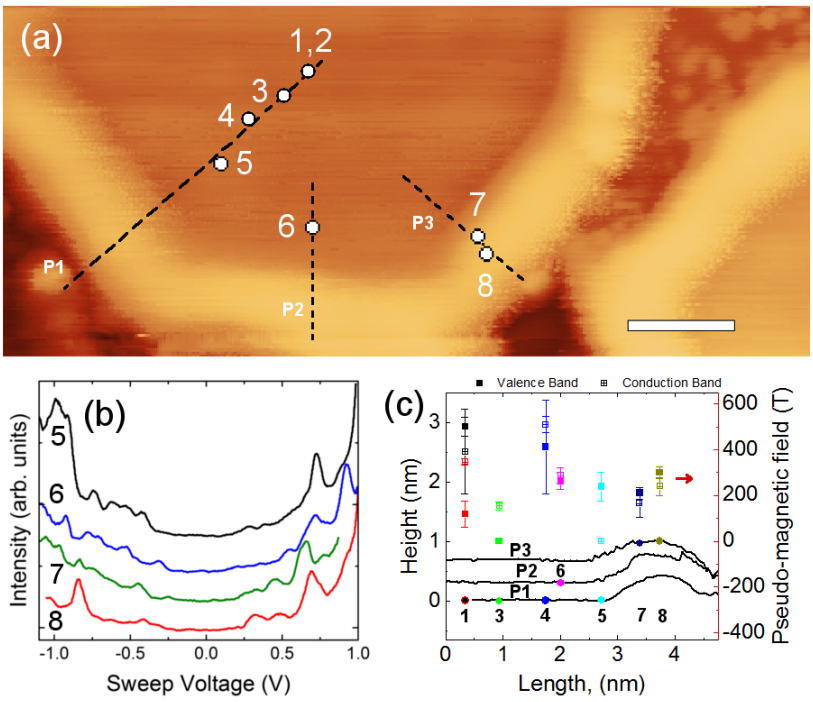

Figure 5.5: STS on 4 layer NG taken on a plateau and edge pleat. (a) STM topography image with profiles and STS locations marked. (b) STS spectra, offset for clarity. (c) Pseudo-magnetic field magnitudes plotted against profiles. Pseudo field magnitudes are between 150-500 T in magnitude. STS taken at BNL at 5 K.

tiple times to confirm reproducibility, and was analyzed as described in Fig. 5.4 with the removal of a polynomial background and Lorentzian peak fitting. The spectra are vertically shifted for clarity and have numbers corresponding to positions indicated on the STM image in Fig. 5.6(b) and (c). The measured pseudo-magnetic field magnitudes are plotted in Fig. 5.6(c) vs distance across the ripple along with the height of the ripple as measured by STM. A selection of the series of pseudo field magnitudes is also shown in Table 5.2. The error bars are from variance in the linear slope of index vs energy squared, originating from the width of the Lorentzian peaks used to fit each Landau level. The pseudo field magnitudes and topographic profiles in Fig. 5.5 are plotted analogously.

Electrostatic potential variations over the graphene would be expected to measurably shift the Dirac point in the STS spectra on NG. Although the center between conduction

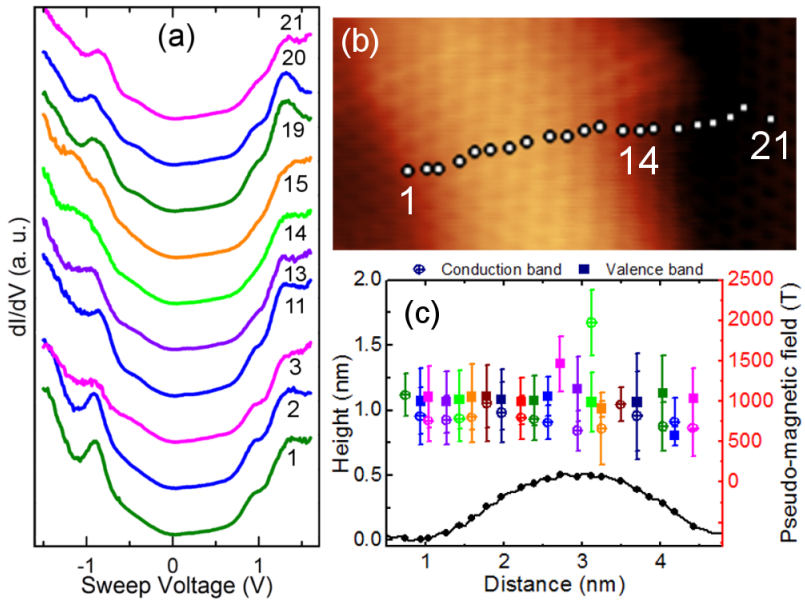

Figure 5.6: STS on 2-3 layer NG taken across a 0.5 nm high ripple. (a) Progression of STS spectra corresponding to pseudo-magnetic field values in (c) and positions in (b). (b) STM topography image with STS locations marked. (c) Pseudo-magnetic field magnitudes plotted against ripple profile, averaging around 1000 T. STS taken at ANL at 100 K.

and valence band peaks does shift by ± 0.5 V among the displayed measurements, there was no obvious correlation between these values and topography, pseudo field magnitude, or features in STM images.

5.4 Discussion

None of the STS spectra displayed in Figs. 5.4, 5.6, or 5.5 show the topologically protected peak at the Dirac point. There are two models which seem theoretically applicable for this: (1) The STS spectra may have a central $n = 0$ peak of such low intensity that the peak is not visible above the noise threshold, or (2) the spectra may have a split $n = 0$ peak which is posited to occur in graphene with a bandgap induced by two perturbations [30, 123]. For the first analysis model, the two peaks closest to 0 V in an NG spectrum would be analyzed as the $n = \pm 1$ peaks. For the second, the first peaks would be considered the respective $n = 0$

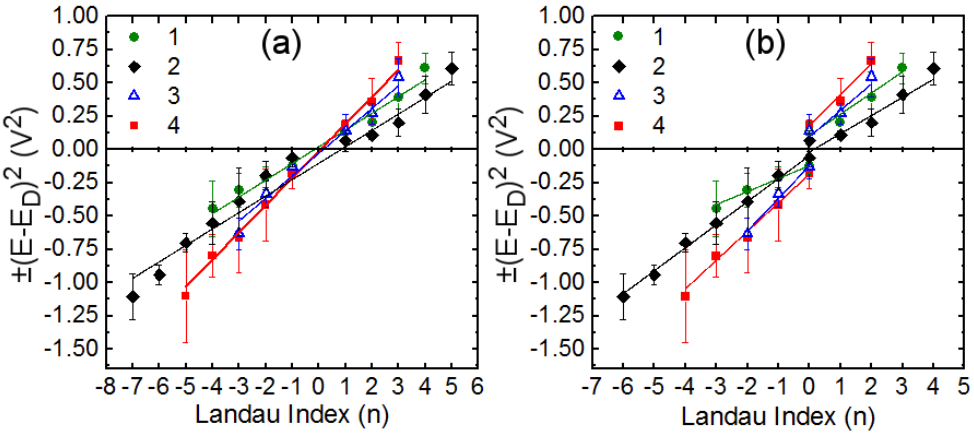

Figure 5.7: Comparison between two different analyses of peak energy squared vs. Landau index for the four spectra from Fig. 5.4. (a) Peaks are indexed with a missing $n = 0$ level. (b) Peaks are indexed with a split $n = 0$ level, including a bandgap in the model.

peaks for the valence and conduction band. Fig. 5.7 illustrates these alternate models using the four spectra from Fig. 5.4 by plotting peak energy squared against the Landau index for the two cases. As may be seen, both analysis procedures give excellent linearity and from this comparison alone it is difficult to say which model fits the data better. In addition, the pseudo field magnitudes determined by either model in Fig. 5.7 are similar.

Theory suggests that Landau levels should have the same number of states regardless of index, which would imply that very similar intensity would be expected for all Landau peaks [11, 52]. Previously published experimental data on Landau levels induced by pseudo-magnetic fields in graphene do show $n = 0$ central peaks with equivalent intensity to higher index peaks [59, 111, 14, 60]. This casts doubt on the likelihood of the first analysis model.

For Landau levels, the ground state $n = 0$ peak is doubly degenerate and requires two perturbations to break the symmetry (thereby inducing a bandgap). Pseudo-magnetic fields alone are insufficient to break the double degeneracy; another perturbation, such as an electrostatic field, must be present [30, 123, 17]. While the existence of strain giving rise to a pseudo-magnetic field is clearly consistent with the data, the origin of a second perturbation, such as an electrostatic field, is not yet known. Nevertheless, a split $n =$

0 peak is consistent with the previously mentioned ARPES measurement indicating an energy gap below the Fermi level. For these reasons the second analysis procedure seems most logical; all of the reported pseudo-magnetic field magnitudes reported herein use this method.

The theoretical predictions derived in Chapter 1, wherein topographically induced strain induces a pseudo-magnetic field, offer a modeling technique to predict the pseudo field magnitude expected from STS analysis of NG films. Recall in Eq. 1.68, the strain tensor for a topographic height profile $h(y)$ may be estimated from:

$$u_{xx} = \frac{\delta u_x}{\delta x} + \frac{1}{2}\frac{\delta h(x)}{\delta x}^2 \approx \frac{\delta}{\delta x}\frac{1}{2}(\frac{\delta h(x)}{\delta x})^2 + \frac{1}{2}\frac{\delta h(x)}{\delta x}^2 . \tag{5.2}$$

Using this approximation, a theoretical estimate of the pseudo-magnetic field was previously derived in Eq. 1.71 [124, 14, 125]:

$$B \propto -\frac{\beta}{a}\frac{4\pi^3 h^2}{w^3}\sin(\frac{4\pi x}{w}). \tag{5.3}$$

Considering the profile in Fig. 5.6 as a Gaussian 1D pleat height function, a maximum pseudo field of about 800 T is calculated, the same order of magnitude as the measured field of about 1000 T. Eq. 5.3 is plotted in Fig. 5.8 against the pseudo field magnitudes experimentally calculated from the STS spectra shown in Fig. 5.6.

Since the strain in NG films develops during growth, both positive and negative strain gradients are expected, and hence positive and negative pseudo fields which vary in magnitude and cross zero in between. Although STS spectra only measure an absolute value of the pseudo field magnitude, a decrease toward zero field and subsequent increase would be expected. Averaging over variation in local pseudo fields could obscure this trend, however. For the 1000 T field measured in Fig. 5.6, the extent of the Landau level's wavefunction is of order $2\sqrt{2\ln 2}l_B$ [126], or $\sim$2.3 nm. Since the ripple featured in Fig. 5.6 is only 4 nm wide, only small changes in the measured field would be expected. Indeed, the pseudo field magnitude varies only by $\pm$500 T across the feature. Fig. 5.4 displays spectra from locations on the flat area of a plateau and also on an edge pleat. It seems reasonable to consider the pleats to be under compressive strain, and the flat plateau area under tensile strain, if

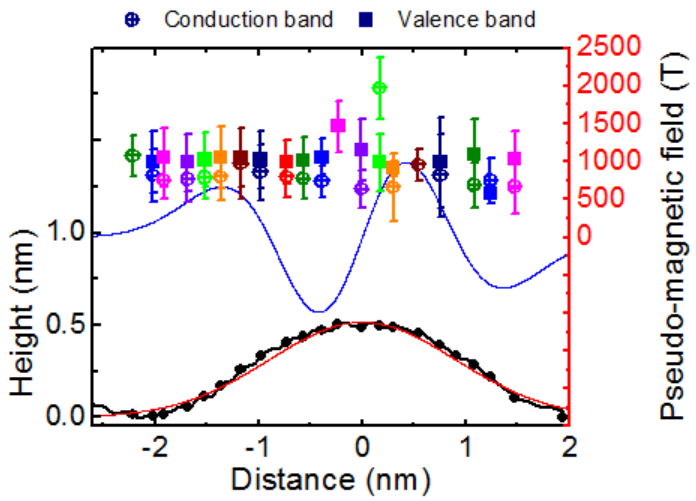

Figure 5.8: Comparison between a Gaussian height profile model for the pseudo-magnetic field magnitude (blue) and the measured pseudo-magnetic field magnitudes across the 0.5 nm high ripple shown in Fig. 5.6. The Gaussian fit to the profile used for the model (red) is plotted against the experimental profile (black) as well.

any. Despite the expected difference in strain, the variation in pseudo-field magnitude for Fig. 5.4 is no more than ± 90 T around an average value of 200 T. Similar instances where variation in pseudo field magnitude is expected but not experimentally observed have been reported by others [59, 14].

If the STS measurement averages over overlapping Landau wavefunctions, then it is reasonable to expect a contribution to the Landau level peak widths from the range of pseudo-magnetic field magnitudes in the surrounding region. As a rough estimate, the observed broadening from Eq. 5.1 should be of the order $\delta E = e\hbar v^2 |n| \delta B/(E - E_D)$. The peak widths for the bottom spectrum of Fig. 5.4 are variable and range from 50-250 meV for a measured field of $\sim$160-300 T. In Fig. 5.6 there is similar amount of broadening for a measured field of $\sim$1000 T. Some of this broadening appears to be an artifact of the peak fitting procedure used to determine the energy locations. Nevertheless, for the level of peak broadening observed in Figs. 5.4 and 5.6 even with the uncertainties, the pseudo field variation, δB, should be no more than about 30 T. This would seem to imply that a change

in pseudo field polarity would be visible via STS, even with averaging smoothing the data. Nevertheless, no zero crossing or minimum was observed in either Fig. 5.4, Fig. 5.5, or 5.6.

Another source of pseudo fields has been discussed by Guo et al. [58] who examined Landau levels seen at the surface of potassium intercalated graphite. They suggested that the pseudo fields could be induced by charge transfer, which could similarly induce individual hopping parameters as strain does. However, in the case of NG this should not be applicable. The nitrogen atoms, possibly the source of such charge, are positioned at the interface screened by several underlying layers of graphene, and the STS and STM measurements are most sensitive to the top layer alone.

5.5 Conclusion

In conclusion, STM and STS are used to characterize graphene grown on nitrogen-seeded SiC. Previous work indicated that NG has a gap of $>$0.7 eV, a topography consisting of many pleats, and a small nitrogen layer at the SiC-graphene interface. Landau level type peaks have been observed via STS essentially everywhere on the surface of NG films. No peaks were observed in STS spectra near the Dirac point, consistent with a bandgap and the splitting of the $n = 0$ level by two perturbations. A strong $\sqrt{n}$ dependence was observed in peak energy when a gap of $\sim$1 eV was included. A consistent variation in the measured pseudo field with strain or topography was not observed. In short, these STM and STS measurements of NG films are consistent with previous ARPES measurements characterizing strained graphene with a bandgap.

Final Conclusion

This thesis unites disparate work characterizing two types of graphene grown on crystalline substrates.

Graphene grown on sapphire (GOS) was fabricated and the procedures which enabled the growth of high-quality few layer graphene were investigated. Growth at 300-500 mTorr of acetylene at 1350-1450°C for 5 minutes fabricated GOS samples with Raman 2D/G peak ratios greater than 1.25 and thickness measurements indicating 1-5 layers. Raman peak widths indicate an average domain size between 20-200 nm across, however flat areas up to 250-2000 nm across are common. XRD and TEM measurements show turbostratic stacking, and the Raman 2D peak for multilayer samples is a single Lorentzian. Both turbostratic stacking and a lack of multiple peak components in the Raman 2D peak suggest that multilayer GOS may have non-interacting layers, similar to C-face SiC graphene, maintaining a linear energy dispersion.

Graphene grown on nitrogen-seeded SiC (NG) was also characterized with STM and STS. Previous characterization confirms that there is $\sim$0.2 ML of nitrogen between the graphene and SiC and that 25 % of the 0.2 ML of nitrogen is taken up in sp^3 bonds between the graphene and the substrate. NG has significant topography, characterized by atomically flat plateaus up to 20 nm across comprising 25-40 % of the surface. Smooth pleats and ripples, similar to features seen on pristine C-face SiC graphene but in much greater density, make up much of the rest of the surface. No scattering patterns from substitutional nitrogen were observed in STM images, supporting the previous variable energy XPS analysis that the nitrogen is at the SiC-graphene interface in NG samples. STS spectra showed Landau

levels, analyzed to result from strain-induced pseudo-magnetic fields. Landau levels were viewed at all locations probed on NG samples. The pseudo-magnetic field magnitudes measured from STS of Landau levels do not vary as theoretically predicted by topography induced strain. An analysis employing a bandgap fits the STS peak spectra consistently, supported by the valence band offset previously measured in NG via ARPES.

There are many further analyses to be considered in the areas considered in this thesis. In particular, transport measurements of GOS samples would be key in verifying the electronic character of this type of graphene. Pending a measurement of reasonable electron mobility, devices could be patterned directly on sapphire as a proof-of-concept for graphene grown directly on insulating crystalline surfaces. Further characterization of NG samples could give more precise specification for when the pseudo field magnitude fluctuations deviate from theoretical topography based models. Characterization of NG could continue with the goal of finding a correspondence between nitrogen coverage and NG topography. These and numerous other investigations promise to keep graphene at the top of the list of intriguing and rewarding topics for research.

Bibliography

[1] J. T. Robinson, J. S. Burgess, C. E. Junkermeier, S. C. Badescu, T. L. Reinecke, F. K. Perkins, M. K. Zalalutdniov, J.W. Baldwin, J. C. Culbertson, P. E. Sheehan, and E. S. Snow. Properties of fluorinated graphene films. *Nano Lett.*, 10:3001–3005, 2010.

[2] H. Liu, Y. Liu, and D. Zhu. Chemical doping of graphene. *J. Mater. Chem.*, 21: 3335–3345, 2011.

[3] M. Deifallah, P. McMillan, and F. Corà. Electronic and structural properties of two-dimensional carbon nitride graphenes. *J. Phys. Chem. C*, 112:5447–5453, 2008.

[4] C. Coletti, C. Riedl, D. S. Lee, B. Krauss, L. Patthey, K. von Klitzing, J. H. Smet, and U. Starke. Charge neutrality and band-gap tuning of epitaxial graphene on SiC by molecular doping. *Phys. Rev. B*, 81(235401), 2010.

[5] A. Lherbier, A. R. Botello-Méndez, and J.-C. Charlier. Electronic and transport properties of unbalanced sublattice N-doping in graphene. *Nano Lett.*, 13:1446–1450, 2013.

[6] Z. Chen, Y. Lin, M. Rooks, and P. Avouris. Graphene nano-ribbon electronics. *Physica E*, 40:228–232, 2007.

[7] M. Y. Han, B. Ozyilmaz, Y. Zhang, and P. Kim. Energy band-gap engineering of graphene nanoribbons. *Phys. Rev. Lett.*, 98:206805, 2007.

[8] J.-K. Lee, S. Yamazaki, H. Yun, J. Park, G. P. Kennedy, G.-T. Kim, O. Pietzsch, R. Wiesendanger, S. W. Lee, S. Hong, U. Dettla-Weglikowska, and S. Roth. Mod-

ulation of electronic structure of graphene by substrate induced nanomodulation. *Nano Lett.*, 13:3494–3500, 2013.

[9] A. Pirkle, J. Chan, A. Venugopal, D. Hinojos, C. W. Magnuson, S. McDonnell, L. Colombo, E. M. Vogel, R. S. Ruoff, and R. M. Wallace. The effect of chemical residues on the physical and electrical properties of chemical vapor deposition graphene transferred to SiO_2. *Appl. Phys. Lett.*, 99(122108), 2011.

[10] C. Kittel. *Introduction to solid state physics*. Wiley, 8th edition, 2004.

[11] M. I. Katsnelson. *Graphene: Carbon in two dimensions*. Cambridge University Press, 2012.

[12] H. Raza, editor. *Graphene nanoelectronics: Metrology, synthesis, properties and applications*. Springer, 2012.

[13] R. Saito, G. Dresselhaus, and M. S. Dresselhaus. *Physical Properties of Carbon Nanotubes*. Imperial College Press, 1998.

[14] L. Meng, W. He, H. Zheng, M. Liu, H. Yan, W. Yan, Z. Chu, K. Bai, R. Dou, Y. Zhang, Z. Liu, J. Nie, and L. He. Strain-induced one-dimensional Landau level quantization in corrugated graphene. *Phys. Rev. B*, 87:205405, 2013.

[15] M. Dresselhaus. Future directions in carbon science. *Annu. Rev. Mater. Sci.*, 27, 1997.

[16] R. Shankar. *Principles of quantum mechanics*. Springer, 2nd edition, 1994.

[17] X. Li, F. Zhang, and Q. Niu. Unconventional quantum hall effect and tunable spin hall effect in dirac materials: application to an isolated MoS_2 trilayer. *Phys. Rev. Lett.*, 110:066803, 2013.

[18] L. D. Landau and E. M. Lifschitz. *Theory of elasticity*. Pergamon Press, 2nd English edition, 1959.

[19] M. A. H. Vozmediano, M. I. Katsnelson, and F. Guinea. Gauge fields in graphene. *Phys. Rep.*, 496:109–148, 2010.

[20] F. Guinea, M. I. Katsnelson, and A. K. Geim. Energy gaps and a zero-field quantum Hall effect in graphene by strain engineering. *Nat. Phys.*, 6:30–33, 2010.

[21] G. J. Verbiest, S. Brinker, and C. Stampfer. Uniformity of the pseudomagnetic field in strained graphene. *Phys. Rev. B*, 92:075417, 2015.

[22] F. Guinea, M. I. Katsnelson, and M. A. H. Vozmediano. Midgap states and charge inhomogeneities in corrugated graphene. *Phys. Rev. B*, 77:075422, 2008.

[23] L. Tapasztó, T. Dumitrică, S. J. Kim, P. Nemes-Incze, C. Hwang, and L. P. Biró. Breakdown of continuum mechanics for nanometre-wavelength rippling of graphene. *Nat. Phys.*, 8:739–742, 2012.

[24] F. Guinea, B. Horovitz, and P. Le Doussal. Gauge fields, ripples, and wrinkles in graphene layers. *Solid State Comm.*, 149:1140–1143, 2009.

[25] Y. Aharonov and A. Casher. Ground state of a spin-1/2 charged particle in a two-dimensional magnetic field. *Phys. Rev. A*, 19(6):2461–2462, 1979.

[26] F. Guinea, B. Horovitz, and P. Le Doussal. Gauge fields induced by ripples in graphene. *Phys. Rev. B*, 77:205421, 2008.

[27] F. Guinea and T. Low. Band structure and gaps of triangular graphene superlattices. *Phil. Trans. R. Soc. A*, 368:5391–5402, 2010.

[28] Y. Chang, T. Albash, and S. Haas. Quantum hall states in graphene from strain-induced nonuniform magnetic fields. *Phys. Rev. B*, 86:125402, 2012.

[29] A. De Martino, L. Dell'Anna, and R. Egger. Magnetic confinement of massless dirac fermions in graphene. *Phys. Rev. Lett.*, 98(066802), 2007.

[30] I. Snyman. Gapped state of a carbon monolayer in periodic magnetic and electric fields. *Phys. Rev. B*, 80:054303, 2009.

[31] In conversation with T. Low.

[32] P. Yu and M. Cardona. *Fundamentals of semiconductors*. Springer, 2010.

[33] G. Haugstad. *Atomic force microscopy: understanding basic modes and advanced applications*. John Wiley & Sons, 2012.

[34] A. C. Ferrari and D. M. Basko. Raman spectroscopy as a versatile tool for studying the properties of graphene. *Nat. Nanotech.*, 8:235–246, 2013.

[35] A. C. Ferrari. Raman spectroscopy of graphene and graphite: Disorder, electron-phonon coupling, doping, and nonadiabatic effects. *Solid State Commun.*, 143:47–57, 2007.

[36] G. Moliter. Spatially resolved Raman spectroscopy of single- and few-layer graphene. *Nano Lett.*, 7(2):238–242, 2007.

[37] N. Ferralis. Probing mechanical properties of graphene with Raman spectroscopy. *J. Mater. Sci.*, **45**:5135–5149, (2010).

[38] F. Tunistra and J. L. Koening. Raman spectra of graphite. *J. Chem. Phys.*, 53:1126, 1970.

[39] T. Schumann. *Direct growth and characterization of graphene layers on insulating substrates*. PhD thesis, Humboldt-Universität zu Berlin, 2014.

[40] J. E. Lee, G. Ahn, J. Shim, Y. S. Lee, and S. Ryu. Optical separation of mechanical strain from charge doping in graphene. *Nat. Commun.*, 3(1024):1–8, 2012.

[41] I. Calizo, W. Bao, F. Miao, C. N. Lau, and A. A. Balandin. The effect of substrates on the Raman spectra of graphene: graphene-on-sapphire and graphene-on-glass. *Appl. Phys. Lett.*, 91(201904), 2007.

[42] I. Calizo, S. Ghosh, W. Bao, F. Miao, C. N. Lau, and A. A. Balandin. Raman nanometerology of graphene: Temperature and substrate effects. *Solid State Commun.*, 149:1132–1135, 2009.

[43] Y. Y. Wang, Z. H. Ni, T. Yu, Z. X. Shen, H. M. Wang, and Y. H. Wu. Raman studies of monolayer graphene: the substrate effect. *J. Phys. Chem. C*, 112(29): 10637–10640, 2008.

[44] Z. H. Ni, T. Yu, Y. H. Lu, Y. Y. Wang, Y. P. Feng, and Z. X. Shen. Uniaxial strain on graphene: Raman spectroscopy study and band-gap opening. *ACS Nano*, 2(11): 2301–2305, 2008.

[45] C. J. Chen. *Introduction to scanning tunneling microscopy*. Oxford University Press, 2nd edition, 2008.

[46] G. M. Rutter. *Atomic scale properties of epitaxial graphene grown on silicon carbide (0001)*. PhD thesis, Georgia Institute of Technology, 2008.

[47] J. S. Townsend. *A modern approach to quantum mechanics*. University Science Books, 2000.

[48] J. Bardeen. Tunneling from a many-particle point of view. *Phys. Rev. Lett.*, 6(2): 57–59, 1961.

[49] C. J. Chen. Theory of scanning tunneling spectroscopy. *J. Vac. Sci. Technol. A*, 6(2), 1988.

[50] K. S. Novoselov, A. K. Geim, S. V. Morozov, D. Jiang, Y. Zhang, S. V. Dubonos, I. V. Grigorieva, and A. A. Firsov. Electric field effect in atomically thin carbon films. *Sci.*, 306(5696):666–669, 2004.

[51] C. Riedl. *Epitaxial graphene on silicon carbide surfaces: Growth, chracterization, doping and hydrogen intercalation*. PhD thesis, Friedrich-Alexander-Universität Erlangen-Nürnburg, 2010.

[52] E. Andrei, G. Li, and X. Du. Electronic properties of graphene: a perspective from scanning tunneling microscopy and magnetotransport. *Rep. Prog. Phys.*, 75:056501, 2012.

[53] N. P. Guisinger, G. M. Rutter, J. N. Crain, C. Heiliger, P. N. First, and J. A. Stroscio. Atomic scale investigation of graphene formation on 6H-SiC (0001). *J. Vac. Sci. and Technol. A*, 26(932):932–937, 2008.

[54] G. M. Rutter, J. N. Crain, N. P. Guisinger, T. Li, P. N. First, and J. A. Stroscio. Scattering and interference in epitaxial graphene. *Sci.*, 317:219–222, 2007.

[55] F. Joucken, Y. Tison, J. Lagoute, J. Dumont, D. Cabosart, B. Zheng, V. Repain, C. Chacon, Y. Girard, A. R. Botello-Méndez, S. Rousset, R. Sporken, J.-C. Charlier, and L. Henrard. Localized state and charge transfer in nitrogen-doped graphene. *Phys. Rev. B*, 85:161408, 2012.

[56] J. Barringhaus, M. Ruan, F. Edler, A. Tejeda, M. Sicot, A. Taleb-Ibrahimi, A.-P. Li, Z. Jiang, E. H. Conrad, C. Berger, C. Tegenkamp, and W. A. de Heer. Exceptional ballistic transport in SiC sidewall ribbons. *Nat.*, 506:349–354, 2014.

[57] V. W. Brar, Y. Zhang, Y. Yayon, T. Ohta, J. McChesney, A. Bostwick, E. Rotenberg, K. Horn, and M. Crommie. Scanning tunneling spectroscopy of inhomogenous electronic structure in monolayer and bilayer graphene on SiC. *Appl. Phys. Lett.*, 91 (122102), 2007.

[58] D. Guo, T. Kondo, T. Machida, K. Iwatake, S. Okada, and J. Nakamura. Observation of Landau levels in potassium-intercalated graphite under a zero magnetic field. *Nat. Commun.*, 3(1068):1–6, 2012.

[59] N. Levy, S. A. Burke, K. L. Meaker, M. Panlasigui, A. Zettl, F. Guinea, A. H. Castro Neto, and M. F. Crommie. Strain-induced pseudo-magnetic fields greater than 300 Tesla in graphene nanobubbles. *Sci.*, 329:544–547, 2010.

[60] H. Yan, Y. Sun, L. He, J.-C. Nie, and M. H. W. Chan. Observation of Landau-level-like quantization at 77 K along a strained-induced graphene ridge. *Phys. Rev. B*, 85: 035422, 2012.

[61] N.-C. Yeh, M.-L. Teague, S. Yeom, B. L. Standley, R. T.-P. Wu, D. A. Boyd, and M. W. Bockrath. Strain induced pseudo-magnetic fields and charging effects on CVD-grown graphene. *Surf. Sci.*, 605:1649–1656, 2011.

[62] N.-C. Yeh, M.-L. Teague, D. A. Boyd, M. W. Bockrath, J. Velasco, and C.-N. Lau. Scanning tunneling spectroscopic studies of the effects of dielectrics and metallic substrates on the local electronic characteristics of graphene. *ECS Transactions*, 28: 115–123, 2010.

[63] M. Orlita, C. Faugeras, P. Plochocka, P. Neugebauer, G. Martinez, D. K. Maude, A.-L. Barra, M. Sprinkle, C. Berger, W. A. de Heer, and M. Potemski. Approaching the Dirac point in high-mobility multilayer epitaxial graphene. *Phys. Rev. Lett.*, 101: 267601, 2008.

[64] P. van der Heide. *X-ray photoelectron spectroscopy: an introduction to principals and practices*. John Wiley & Sons, 2011.

[65] F. Wang, G. Liu, S. L. Rothwell, M. Nevius, A. Tejeda, A. Taleb-Ibrahimi, L. C. Feldman, P. I. Cohen, and E. H. Conrad. Wide-gap semiconducting graphene from nitrogen-seeded SiC. *Nano Lett.*, 13:4827–4832, 2013.

[66] K. V. Emtsev, F. Speck, Th. Seyller, L. Ley, and J. D. Riley. Interaction, growth, and ordering of epitaxial graphene on SiC $\{0001\}$ surfaces: A comparative photoelectron spectroscopic study. *Phys. Rev. B*, 77:155303, 2008.

[67] G. G. Jernigan, B. L. VanMil, J. L. Tedesco, J. G. Tischler, E. R. Glaser, A. Davidson III, P. M. Campbell, and D. K. Gaskill. Comparison of epitaxial graphene on Si-face and C-face 4H SiC formed by ultrahigh vacuum and RF furnace production. *Nano Lett.*, 9(7):2605–2609, 2009.

[68] S. Bae, H. Kim, Y. Lee, X. Xu, J.-S. Park, Y. Zheng, J. Balakrishnan, T. Lei, H. R. Kim, Y. I. Song, Y.-J. Kim, K. S. Kim, B. Özyilmaz, J.-H. Ahn, B. H. Hong, and S. Iijima. Roll-to-roll production of 30-inch graphene films for transparent electrodes. *Nat. Nanotech.*, 5:574–578, 2010.

[69] W. A. de Heer, C. Berger, X. Wu, M. Sprinkle, Y. Hu, M. Ruan, J. A. Stroscio, P. N. First, R. Haddon, B. Piot, C. Faugeras, M. Potemski, and J.-S. Moon. Epitaxial graphene electronic structure and transport. *J. Phys. D: Appl. Phys.*, 43(374007), 2010.

[70] M. Henini. *Molecular Beam Epitaxy: from research to mass production*. Amsterdam: Elsevier, 2012.

[71] T. M. French and G. A. Somorjai. Composition and surface structure of the (0001) face of α-Alumina by low-energy electron diffraction. *J. Phys. Chem.*, 74(12):2489–2495, 1970.

[72] L. Malard, M. Pimenta, G. Dresselhaus, and M. Dresselhaus. Raman spectroscopy in graphene. *Phys. Rep.*, 473(5-6):51–87, 2009.

[73] J. Röhrl, M. Hundhausen, K. Emtsev, T. Seyller, and R. Graupner. Raman spectra of epitaxial graphene on SiC (0001). *Appl. Phys. Lett.*, 92, 2008.

[74] Z. Q. Li, C. J. Lu, Z. P. Xia, Y. Zhou, and Z. Luo. X-ray diffraction patterns of graphite and turbostratic carbon. *Carbon*, 45(8):1686–1695, 2007.

[75] J. R. Hass. *Structural characterization of epitaxial graphene on SiC*. PhD thesis, Georgia Institute of Technology, 2008.

[76] W. A. de Heer, C. Berger, M. Ruan, M. Sprinkle, X. Li, Y. Hu, B. Zhang, J. Hackinson, and E. H. Conrad. Large area and structured epitaxial graphene produced by confinement controlled sublimation of silicon carbide. *Proc. Natl. Acad. Sci.*, 108 (41):16900–16905, 2011.

[77] C. Berger, Z. Song, T. Li, X. Li, A. Y. Ogbazghi, R. Feng, Z. Dai, A. N. Marchenkov, E. H. Conrad, P. N. First, and W. A. de Heer. Ultrathin epitaxial graphene: 2D electron gas properties and a route toward graphene-based nanoelectronics. *J. Phys. Chem. B*, 108(52):19912–19916, 2004.

[78] N. Camara, A. Tiberj, B. Jouault, A. Caboni, B. Jabakhanji, N. Mestres, P. Godignon, and J. Camassel. Current status of self-organized epitaxial graphene ribbons on the C face of 6H-SiC substrates. *J. Phys. D: Appl. Phys.*, 43(37):374011, 2010.

[79] P. Lauffer and K. V. Emtsev. Atomic and electronic structure of few-layer graphene on SiC(0001) studied with scanning tunneling microscopy and spectroscopy. *Phys. Rev. B*, 77:155426, 2008.

[80] W. A. de Heer, C. Berger, X. Wu, P. N. First, E. H. Conrad, X. Li, T. Li, M. Sprinkle, J. R. Hass, M. L. Sadowski, M. Potemski, and G. Martinez. Epitaxial graphene. *Solid State Commun.*, 143:92–100, 2007.

[81] D. L. Miller. *Atomic-scale spectroscopy and mapping of magnetic states in epitaxial graphene*. PhD thesis, Georgia Institute of Technology, 2010.

[82] J. Hass, R. Feng, J. E. Millán-Otoya, X. Li, M. Sprinkle, P. N. First, W. A. de Heer, and E. H. Conrad. Structural properties of the multilayer graphene 4H-SiC $(000\bar{1})$ system as determined by surface X-ray diffraction. *Phys. Rev. B*, 75:214109, 2007.

[83] M. Sprinkle, J. Hicks, A. Tejeda, A. Taleb-Ibrahimi, P. Le Fèvre, F. Bertran, H. Tinkey, M. C. Clark, P. Soukiassian, D. Martinotti, J. Hass, and E. H. Conrad. Multilayer epitaxial graphene grown on the SiC $(000\bar{1})$ surface; structure and electronic properties. *J. Phys. D: Appl. Phys.*, 43(374006), 2010.

[84] J. Hass, F. Varchon, J. E. Millán-Otoya, M. Sprinkle, N. Sharma, W. A. de Heer, C. Berger, P. N. First, L. Magaud, and E. H. Conrad. Why multilayer graphene on 4H-SiC $(000\bar{1})$ behaves like a single sheet of graphene. *Phys. Rev. Lett.*, 100:125504, 2008.

[85] C. Riedl, C. Coletti, T. Iwasaki, A. A. Zakharov, and U. Starke. Quasi-free-standing epitaxial graphene on SiC obtained by hydrogen intercalation. *Phys. Rev. Lett.*, 103 (246804), 2009.

[86] D. Yoon, Y. Son, and H. Cheong. Negative thermal expansion coefficient of graphene measured by Raman spectroscopy. *Nano Lett.*, 11(8):3227–3231, 2011.

[87] W. Gao and R. Huang. Thermomechanics of monolayer graphene: rippling, thermal expansion and elasticity. *J. Mech. Phys. Solids*, 66:42–58, 2014.

[88] W. Bao, F. Miao, Z. Chen, H. Zhang, W. Jang, C. Dames, and C. N. Lau. Controlled ripple texturing of suspended graphene and ultrathin graphite membranes. *Nat. Nanotech.*, 4:562–566, 2009.

[89] N. Mounet and N. Marzari. First-principle determination of the structural, vibrational, and thermodynamic properties of diamond, graphite, and derivatives. *Phys. Rev. B*, 71:205214, 2005.

[90] J.-W. Jiang, J.-S. Wang, and B. Li. Thermal expansion in single-walled carbon nanotubes and graphene: nonequilibrium Green's function approach. *Phys. Rev. B*, 80:205429, 2009.

[91] E. R. Dobrovinskaya, L. A. Lytvynov, and V. Pishchik. *Sapphire: material, manufacturing, applications*. Springer, 2009.

[92] R. F. Pierret. Advanced semiconductor fundamentals. In R. F. Pierret and G. W. Neudeck, editors, *Modular series on solid state devices*, volume VI. Prentice Hall, 2nd edition, 2003.

[93] X.-L. Wei, H. Fang, R.-Z. Wang, Y.-P. Chen, and J.-X. Zhong. Energy gaps in nitrogen delta-doping graphene: a first-principles study. *Appl. Phys. Lett.*, 99(012107), 2011.

[94] I. Shimoyama, G. Wu, T. Sekiguchi, and Y. Baba. Evidence for the existence of nitrogen-substituted graphite structure by polarization dependence of near-edge X-ray-absorption fine structure. *Phys. Rev. B*, 62(6053(R)), 2000.

[95] D. Wei, Y. Liu, Y. Wang, H. Zhang, L. Huang, and G. Yu. Synthesis of N-doped graphene by chemical vapor deposition and its electrical properties. *Nano Lett.*, 9 (5):1752–1758, 2009.

[96] Y. Wang, Y. Shao, D. W. Matson, J. Li, and Y. Lin. Nitrogen-doped graphene and its application in electrochemical biosensing. *ACS Nano*, 4(4):1790–1798, 2010.

[97] D. Usachov, O. Vilkov, A. Gruneis, D. Haberer, A. Fedorov, V. K. Adamchuk, A. B. Preobrajenski, P. Dudin, A. Barinov, M. Oehzeltz, C. Laubschat, and D. V. Vyalikh. Nitrogen-doped graphene: Efficient growth, structure, and electronic properties. *Nano Lett.*, 11:5401–5407, 2011.

[98] C. Zhang, L. Fu, N. Liu, M. Liu, Y. Wang, and Z. Liu. Synthesis of nitrogen-doped graphene using embedded carbon and nitrogen sources. *Adv. Mater.*, 23:1020–1024, 2011.

[99] E. Velez-Fort, C. Mathieu, E. Pallecchi, M. Pigneur, M. G. Silly, R. Belkhou, M. Marangolo, A. Shukla, F. Sirotti, and A. Ouerghi. Epitaxial graphene on 4H-SiC grown under nitrogen flux: evidence of low nitrogen doping and high charge transfer. *ACS Nano*, 6(12):10893–10900, 2012.

[100] R. Podila, J. Chacón-Torres, J. T. Spear, T. Pichler, and P. Ayala. Spectroscopic investigation of nitrogen doped graphene. *Appl. Phys. Lett.*, 101(123108), 2012.

[101] H. Wang, T. Maiyalagan, and X. Wang. Review on recent progress in nitrogen-doped graphene: Synthesis, characterization, and its potential applications. *ACS Catal.*, 2: 781–794, 2012.

[102] Y.-F. Lu, S.-T. Lo, J.-C. Lin, W. Zhang, J.-Y. Lu, F.-H. Liu, C.-M. Tseng, Y.-H. Lee, C.-T. Liang, and L.-J. Li. Nitrogen-doped graphene sheets grown by chemical vapor

deposition: synthesis and influence of nitrogen impurities on carrier transport. *ACS Nano*, 7(8):6522–6532, 2013.

[103] Z. Wang, P. Li, Y. Chen, J. Liu, H. Tian, J. Zhou, W. Zhang, and Y. Li. Synthesis of nitrogen-doped graphene by chemical vapor deposition using melamine as the sole solid source of carbon and nitrogen. *J. Mater. Chem. C*, 2(7396), 2014.

[104] T. Katoh, G. Imamura, S. Obata, M. Bhanuchandra, G. Copley, H. Yorimitsu, and K. Saiki. The influence of source molecule structure on the low temperature growth of nitrogen-doped graphene. *Phys. Chem. Chem. Phys.*, 17:14115–14121, 2015.

[105] A. Snis and S. F. Matar. Electronic density of states, 1s core-level shifts, and core ionization energies of graphite, diamond, C3N4 phases, and graphitic C11N4. *Phys. Rev. B*, 60(10855), 1999.

[106] S. Dhar. *Nitrogen and hydrogen induced trap passivation at the SiO2/4H-SiC interface*. PhD thesis, Vanderbilt University, 2005.

[107] J. Gimbert, T. Billon, T. Ouisse, J. Grisolia, G. Ben-Assayag, and C. Jaussaud. Nitrogen implantation in 4H and 6H-SiC. *Mat. Sci. and Eng. B*, 61-62:368–372, 1999.

[108] B. Zheng, P. Hermet, and L. Henrard. Scanning tunneling microscopy simulations of nitrogen- and boron-doped graphene and single-walled carbon nanotubes. *ACS Nano*, 4(7):4165–4173, 2010.

[109] Y. Tison, J. Lagoute, V. Repain, C. Chacon, Y. Girard, S. Rousset, F. Joucken, D. Sharma, L. Henrard, H. Amara, A. Ghedjatti, and F. Ducastelle. Electronic interaction between nitrogen atoms in doped graphene. *ACS Nano*, 9(1):670–678, 2015.

[110] D. Moldovan, M. R. Masir, and F. R. Peeters. Electronic states in a graphene flake strained by a Gaussian bump. *Phys. Rev. B*, 88(035446), 2013.

[111] J. Lu, A. H. Castro Neto, and K. P. Loh. Transforming moiré blisters into geometric graphene nano-bubbles. *Nat. Commun.*, 3(823), 2012.

[112] K. K. Gomes, W. Mar, W. Ko, F. Guinea, and H. C. Manoharan. Designer Dirac fermions and topological phases in molecular graphene. *Nature*, 483:306–310, 2012.

[113] F. Wang, G. Liu, S. L. Rothwell, M. S. Nevius, C. Mathieu, N. Barrett, A. Sala, T. O. Menteş, A. Locatelli, P. I. Cohen, L. C. Feldman, and E. H. Conrad. Pattern induced ordering of semiconducting graphene ribbons grown from nitrogen-seeded SiC. *Carbon*, 82:360–367, 2015.

[114] M. Naitoh, M. Kitada, S. Nishigaki, N. Toyama, and F. Shoji. An STM observation of the initial process of graphitization at the 6H-SiC $(000\bar{1})$ surface. *Surf. Rev. Lett.*, 10(2 & 3):473–477, 2003.

[115] R. Lv, Q. Li, A. R. Botello-Méndez, T. Hayashi, B. Wang, A. Berkdemir, Q. Hao, A. L. Elías, R. Cruz-Silva, H. R. Gutiérrez, Y. A. Kim, H. Muramatsu, J. Zhu, M. Endo, H. Terrones, J.-C. Charlier, M. Pan, and M. Terrones. Nitrogen-doped graphene: beyond single substitution and enhanced molecular sensing. *Sci. Reports*, 2(586), 2012.

[116] N. Ohtani, M. Katsuno, T. Aigo, T. Fujimoto, H. Tsuge, H. Yashiro, and M. Kanaya. Step bunching behavior on the $\{0001\}$ surface of hexagonal SiC. *J. Crys. Growth*, 210:613–622, 2000.

[117] J. Hicks, K. Shepperd, F. Wang, and E. H. Conrad. The structure of graphene grown on SiC $(000\bar{1})$. *J. Phys. D. Appl. Phys.*, 45:154002, 2012.

[118] M. Sprinkle, P. Soukiassian, W. A. de Heer, C. Berger, and E. H. Conrad. Epitaxial graphene: the material for graphene electronics. *Phys. Status Solidi*, 3(6):A91–A94, 2009.

[119] T. Ohta, A. Bostwick, J. L. Mcchesney, T. Seyller, K. Horn, and E. Rotenberg. Interlayer interaction and electronic screening in multilayer graphene investigated with angle-resolved photoemission spectroscopy. *Phys. Rev. Lett.*, 98(20):206802, MAY 18 2007. ISSN 0031-9007. doi: 10.1103/PhysRevLett.98.206802.

[120] T. Ohta, J. T. Robinson, P. J. Feibelman, A. Bostwick, E. Rotenberg, and T. E. Beechem. Evidence for interlayer coupling and moiré periodic potentials in twisted bilayer graphene. *Phys. Rev. Lett.*, 109:186807, 2012.

[121] J. M. B. L. dos Santos, N. M. R. Peres, and A. H. Castro Neto. Graphene bilayer with a twist: electronic structure. *Phys. Rev. Lett.*, 99:256802, 2007. doi: 10.1103/PhysRevLett.99.256802.

[122] H. Aoki and M. S. Dresselhaus, editors. *Physics of Graphene*. Springer, 2014.

[123] T. Low, F. Guinea, and M. I. Katsnelson. Gaps tunable by electrostatic gates in strained graphene. *Phys. Rev. B*, 83(195436), 2011.

[124] M. Neek-Amal and F. M. Peeters. Strain-engineered graphene through a nanostructured substrate. II. Pseudomagnetic fields. *Phys. Rev. B*, 85(19):195446, 2012.

[125] Y. Jiang, T. Low, K. Chang, M. I. Katsnelson, and F. Guinea. Generation of pure bulk valley current in graphene. *Phys. Rev. Lett.*, 110(4):046601, JAN 23 2013. ISSN 0031-9007. doi: 10.1103/PhysRevLett.110.046601.

[126] E. McCann. Ch. 8 Electronic properties of monolayer and bilayer graphene. In H. Raza, editor, *Graphene nanoelectronics: Metrology, synthesis, properties and applications*, page 259. Springer, 2012.